Scientific Research

JBiSE

ISSN: 1937-6871

Volume 2 Number 5 September 2009

Journal of Biomedical Science and Engineering

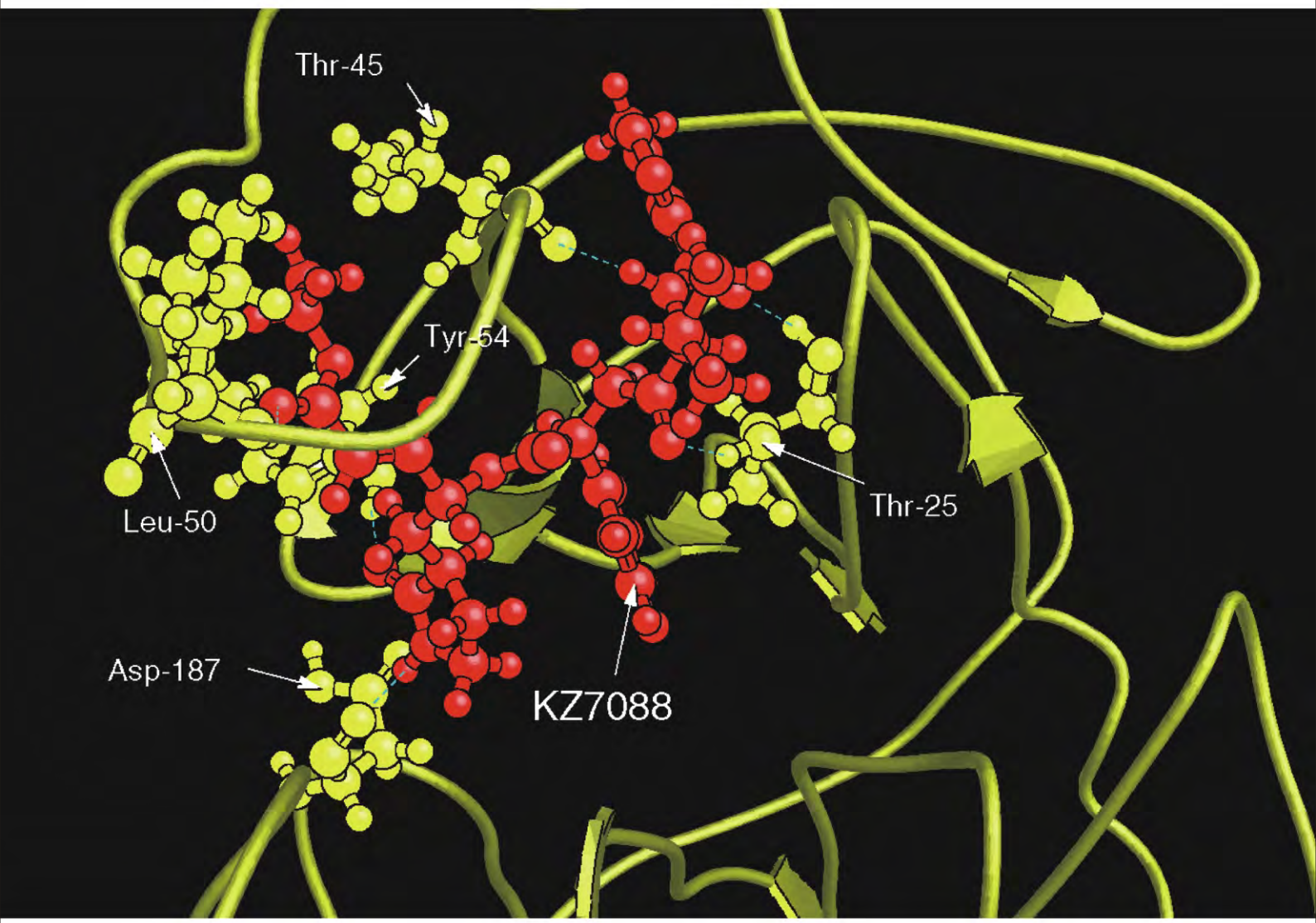

www. scirp. org/journal/jbise

Journal Editorial Board

ISSN 1937-6871 (Print) ISSN 1937-688X (Online)

http://www.scirp.org/journal/jbise

Journal of Biomedical Science and Engineering (JBiSE)
Published Online September 2009 in SciRes (http://www.scirp.org/journal/jbise).

TABLE OF CONTENTS

Volume 2, Number 5, September 2009

The figure on the front cover shows the binding interaction between the inhibitor KZ7088 and the SARS enzyme. (Courtesy of Kuo-Chen Chou.)

Journal of Biomedical Science and Engineering (JBiSE)

SUBSCRIPTIONS

The ***Journal of Biomedical Science and Engineering*** (Online at Scientific Research Publishing, www.scirp.org) is published monthly by Scientific Research Publishing, Inc., USA.
E-mail: service@scirp.org

Subscription Rates: Volume 2 2009

Printed: $50 per copy.

Electronic: freely available at www.scirp.org.

To subscribe, please contact Journals Subscriptions Department at service@scirp.org.

Sample Copies: If you are interested in obtaining a free sample copy, please contact Scientific Research Publishing, Inc at service@scirp.org.

SERVICES

Advertisements

Contact the Advertisement Sales Department at service@scirp.org.

Reprints (a minimum of 100 copies per order)

Contact the Reprints Co-ordinator, Scientific Research Publishing, Inc., USA.
E-mail: service@scirp.org

PRODUCTION INFORMATION

For manuscripts that have been accepted for publication, please contact:
E-mail: jbise@scirp.org

J. Biomedical Science and Engineering, 2009, 2, 287-293 **JBiSE**
doi: 10.4236/jbise.2009.25043 Published Online September 2009 (http://www.SciRP.org/journal/jbise/).

A new size and shape controlling method for producing calcium alginate beads with immobilized proteins

Yan Zhou[1], Shin'ichiro Kajiyama[1], Hiroshi Masuhara[2*], Yoichiro Hosokawa[2*], Takahiro Kaji[2*], Kiichi Fukui[1]**

[1]Department of Biotechnology, Grad. School of Engineering, Osaka University, 2-1 Yamadaoka, Suita, 565-0871, Osaka, Japan; [2]Department of Applied Physics, Grad. School of Engineering, Osaka University, 2-1 Yamadaoka, Suita, 565-0871, Osaka, Japan; [*]Present address: Nara Institute for Science and Technology, 8916-5, Takayama, Ikoma 630-0192, Nara, Japan.
Email: kfukui@bio.eng.osaka-u.ac.jp

Received 29 April 2009; revised 10 May 2009; accepted 15 May 2009.

ABSTRACT

A method for producing size- and shape-controlled calcium alginate beads with immobilized proteins was developed. Unlike previous calcium alginate bead production methods, protein-immobilized alginate beads with uniform shape and sizes less then 20 micrometers in diameter could successfully be produced by using sonic vibration. BSA and FITC-conjugated anti-BSA antibodies were used to confirm protein immobilization in the alginate beads. Protein diffusion from the beads could be reduced to less than 10% by cross-linking the proteins to the alginate with 1-ethyl-3-(3-dimethylaminopropyl)carbodiimide (EDC) and *N*-hydroxysulfosuccinimide (NHSS). The calcium alginate beads could also be arranged freely on a slide glass by using a femtosecond laser.

Keywords: Calcium Alginate Beads; Size Controllable Production Method; Protein Immobilized Beads; Femtosecond Laser; Laser Manipulation

1. INTRODUCTION

Calcium alginate beads have been widely used for immobilizing DNA [1,2,3,4], proteins [5,6], and cells [7] for applications in a variety of fields. In our laboratory, alginate beads have successfully been used for DNA transfection into microorganisms [1], plants [2, 3], and [4] animal cells. Another important application of calcium alginate beads is protein-immobilized alginate beads. Protein-immobilized alginate beads can be used for oral drug delivery [8], protein characterization [9], etc.

The size of the beads is an important factor for applications of calcium alginate beads, since it have been reported that smaller beads are more biocompatible than larger beads [10] and that lower shear forces due to reduced size may increase their long-time stability [11].

Several methods for producing protein-immobilized calcium alginate beads have been reported in previous studies, such as dropping an alginate solution into a gently stirred calcium chloride solution [12], adding an alginate solution and a calcium chloride solution into a gently stirred oil phase [13], and dropping an alginate solution into a calcium chloride solution containing a surfactant using a high voltage electrostatic generator [14]. However, while some of those methods produce calcium alginate beads less than 200 μm in diameter [14], it is difficult to produce beads under 50 μm with a uniform size. Moreover, protein-retention capacity seriously affects the future applications of protein-immobilized alginate beads.

In this study, we produced protein-immobilized calcium alginate beads with uniform shape smaller than 20 μm in size by using a vibration method. The small beads made by this method are easy to arrange by optical tweezers or laser manipulation. This should open the door to new applications of protein-immobilized calcium alginate beads, such as the development of protein arrays using such alginate particles. To enhance the protein-retention capacity of the bio-beads, the analyte proteins were cross-linked to the alginate carboxyl groups with 1-ethyl-3-(3-dimethylaminopropyl)carbodiimide (EDC) and *N*-hydroxysulfosuccinimide (NHSS). EDC is commonly used for the covalent linking of proteins to other molecules [15], and catalyzes the formation of amide bonds between the carboxylic groups of alginate and the amine groups of proteins. The cross-linking reaction is promoted by NHSS [16]. The beneficial effectiveness of cross-linking on protein retention is demonstrated. In addition, femtosecond laser irradiation of the target calcium alginate beads and laser arrangement of the calcium alginate beads into alphabetical patterns was performed.

2. MATERIALS AND METHODS

Chemical materials Sodium alginate with a viscosity of 100~150 cP, isoamyl alcohol, isopropyl alcohol, 1-ethyl -3-(3-dimethylaminopropyl)carbodiimide (EDC) and *N*-hydroxysulfosuccinimide (NHSS) were purchased from Wako Co. (Osaka, Japan). Bovine serum albumin (BSA) was purchased from Nakalai Tesque Co. (Kyoto, Japan). Bovine serum albumin labeled with fluorescein isothiocyanate (FITC) and anti-bovine serum albumin antibody were purchased from Sigma Co. (St. Louis, MO, USA). EZ-Label™ FITC Protein Labeling Kit was purchased from Takara Co. (Shiga, Japan).

Calcium alginate beads production A solution containing isoamyl alcohol, isopropyl alcohol, and aq. $CaCl_2$ (2:1:1) was added into a 1.5 ml test tube. Sodium alginate solution (alginate concentration: 1 % w/w) containing protein (25 μg/ml FITC-labeled BSA) was forced from a 100 μl syringe (1710RN 100 μl GL Sciences, Tokyo, Japan) by a syringe pump (MSP-RT As One, Osaka, Japan) through a fused silica capillary (30-75 μm) (GL Sciences) at a constant flow rate (0.1-2 μl/min) (Table 1), and dropped into the mixture while vibrating with a loudspeaker (FR-8, 4 Ω, Visaton, Germany) which was connected to a sine wave sound generator (AG-203D Kenwood, Tokyo, Japan) to produce calcium alginate beads (Figure 1). The frequency of the sine wave sound generator was set to 200 Hz. To harvest the calcium alginate beads produced, the test tube was centrifuged at 5,000 rpm for 3 min. The upper isoamyl alcohol phase was discarded, taking care not to remove the calcium alginate beads. After adding 100 mM $CaCl_2$, the suspension was mixed using a micro-tube mixer (CST-040; Asahi Technoglass, Tokyo, Japan) until the precipitated calcium alginate beads were completely re-suspended. Centrifugation was conducted at 5,000 rpm for 3 min. This washing step was repeated at least 3 times, and the final volume was adjusted to 50 μl.

Calcium alginate beads size measurement Calcium alginate beads were produced under 7 different conditions (Table 1). Adequate amounts of calcium alginate beads were re-suspended in a fresh 100 mM $CaCl_2$ solution on a glass slide and digital images of calcium alginate beads were captured through an inverted fluorescent

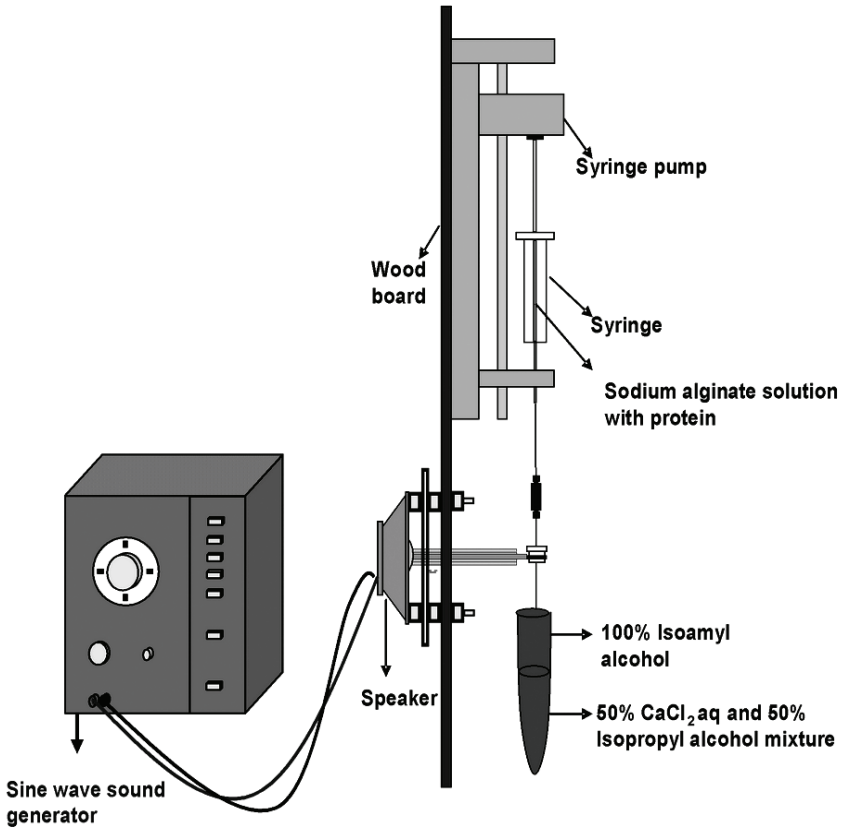

Figure 1. Apparatus for producing calcium alginate beads by the vibration method, comprising a syringe pump for forcing sodium alginate solution from a syringe, a loudspeaker, and a sine wave sound generator.

Table 1. Conditions for calcium alginate beads production.

Conditions	1	2	3	4	5	6	7
Capillary ϕ (μm)	75	75	75	75	75	30	30
Flow rate (μl/min)	2	1	0.8	0.5	0.4	0.2	0.1
Diameter of beads	14.09±1.90	12.96±2.35	11.87±1.91	9.61±1.24	8.77±1.04	8.72±0.62	6.36±1.34
Number of beads measured	52	53	53	53	53	53	54

microscope (IX-70 Olympus, Tokyo, Japan) equipped with an RGB color CCD video camera. The original images of the calcium alginate beads were introduced into a personal computer and the area of each bead in the images was measured with ImageJ® image analysis software. The calcium alginate beads were assumed to be spherical, and their diameters were determined from the projection area. For each condition, at least 100 beads were collected, and of these, 371 isolated beads in total were measured.

BSA and anti-BSA antibody reaction in calcium alginate beads Anti-BSA antibody was labeled with FITC by an EZ-Label™ FITC Protein Labeling Kit according to manufacturer's instructions. BSA (50 μg/ml) protein was immobilized in calcium alginate beads. Calcium alginate beads without protein and calcium alginate beads with non-specific protein Glutathione S-transferase (GST 50 μg/ml) were used as negative controls. After washing 3 times, the beads were collected into three 1.5 ml tubes. Aqueous 5% skim milk was prepared as a blocking solution; since the skim milk was difficult to dissolve, it was centrifuged (4°C, 1,500 rpm, 10 min), and the supernatant was used.

The beads were incubated with 0.5 ml blocking solution for 1 hour. After blocking, the beads were washed 3 times with aq. $CaCl_2$ (100 mM). FITC-antiBSA antibody was diluted 5,000-fold with aq. $CaCl_2$ (100 mM). Into each of the 3 tubes was added 200 μl aq. FITC-antiBSA, followed by incubation for another hour. After washing 3 times, the beads were investigated by using the CCD video camera-equipped fluorescence microscope.

Protein-retention capacity observation EDC and NHSS were added to a sodium alginate solution (1% w/w) to give a final concentration of 2.5 μg/ml EDC and 0.8 μg/ml NHSS. The protein solution (FITC-BSA 25 g/ml) was mixed with this cross-linker-containing alginate solution (1:2 v/v), and stood at room temperature for 15 minutes.

The solution containing isoamyl alcohol, isopropyl alcohol, and aq. $CaCl_2$ (2:1:1) was added into the test tube to generate a $CaCl_2$ concentration gradient. The protein (25 μg/ml FITC-BSA) and aq. alginate (100 μl), with or without cross-linker, was forced from a syringe through a silica capillary by the bead-production instrument (capillary ϕ 75 μl, flow rate 2 μl/min), and dropped into the mixture solution.

The protein-retention capacity was evaluated by analyzing the intensity of fluorescence of each bead's surface. Adequate amounts of calcium alginate beads were re-suspended in a fresh 100 mM $CaCl_2$ solution and placed on a glass slide and digital images of the calcium alginate beads were captured through an inverted fluorescent microscope equipped with the CCD video camera. The original images of the calcium alginate beads were introduced into the personal computer and the intensity value of each bead was analyzed with MATLAB® software. Images of beads were taken at the 3rd day, the 6th day, and the 14th day after bead production. From each sample, the fluorescence intensities of 30~50 beads were measured.

Calcium alginate beads arrangement Sample calcium alginate beads produced by the vibration method were deposited on a 2% 3-aminopropyltrimethoxysilane (APS, Tokyo Chemical Industry Co. Tokyo, Japan)-coated cover glass by a Cytospin centrifuge (Shanpon Cytospin® 4, Thermo Scientific, Cheshire, UK) at 2,000 rpm for 5 min and placed above a target slide glass. A water layer of 100 μm was maintained between the two glasses by a silicone rubber spacer. The source and target substrates were set on an inverted microscope (Olympus), equipped with a 100× objective lens (PLN100XO, NA 1.25, WD 0.15, Olympus). The laser beam from a regeneratively amplified Ti:sapphire laser (Spectra Physics, Hurricane, 800 nm, 120 fs) was introduced to the inverted microscope. The beam diameter was adjusted with collimator lenses to be about 5 mm to match the size of the back aperture of the 100× objective lens, and the laser beam was focused on the image plane of the microscope. The protein-beads were patterned by scanning a motorized microscope stage (BIOS-102T, Sigma Koki, Tokyo, Japan) with a linear velocity of 90 μm/s, while irradiating a focused femtosecond laser pulse train with a repetition rate of 1 kHz. The laser pulse energy was 63 nJ/pulse (**Figure 2**).

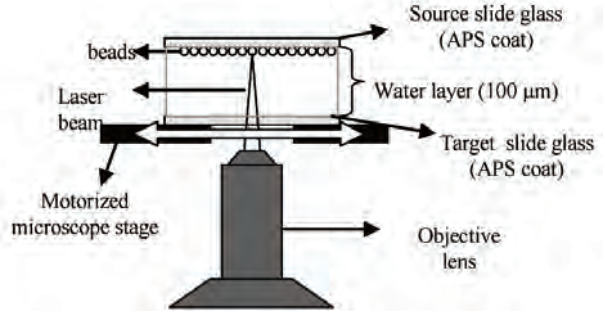

Figure 2. Experimental setup for micro-patterning calcium alginate beads by focused femtosecond laser.

3. RESULTS

Calcium alginate beads production Protein-immobilized calcium alginate beads with uniform size were successfully produced using the bead-production equipment (**Figure 3**). When the bead-production conditions were set as capillary ϕ , 75 μm, and flow rate, 2 μl/min, the average diameter of the calcium alginate beads was approximately 14 μm. At a flow rate of 0.8 μl/min, the size decreased to approximately 12 μm. When the flow rate was further reduced to 0.4 μl/min, the bead size did not change. To get smaller beads, the capillary was changed to 30 μm, and the diameter of most of the beads could be controlled to approximately 5 μm (**Figure 4**, **Table 1**).

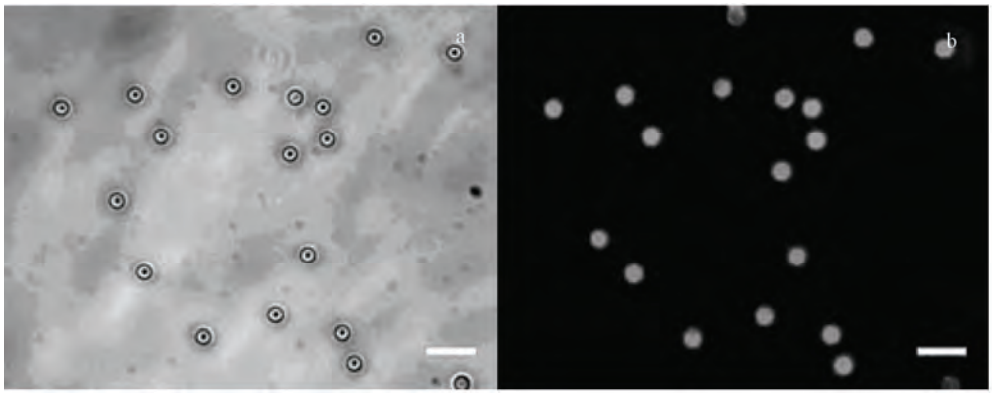

Figure 3. Images of protein-immobilized calcium alginate beads made by the vibration method. Images were photographed under a fluorescent microscope by cooled CCD camera. Bars: 20 μm. (a) microscope image of FITC-BSA-immobilized beads. (b) fluorescence image of the same beads.

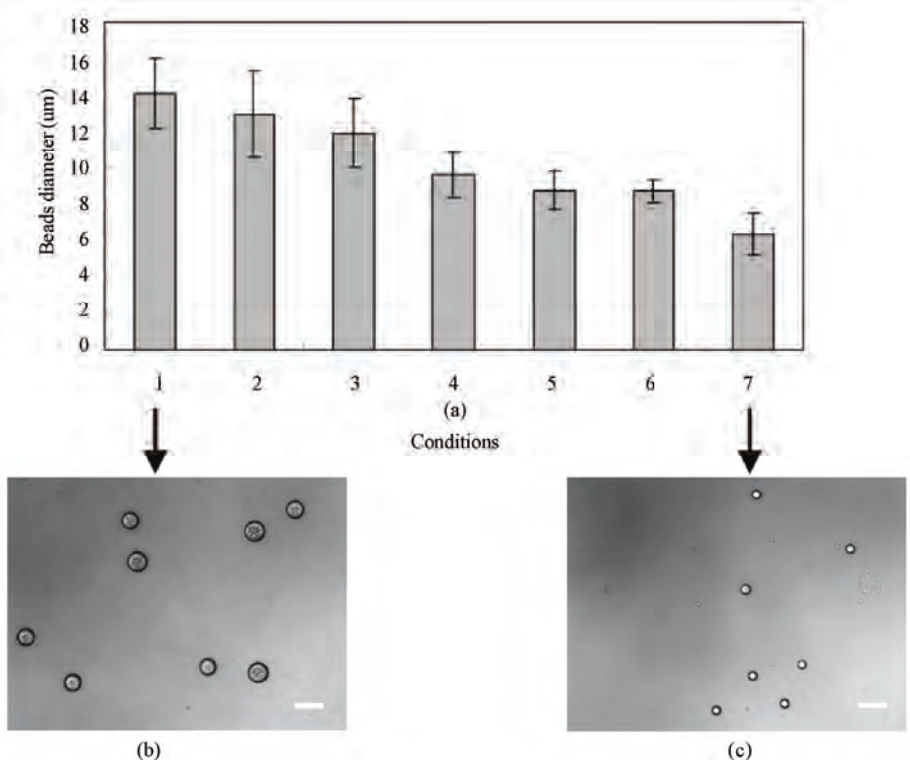

Figure 4. (a) Mean values of the sizes of at least 50 beads for each of 7 different conditions for calcium alginate beads production. Condition 1: capillary ϕ 75 μm, flow rate 2 μl/min. Condition 2: capillary ϕ 75 μm, flow rate 1 μl/min. Condition 3: capillary ϕ 75 μm, flow rate 0.8 μl/min. Condition 4: capillary ϕ 75 μm, flow rate 0.5 μl/min. Condition 5: capillary ϕ 75 μm, flow rate 0.4 μl/min. Condition 6: capillary ϕ 30 μm, flow rate 0.2 μl/min. Condition 7: capillary ϕ 30 μm, flow rate 0.1 μl/min. (b) Calcium alginate beads made under the 1st condition. (c) Calcium alginate beads made under the 7th condition. Bars: 20 μm.

BSA and anti-BSA antibody reaction in calcium alginate beads To confirm that the protein was immobilized in the alginate beads, antigen-antibody reaction in the alginate beads was performed by using BSA and FITC-labeled anti-BSA. Alginate beads without any encapsulated proteins and beads with encapsulated nonspecific protein (GST) were used as negative controls. BSA-encapsulated beads were clearly observed with FITC-labeled anti-BSA antibody under a fluorescence microscope. Almost no fluorescence was detected from GST protein-immobilized calcium alginate beads (**Figure 5(b)**). Weak signals were observed from non-protein calcium alginate beads (**Figure 5(a)**). However the intensity was barely more than a third that of BSA-immobilized calcium alginate beads (**Figure 5(c)**). These results suggest that the protein-immobilized calcium alginate beads would be useful for detecting antigen-antibody reactions.

Protein-retention capacity observation The protein-retention capacity was observed by using 2 types of calcium alginate beads: protein-immobilized alginate beads produced by the vibration method either with or without cross-linking. One group of calcium alginate beads had FITC-BSA cross-linked to the alginate carboxyl groups by EDC and NHSS, whereas the standard beads had no FITC-BSA cross-linking. After analyzing the captured images of the samples, the fluorescence data showed that the small alginate beads made by this vibration method showed a good protein-retention capacity. Two weeks after production of the beads, the image intensity of the standard beads had decreased only 22%, while the intensity reduction of the cross-linked beads was less then 10% (**Figure 6**) and the cross-linked beads could hold more protein than the standard beads. These results suggest that both of the standard beads and protein-cross-linked beads have excellent ability for protein-retention.

Calcium alginate beads arrangement Calcium alginate beads produced by using the vibration method were deposited on an APS (2%)-coated cover glass by centrifugation. The cover glass was placed above another glass slide where the calcium alginate beads would be arranged. A water layer of 100m was maintained between the two glasses by a silicone rubber spacer. The source and target slides were set on an inverted microscope equipped with a 100× objective lens. Laser scanning arranged the beads on the target slide into the pattern "F U K U I" (**Figure 7**). This result suggests that a

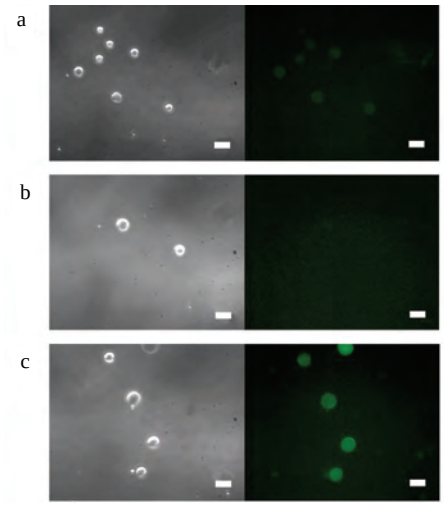

Figure 5. Calcium alginate beads produced by the vibration method. The images were taken under a fluorescence microscope by cooled CCD camera. Bars: 20m. (a) Negative control, calcium alginate beads without any immobilized protein. (b) Negative control, calcium alginate beads with nonspecific protein (GST). (c) calcium alginate beads with immobilized BSA.

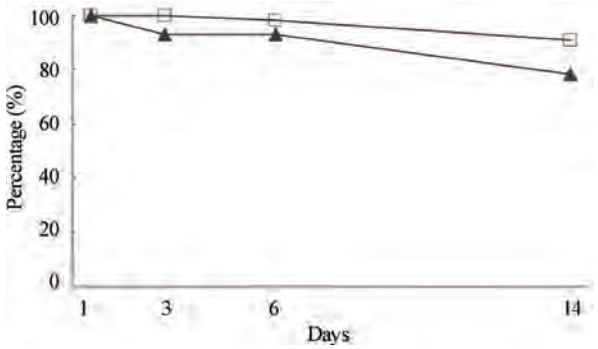

Figure 6. Intensity changes for cross-linked beads and standard beads. Squares, cross-linked beads. Triangles, standard beads.

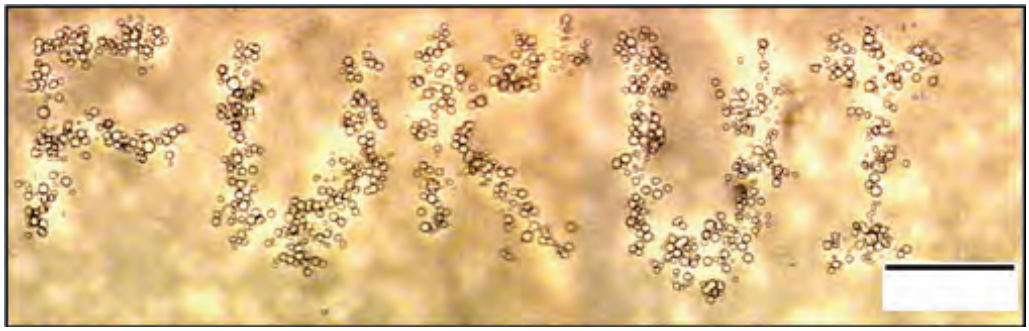

Figure 7. Microsopic image of target slide after laser irradiation with a 63 nJ/pulse energy. Bars: 200 μm.

femtosecond laser could serve as a useful manipulation tool for the arrangement of protein-immobilized calcium alginate beads on glass slides and for future applications of the small alginate beads.

4. DISCUSSION

In previous studies, for alginate beads size control, a droplet generator with a constant electrostatic potential [14,17] showed good potential for size control. The size of the capsules is mainly governed by voltage, flow, and needle diameter [17]. However, since the production of a micro-diameter needle is still difficult, the size adjustment is also limited. In this study, by connecting a flexible silica capillary to the syringe needle, reduction of the needle diameter was achieved. Furthermore, by changing from a droplet generator with constant electrostatic potential to a loudspeaker that was connected to a sine wave sound generator, continuous, smooth and fine vibrations could be generated. Consequently the size of the alginate beads could be controlled very accurately at the micro-scale. Calcium alginate beads in the range of 5 to 20m with a uniform size could be produced by using this new method. Moreover, by reducing the inner diameter of the silica capillary, and slower the flow rate of alginate solution from the syringe, the smaller alginate beads would be the produced.

Besides protein-immobilization, calcium alginate beads are also widely used for cell-immobilization. Reduction in capsule size has been emphasized to enhance mass transfer of both nutrients into encapsulated cells and products from the encapsulated cells out of the capsule. It has been shown that the response time of encapsulated islets to glucose increases with capsule size [18]. Thus the method developed by us might also be used for immobilizing cells. Furthermore, by adjusting the beads' size and the concentration of the cells-containing alginate solution, one cell per one bead should be possible.

Since BSA protein was successfully immobilized in the calcium alginate beads, and the reaction with FITC labeled anti-BSA was detected successfully by using alginate beads, this indicated that the protein- immobilized alginate beads have the potential to be used to detect antigen-antibody reactions.

Previously, a serum albumin-alginate membrane has been used for coating alginate beads to reduce protein diffusion [19]. However, in this report, even when the beads were coated, over 80% of the protein diffused within 8 days. However, by cross-linking the protein to the alginate, the protein diffusion could be reduced to less than 10% over 14 days. The data also showed that, even without cross-linking, the alginate beads produced by using the vibration method have a high ability for protein-retention.

In conclusion, we have succeeded in the development of a method for producing size- and shape-controlled calcium alginate beads with immobilized proteins. The protein-immobilized calcium alginate beads produced have a small and uniform size, can retain protein within the beads for long periods, are easy to manipulate, and are useful for the detection of antigen-antibody interactions. Therefore the alginate beads production method reported here should find wide application in many biotechnological fields.

5. ACKNOWLEDGEMENTS

This work was supported in part by a grant from the Cooperative Link of Unique Science and Technology for Economy revitalization promoted by MEXT, Japan, to K. F.

REFERENCES

[1] Mizukami, A., Nagamori, E., Takakura, Y., Matsunaga, S., Kaneko, Y., Kajiyama, S., Harashima, S., Kobayashi, A., and Fukui, K., (2003) Transformation of yeast using calcium alginate microbeads with surface-immobilized chromosomal DNA, Biotechniq., **35**, 734–736, 738–740.

[2] Liu, H., Kawabe, A., Matsunaga, S., Murakawa, T., Mizukami, A., Yanagisawa, M., Nagamori, E., Harashima, S., Kobayashi, A., and Fukui, K., (2004) Obtaining transgenic plants using the calcium alginate beads method, J. Plant Res., **117**, 95–99.

[3] Sone, T., Nagamori, E., Ikeuchi, T., Mizukami, A., Takakura, Y., Kajiyama, S., Fukusaki, E., Harashima, S., Kobayashi, A., and Fukui K., (2002) A novel gene delivery system in plants with calcium alginate micro-beads, J. Biosci. Bioeng., **94**, 87–91.

[4] Higashi, T., Nagamori, E., Sone, T., Matsunaga, S. and Fukui, K. (2004) A novel transfection method for mammalian cells using calcium alginate microbeads, J. Biosci. Bioeng., **97**, 191–195.

[5] Gray, C. J. and Dowsett, J., (1988) Retention of insulin in alginate gel beads, Biotech. Bioeng., **31**, 607–612.

[6] Ko, C., Dixit, V., Shaw, W., and Gitnick, G., (1995) In vitro slow release profile of endothelial cell growth factor immobilized within calcium alginate microbeads, Artif. Cells Blood Substit Immobil. Biotechnol., **23**, 143–151.

[7] Smidsrød, O. and Skjåk-Braek, G., (1990) Alginate as immobilization matrix for cells, Trends Biotechnol., **8,** 71–78.

[8] Puolakkainen, P. A., Ranchalis, J. E., Gombotz, W. R., Hoffman, A. S., Mumper, R. J., and Twardzik, D. R., (1994) Novel delivery system for inducing quiescence in intestinal stem cells in rats by transforming growth factor beta 1, Gastroenterology, **107**, 1319–1326.

[9] Singh, O. N. and Burgess, J., (1989) Characterization of albumin-alginic acid complex coacervation, J. Pharm. Pharmacol., **41**, 670–673.

[10] Robitaille, R., Pariseau, J. F., Leblond, F. A., Lamoureux, M., Lepage, Y., and Hallé, J. P., (1999) Studies on small (<350 microm) alginate-poly-L-lysine microcapsules. III. Biocompatibility of smaller versus standard microcapsules, J. Biomed. Mater. Res., **44**, 116–120.

[11] Poncelet, D. and Neufeld R. J., (1989) Shear breakage of nylon membrane microcapsules in a turbine reactor, Bio-

technol. Bioeng., **5**, 95–103.

[12] Sakai, S., Ono, T., Ijima, H., and Kawakami, K., (2000) Synthesis and transport characterization of alginate/ aminopropyl-silicate/alginate microcapsule: application to bioartificial pancreas, Biomater., **22**, 2827–2834.

[13] Srivastava, R. and McShane, M. J., (2005) Application of self-assembled ultra-thin film coatings to stabilize macromolecule encapsulation in alginate microspheres, J. Microencapsul., **22**, 397–411.

[14] Wang, S. B., Chen, A. Z., Weng, L. J., Chen, M. Y., and Xie, X. L., (2004) Effect of drug-loading methods on drug load, encapsulation efficiency and release properties of alginate/poly-L-arginine/chitosan ternary complex microcapsules, Macromol. Biosci., **4**, 27–30.

[15] Timkovich, R., (1997) Detection of the stable addition of carbodiimide to proteins, Anal. Biochem., **179**, 135–143.

[16] Grabarek, Z. and Gergely, J., (1990) Zero-length cross-linking procedure with the use of active esters, Anal. Biochem, **185**, 131–135.

[17] Strand, B. L., Gåserød, O., Kulseng, B., Espevik, T., and Skjåk-Baek, G., (2002). Alginate-polylysine-alginate microcapsules: effect of size reduction on capsule properties, J. Microencapsul., **19**, 615–30.

[18] Chicheportiche, D. and Reach, G., (1988) In vitro kinetics of insulin release by microencapsulated rat islets: effect of the size of the microcapsules, Diabetologia., **31**, 54–57.

[19] Hurteaux, R., Edwards-Lévy, F., Laurent-Maquin, D., and Lévy, M. C., (2005) Coating alginate microspheres with a serum albumin-alginate membrane: application to the encapsulation of a peptide, Eur. J. Pharm. Sci., **24**, 187–197.

J. Biomedical Science and Engineering, 2009, 2, 294-303 **JBiSE**
doi: 10.4236/jbise.2009.25044 Published Online September 2009 (http://www.SciRP.org/journal/jbise/).

Sleep spindles detection from human sleep EEG signals using autoregressive (AR) model: a surrogate data approach

Venkatakrishnan Perumalsamy[1], Sangeetha Sankaranarayanan[2], Sukanesh Rajamony[3]

[1]Department of Information Technology, Thiagarajar College of Engineering, Madurai, India; [2]Department of Electrical and Electronics Engineering, Sethu Instituite of Technology, Madurai, India; [3]Department of Electronics and Communication Engineering, Thiagarajar College of Engineering, Madurai, India.
Email: pvkit@tce.edu; viggee_tce2000@yahoo.co.in; rshece@tce.edu

Received 5 May 2009; revised 19 July 2009; accepted 29 July 2009.

ABSTRACT

A new algorithm for the detection of sleep spindles from human sleep EEG with surrogate data approach is presented. Surrogate data approach is the state of the art technique for nonlinear spectral analysis. In this paper, by developing autoregressive (AR) models on short segment of the EEG is described as a superposition of harmonic oscillating with damping and frequency in time. Sleep spindle events are detected, whenever the damping of one or more frequencies falls below a predefined threshold. Based on a surrogate data, a method was proposed to test the hypothesis that the original data were generated by a linear Gaussian process. This method was tested on human sleep EEG signal. The algorithm work well for the detection of sleep spindles and in addition the analysis reveals the alpha and beta band activities in EEG. The rigorous statistical framework proves essential in establishing these results.

Keywords: AR Model; LPC; Sleep Spindles; Surrogate Data

1. INTRODUCTION

Oscillatory signal activities are ubiquitous in the biomedical signals [1]. Multielectrode recordings provide the opportunity to study signal oscillations from a network perspective. To assess signal interactions in the frequency domain, one often applies methods, such as ordinary coherence and Granger causality spectra [2] that are formulated within the frame work of linear stochastic process. Electroencephalogram (EEG) is one of the most important electrophysiological techniques used in human clinical and basic sleep research. In 1979 Barlow proposed linear modeling system which has a long-lasting history in EEG analysis [3]. The models are mainly considered as a mathematical description of the signal and less as a biophysical model of the underlying neuronal mechanisms.

In 1985, Frannaszczua *et al*. [4] proposed a model to interpret linear models as damped harmonic oscillators generating EEG activity based on the equivalence between stochastically driven harmonic oscillators and autoregressive (AR) models. There is a unique transformation between the AR coefficients and the frequencies and damping coefficients of the corresponding oscillators. In particular at times when the EEG is dominated by a certain rhythmic activity e.g. in the case of sleep spindles or alpha activity, on might expect, that this activity will be rejected by a pole with a corresponding frequency and low damping. This idea was the staring point of our analysis [5].

The sleep EEG is always not stationary. However, we demonstrated that the effects of non stationary become relevant only with scales longer than 1s [6]. Therefore, short segments with duration of around 1s are sufficiently described by linear models. The non stationary in longer time scales might be rejected by the variation of the AR-coefficients and thus by the corresponding frequencies and damping coefficients. Based on the above considerations we propose an easy way to define oscillatory events. They are detected, whenever the damping of one of the poles of a 1s AR model is below a predefined threshold.

The method of surrogate data is a tool to test whether data were generated by some class of model. In 1992 the method of surrogate data proposed by Theiler *et al*. [7] is a general procedure to test whether data are consistent with some class of models. In order to test the hypothesis that the data are consistent with being generated by a linear system, the Fourier Transform (FT) algorithm is applied. Based on a example and the theory of linear stochastic systems we will show that this algorithm produce correct

distribution of time series and therefore might not generally yield the correct distribution of the test statistics. The surrogate data method differs from a simple Monte Carlo implementation of a hypothesis test in that it tests not against a single model, but a class of models, i.e. linear systems driven by Gaussian noise. The idea is to select single model from the class on the basis of the measured data x, and then do a Monte Carlo hypothesis test for the selected model and the original data.

The statistical properties of a time series generated by a linear process are specified by the autocovariance function (ACF) or equivalently by its Fourier Transform, the power spectrum X (ω). The purpose of this study is described as even without a rigorous mathematical foundation it is possible to detect sleep spindles as well as alpha and beta activities from human sleep EEG. The theoretical framework of AR model and the procedure to generate the surrogate data are given in Section 2. The method is then tested on one simulation data set in Section 3. Section 4 describes sleep spindles detection using AR model with surrogate data approach. Results are discussed and summarized in Section 5.

2. METHODS

In this section, we start with AR model of order p and then proceed to outline the procedure for generating surrogate data.

2.1. AR Model

The Parametric description of the EEG signal by means of the AR model makes possible estimation of the transfer function of the system in the straight forward way. From the transfer function it is easy to find the differential equation describing the investigated process. Our detection algorithm is based on modeling 1s segments of the EEG time series using autoregressive (AR) models of order p. From the AR (p)-model

$$\sum_{j=0}^{p} a_j x_{n-j} = \in_n \tag{1}$$

where

a_j - Coefficients of the model (a_0 =1)

x_n - The value of the sampled signal at the moment n

ε_n - Zero mean uncorrelated white noise process.

Applying the Z-transform to **Eq.1** we obtain:

$$A(z)X(z) = E(z) \tag{2}$$

where

$$A(z) = \sum_{j=0}^{p} a_j z^{-j} \tag{3}$$

X(z)-the Z-transform of the signal x
E(z)-the Z-transform of the noise.
If the system is stable, there exists $A^{-1}(z)$ and we get

$$X(z) = A^{-1}(z)E(z) \tag{4}$$

In the z domain this filter is expressed by the **Eq.4** where $A^{-1}(z)$ is the transfer function. Denoting it by H(z) and writing if explicitly we obtain:

$$H(z) = A^{-1}(Z) = 1/\sum_{j=0}^{p} a_j z^{-j} \tag{5}$$

Multiplying numerator and denominator z^p we get

$$H(z) = z^p / \sum_{j=0}^{p} a_j z^{p-j} \tag{6}$$

Factorizing the denominator gives the formula

$$H(z) = z^p / \prod_{j=1}^{p} (z - z_j) \tag{7}$$

where $z_j = r_k e^{i\varphi k}$

Using the above formula to estimate the frequencies $f_k = \varphi_k / (2\pi\Delta)$ and damping coefficients $\gamma_k = -\Delta^{-1} lnr_k$ (Δ Denotes the sampling interval).

We assume that there are only single poles of H (Z) which can be written in the form

$$H(z) = \sum_{j=1}^{p} c_j (z / z - z_j) \tag{8}$$

For the single pole coefficients c_j can be found according to the formula:

$$c_j = \lim_{z \to z_j} \frac{(z - z_j)H(z)}{z} \tag{9}$$

By means of the inverse transform $-z^{-1}$ from the **Eq.8** the impulse response of the system: h (n) can be found. Since from the properties of the z^{-1} transform we know that $z^{-1}(z / z - z_j)) = \exp(n.lnz_i)$ we obtain:

$$h(n) = z^{-1}(H(z)) = \sum_{j=1}^{p} c_j \exp(n.lnz_j) \tag{10}$$

If the sampling interval Δt was chosen according to the Nyquist theorem we can express the impulse response as continuous function and write it in the form:

$$h(t) = \sum_{j=1}^{p} c_j \exp(\frac{t}{\Delta t}.lnz_j) = \sum_{j=1}^{p} c_j \exp(a_j t) \tag{11}$$

where

t = Δt*n $a_j = \frac{lnz_j}{\Delta t}$

Laplace transform of the **Eq.11** which corresponds to the transfer function H(s) of the continuous system is given by the formula:

$$H(s) = \sum_{j=1}^{p} c_j \frac{1}{s - a_j} \tag{12}$$

The above expression can be obtained directly from **Eq.8**

by means of the integral transform z. **Eq.12** can be written as a ratio of two polynomials of the order p-1 and p

$$H(s)=\frac{b_{p-1}s^{p-1}+\cdots+b_1s+b_o}{c_ps^p+\cdots+c_1s+c_o} \quad (13)$$

The polynomial coefficients can be readily calculated from c_j and a_j. This form of the transfer function was found also by Freeman 1975. It leads directly to the differential equations describing the system. The transfer function is the ratio of the Laplace transform of input y(t) and output x(t) functions:

$$H(s)=\frac{X(s)}{Y(s)}=\frac{L(x(t))}{L(y(t))} \quad (14)$$

Since variable s corresponds to the operator $\frac{d}{dt}$, from **Eq.13 and 14** we get:

$$c_p\frac{d^p}{dt^p}x(t)+\cdots+c_1\frac{d^1}{dt^1}x(t)+c_0x(t)$$
$$=\frac{d^{p-1}}{dt^{p-1}}y(t)+\cdots+b_1\frac{d^1}{dt^1}y(t)+b_0y(t) \quad (15)$$

In this way we have obtained the differential equation describing the system which is free of the arbitrary parameters. Its order is determined by the characteristic of the signal and may be found from the criteria based on the principle of the maximum of entropy.

2.2. Surrogate Data Method

Generally, a surrogate data testing method involves three ingredients: 1) a null hypothesis; 2) a method to generate surrogate data; and 3) testing statistics for significance evaluation. The null hypothesis in the present study is that investigated data from a linear Gaussian process. If the null hypothesis is rejected, then we conclude that the data are either non-Gaussian or come from nonlinear process. The surrogate data are generated in such a way that it is Gaussian distributed but has the same second order spectral properties (in the bivariate, auto spectra) as the original data. The testing statistics the amplitude of the peridogram we will give the steps for generation the surrogate data and the theoretical rationale behind the steps [8].

Consider two zero mean stationary random processes x(t) and y(t). These processes may or may not be linear Gaussian processes. Their one-sided auto spectra S_{xx} and S_{yy} can be estimated [9].

$$S_{xx}(f)=2\lim_{T\to\infty}\frac{1}{T}E[|X_k(f,T)|^2]$$
$$S_{yy}(f)=2\lim_{T\to\infty}\frac{1}{T}E[|Y_k(f,T)|^2] \quad (16)$$

where T is the duration of the data, the expectation is taken over multiple realizations and X_k and Y_k are the Fourier Transform of x(t) and y(t). Now we consider how to generate two zero-mean linear Gaussian processes $x'(t)$ and $y'(t)$ which have the same second order statistical properties as x(t) and y (t). Let X'_k and Y'_k expressed in real and imaginary parts, X'_R, X'_I, Y'_R and Y'_I, these Fourier Transforms are

$$X'_k(f)=X'_R(f)-j.X'_I(f)$$
$$Y'_k(f)=Y'_R(f)-j.Y'_I(f) \quad (17)$$

Since $x'(t)$ and $y'(t)$ are normally distributed with zero mean values, X'_R, X'_I, Y'_R and Y'_I are also normally distributed with zero means [9]. The covariance matrix ($\sum$) of X'_R, X'_I, Y'_R and Y'_I should be selected such that the auto-spectra and cross spectra of $x'(t)$ and $y'(t)$ are the same as those of the original data, i.e, $S'_{xx}=S_{xx}$ and $S'_{yy}=S_{yy}$

In practice, S_{xx} and S_{yy} estimated from the data. The question is how to draw Gaussian variables for X'_R, X'_I, Y'_R and Y'_I such that $S'_{xx}=S_{xx}$ and $S'_{yy}=S_{yy}$. It can be shown that the relation between X'_R, X'_I, Y'_R and Y'_I and S'_{xx} and S'_{yy} are as follows [10].

$$E[X'_RX'_I]=E[Y'_RY'_I]=0$$
$$E[X'_RX'_R]=E[Y'_IY'_I]=\left(\frac{T}{4}\right)S'_{xx}$$
$$E[Y'_RY'_R]=E[Y'_IY'_I]=\left(\frac{T}{4}\right)S'_{yy} \quad (18)$$

According to these relations the covariance matrix ($\sum$) for the real and imaginary parts of X'_k and Y'_k for each frequency is

$$\sum_x=E\left[\begin{pmatrix}X'_R\\X'_I\end{pmatrix}(X'_RX'_I)\right]=\frac{T}{4}\begin{pmatrix}S_{xx}&0\\0&S_{xx}\end{pmatrix}$$
$$\sum_y=E\left[\begin{pmatrix}Y'_R\\Y'_I\end{pmatrix}(Y'_RY'_I)\right]=\frac{T}{4}\begin{pmatrix}S_{yy}&0\\0&S_{yy}\end{pmatrix} \quad (19)$$

Choosing $S'_{xx}=S_{xx}$ and $S'_{yy}=S_{yy}$ and X'_R, X'_I, Y'_R and Y'_I are then generated by sampling from a Gaussian distribution with zero mean and covariance matrix$\sum$. Once X'_R, X'_I, Y'_R and Y'_I are generated for each frequency, the surrogate data $x'(t)$ and $y'(t)$ are the inverse Fourier Transform of $X'_k(f)=X'_R(f)-j.X'_I(f)$ and $X'_k(f)=X'_R(f)-j.X'_I(f)$

For easy implementation, we summarize the earlier analysis as follows.

Step 1) Estimate S_{xx} and S_{yy} for original data according to (16)

Step 2) Calculate Covariance matrix $\sum$ according to (19)

Step 3) Draw values (realizations) of X'_R, X'_I, Y'_R and Y'_I from the Gaussian processes with zero mean and covariance matrix ($\sum$) for each frequency. This can be done for example Matlab function based on the ziggurat method [11].

Step 4) Take the inverse Fourier Transform of X'_k and Y'_k to obtain the surrogate data $x'(t)$ and $y'(t)$. To ensure surrogate data are real valued, the negative frequency parts of X'_k and Y'_k are taken as the complex conjugate of the positive frequency parts.

Step 5) Repeat Steps 3) and 4) to generate multiple realizations of the surrogate data.

X'_R and Y'_I, could be drawn from Gaussian distribution with zero mean and covariance matrix $\sum_x$. This simplified method is similar to the method proposed by Timmer [12]. The probability density function for the extreme value distribution (type I) with location parameter μ and scale parameter is σ [13].

$$y = \frac{1}{\sigma}\exp(-\exp(-\frac{x-\mu}{\sigma})-\frac{x-\mu}{\sigma}) \quad (20)$$

The exact PDF is determined once μ and σ are known. From this distribution, one can determine the threshold for any desired significance level (i.e. -p value).

3. SIMULATION EXAMPLE

We have performed simulation studies to test the effectiveness of the method proposed before. Matlab "Signal processing and Spectral analysis toolbox" is used in our analysis.

3.1. Linear Bivariate AR Model Driven by Gaussian White Noise

The model is written as

$$\begin{aligned} x(t) &= 0.8*x(t-1)-0.5x(t-2)+\varepsilon(t) \\ y(t) &= 0.6x(t-5)+\eta(t) \end{aligned} \quad (21)$$

where $\varepsilon(t)$ and $\eta(t)$ are uncorrelated Gaussian white noise with zero means and unit variances. The data set consists of M=50 realizations where each realization is of length K=512. For sampling frequency of 128Hz, each realization has the duration of 4s. To perform the test P =1500 surrogate data sets were generated following the procedure in Section 2.

The one sided power spectra S_{xx} and S_{yy} for both original (solid curve) and one set of surrogate data (dotted curve) are shown in **Figure 1**. It is seen that the surrogate data's spectra nearly match well with that of the original data. This is an expected result. The maximum amplitude for x(t) original power spectra is 30.1891 [**Figure 1(a)**] and that for surrogate data x′(t) power spectra is 32.6881. Similarly the maximum amplitude for y(t) original power spectra is 28.5673 [**Figure 1(b)**] and that for surrogate data y′(t) power spectra is 29.8921. Notice that the power spectra amplitude is higher between 0 to 30 Hz than other regions. Namely, the estimation variances are proportional to the power spectral amplitudes as those frequencies. Considering that the surrogate data contour plots are computed based on a randomly selected data set among P=1500 available, these maximum value comparisons suggests the known fact that there are no nonlinear or non-Gaussian components in the original data. The histogram and Gaussian fit of input data x(t) and y(t) and surrogate data x′(t) and y′(t) are generated by ziggurat algorithm shown in **Figure 2**. The PDFs are obtained from these parameters

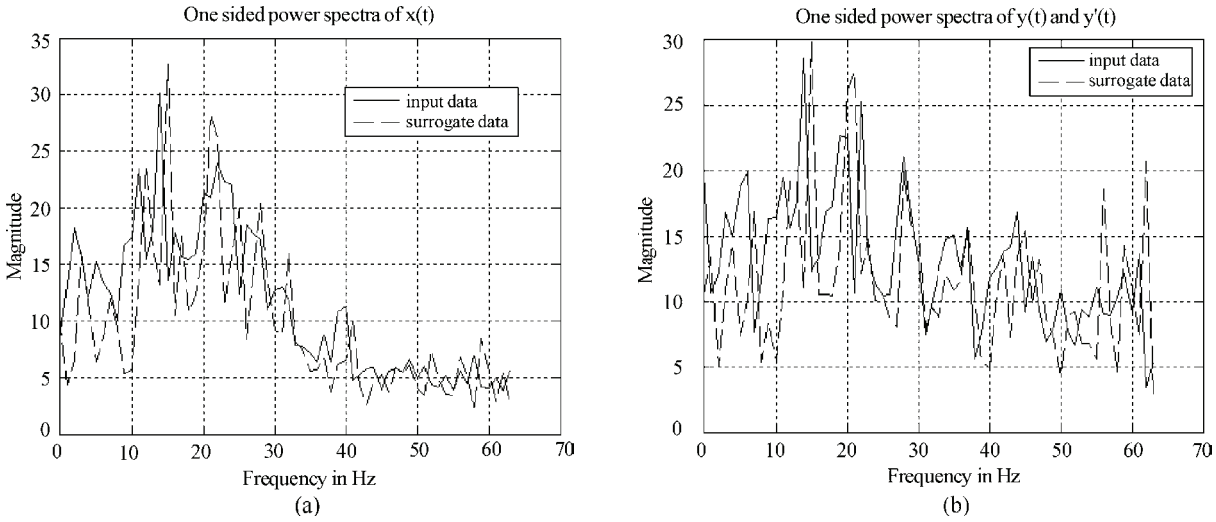

Figure 1. One sided power spectra of a) $x(t)$ *and* $x'(t)$ b) $y(t)$ *and* $y'(t)$.The solid curve indicates the result from the original data and the dotted curve indicates the result from one of the 1500 surrogate data sets.

according to **Eq.20** and are plotted along with the histogram in blue color in **Figure 3**. Notice that the PDF here are multiplied by the total number of surrogate data sets (1500) to match the histogram. From the PDFs, the threshold for a significance level of $p < 0.005$. By comparing the original data's maximum power spectra values with the thresholds, it can be seen from the null hypothesis that the original data coming from a linear Gaussian processes cannot be rejected, a theoretically expected result.

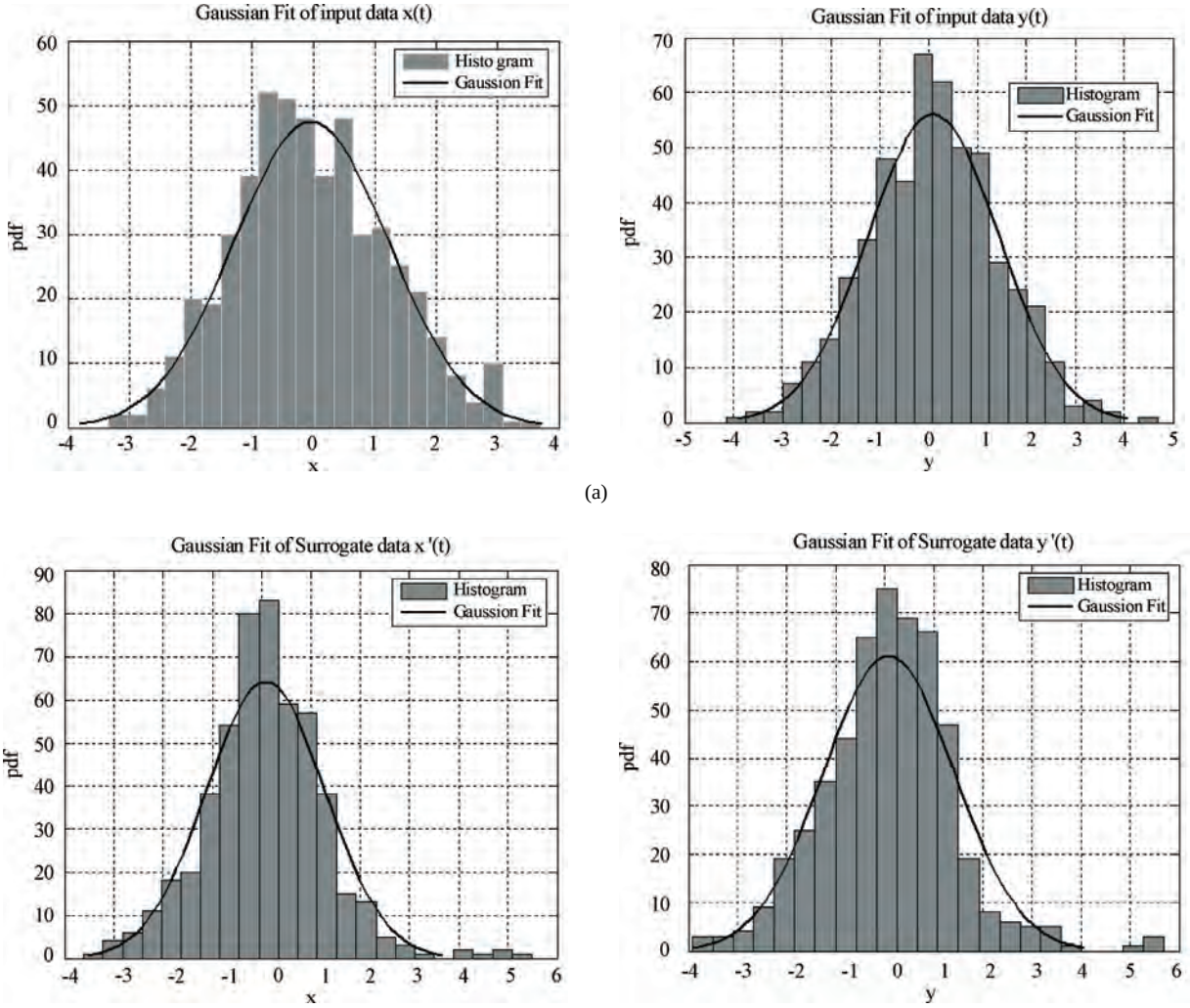

Figure 2. Histogram and Gaussian fit of the a) original and b) surrogate data.

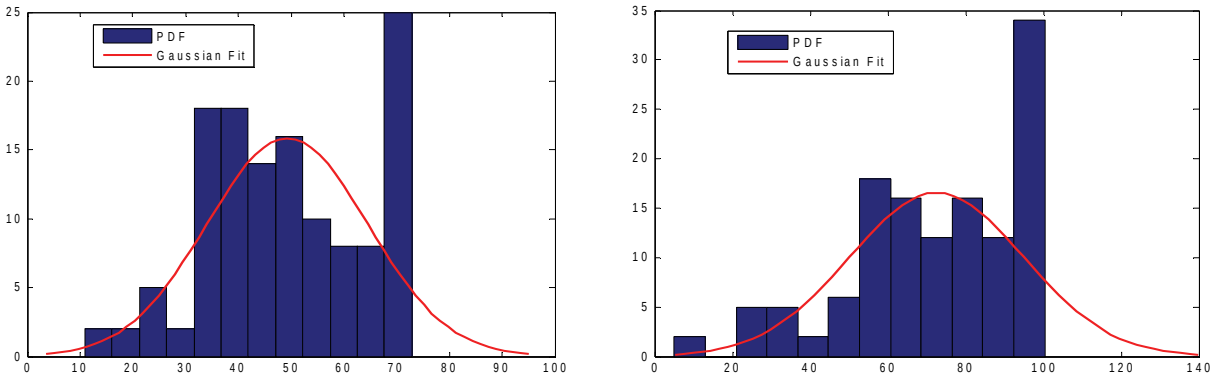

Figure 3. PDF of original power spectra and the surrogate data power spectra with Gaussian Fit.

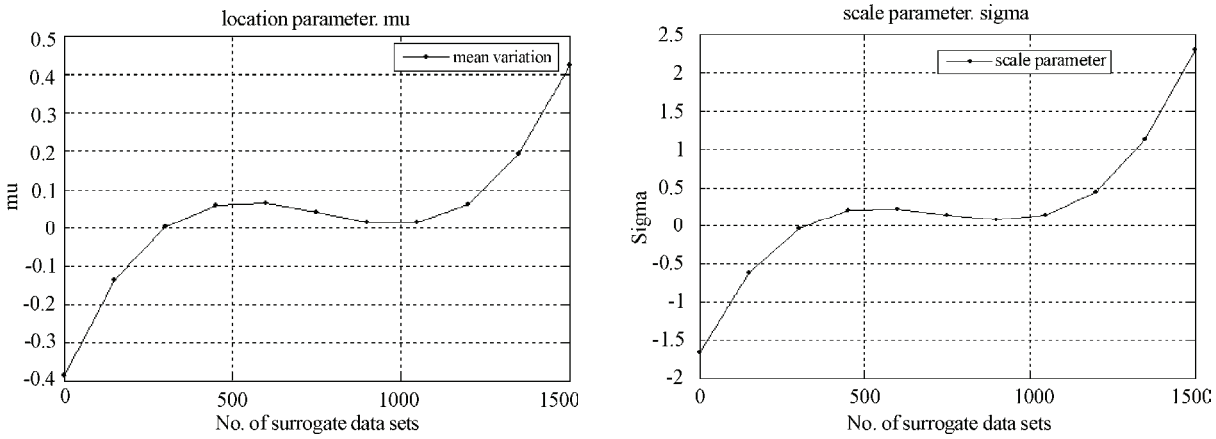

Figure 4. μ and σ versus the number of surrogate data sets.

We have also performed a study to examine whether fitting an extreme value distribution to the empirical histogram is a viable approach. The fitted model parameters μ and σ versus the number of surrogate data sets used are plotted in **Figure 4**. It can be seen after around 500 surrogate data sets, the estimation becomes linear.

4. SLEEP SPINDLES DETECTION

A seven minutes recording of 9 channels of EEG (C3, A2, O1, O2, C4, P3, P4, F3, and F4) was used in our test (16,207 trials) shown in **Figure 5**. Precise numbers of sleep stages and standard characteristics derived form hypnograms are in **Table 1**. Number of sleep stages (17s records) are in the first column; data in the second column are the average values over 5 subjects (C3A2, C4P4, F3C3, P3O1, P4O2) related to total sleep time, the beginning of sleep is set as the first appearance of the sleep Stage 2. Sleep efficiencies is the ratio of time spent in Stages 1-4 or REM sleep to the whole sleep time, where also movement time and some awakenings during the night are included; in sleep medicine this parameter discriminates some sleep disorders. Surrogate data were generated following the procedure in Section 2.

The EEG derivation C3A2 and C4P4 was analyzed shown in **Figure 6**. Oscillatory events are detected, if the damping coefficients r_k falls above a pre defined threshold and hence r_k, exceeds the corresponding threshold. In practice, we use two thresholds, a lower one, r_a, to detect candidate events scanning the EEG with non-overlapping 1-s segments. When r_a is crossed we go back to the previous segment and use a smaller step size of 1/16s (overlapping 1-s segments). If r_k exceeds a second threshold $r_b > r_a$ the beginning of an oscillatory events is detected.

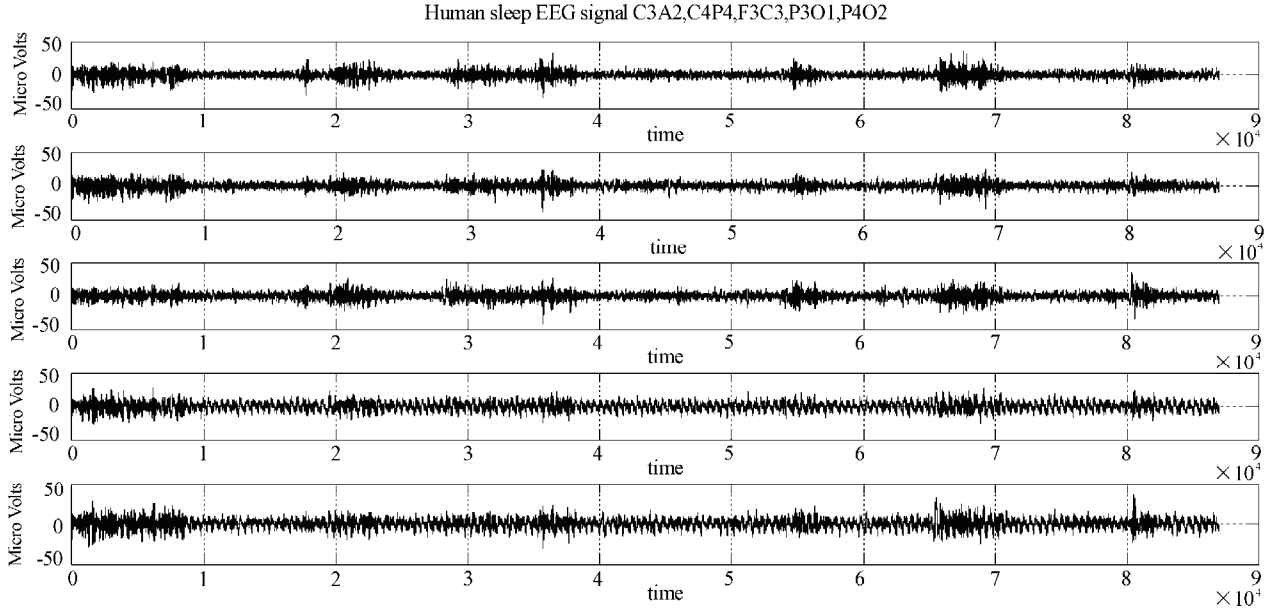

Figure 5. Human sleep EEG signals (9 channels C3, A2, O1, O2, C4, P3, P4, F3, and F4).

Table 1. Number of sleep stages (first column) and sleep efficiency and average percentage of sleep stages during the sleep (mean ± standard deviation).

Total	16,207	Sleep Efficiency[%]: 92.6 ± 5.3	
Waking	761	% Waking	8.0 ± 3.2
Stage 1	809	% Stage 1	6.9 ± 1.4
Stage 2	8024	% Stage 2	46 ± 7.3
Stage 3	1536	% Stage 3	9.3 ± 4.2
Stage 4	1753	% Stage 4	10.9 ± 2.6
REM Sleep	3217	% REM Sleep	17.9 ± 3.6
Movement time	107	% Movement time	0.7 ± 0.6

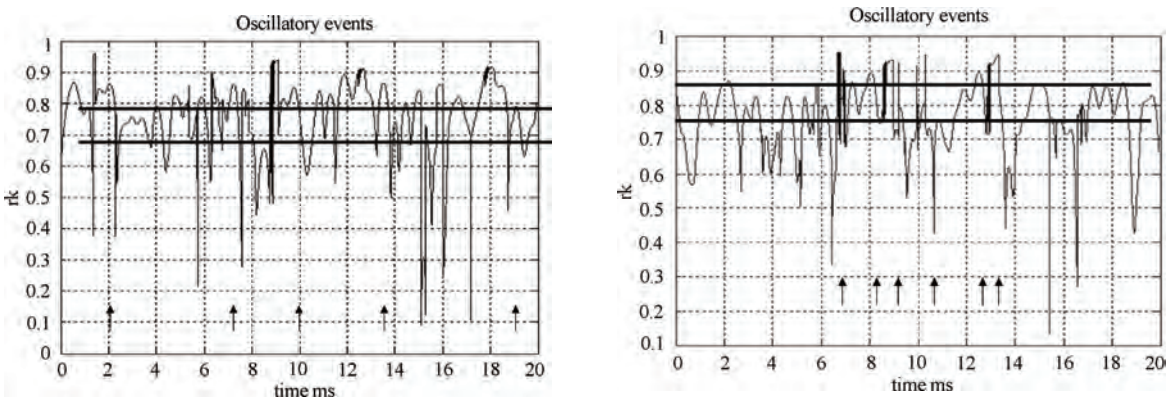

(a) (b)

Figure 6. Sleep spindles detection for a) C3A2 and b) C4P4 channel (arrow mark representation).

The oscillatory events are terminated by the time r_k is lower than r_b for the last time before it falls below r_a. The frequency and time at the position of the maximal value r_{max} are considered as the frequency and occurrence of the event respectively. Spindles or Sigma waves are a poor indicator for sleep onset. Some subjects do not have discernable sigma waves. These spindles are more prominent in Stage 2 than Stage 1. In the present analysis the order of the AR model was set to p=8 and the threshold \value set to r_a=0.75 and r_b=0.85 parameter were chosen in such a way, that clearly visible sleep spindles were reliable detected by the algorithm. Sleep stages were visually scored according to standard criteria in **Figure 7**.

In **Figure 7** shows the detected events from 2 recordings. The distributions show modes in four stages: in the delta (±1:0-2 Hz), in the fast delta (±2: 2-4 Hz), in the alpha (®: 8-12 Hz) and sigma (sleep spindles: 11.5-16 Hz) bands. These modes are also evident in the distribution of the events in the different sleep stages (**Figure 7**). Alpha waves predominate in waking, spindles in Stage 2 while the occurrence of delta waves decreases from Stage 2 to Stage 4 (deepening of sleep). Delta waves are the prevalent events in REM sleep and Stage 1. Note that they also occur in Stage 2 with almost the same incidence. Events in the alpha frequency range correspond to continuous alpha activity during waking and to small amplitude, sometimes spindle-like activity in NREM sleep. However, in particular during NREM sleep Stages 3 and 4, slow waves are often not detected as oscillatory events because they yield a relaxatory pole (frequency zero) in the AR-model. **Table 2** provides detection of different frequency bands and their amplitude calculated from the Fast Fourier Transform.

Table 2. Different frequency band detection and the corresponding true value determined from one sided Power spectra.

S.No	Wave	Bandwidth (Hz)	Time range (sec)	Amplitude (μV)
1	Delta	0, 1-4	0-5	10-30
2	Theta	4-8	5-9	30-70
3	Alpha	8-12	9-13	> 70
4	Beta	> 12	13 – 16	< 100
5	Sleep Spindles (sigma)	11.5 – 16	16-20	< 50

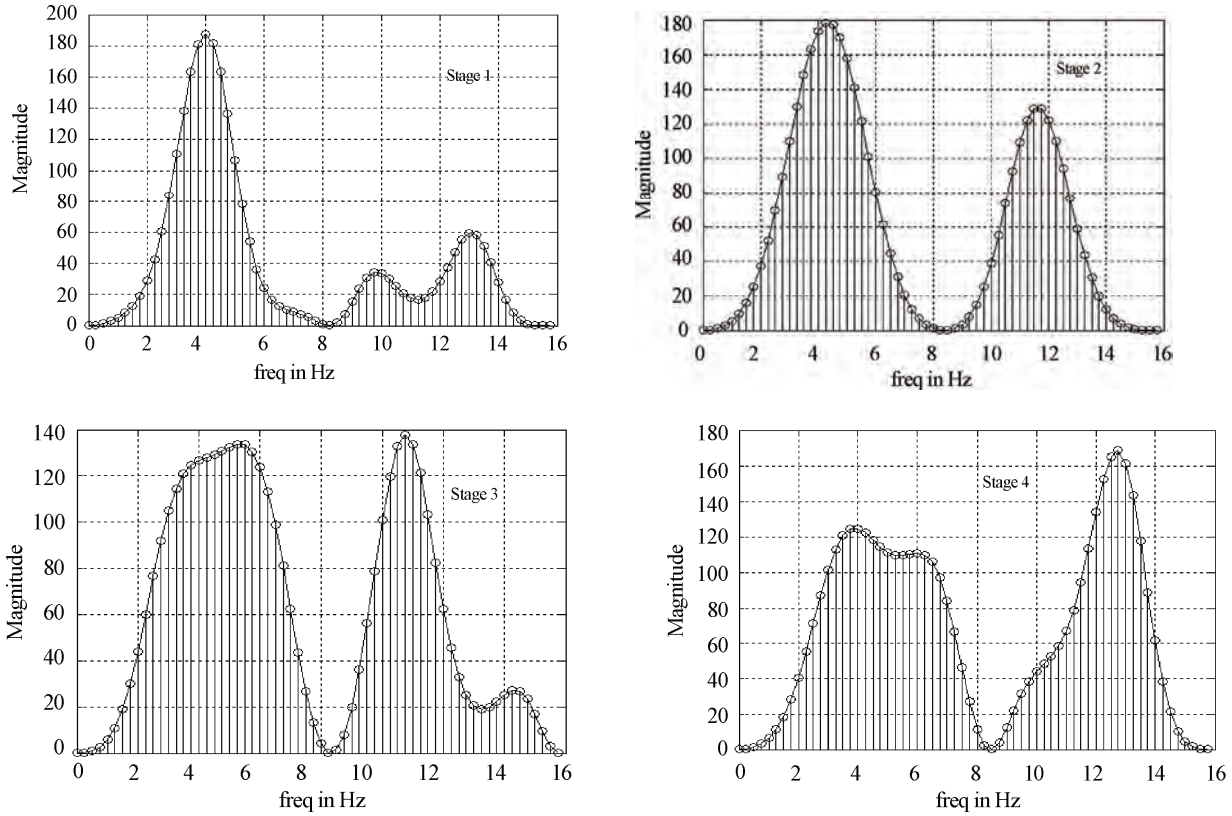

Figure 7. Sleep stages from Stage 1-Stage 4.

The two most important characteristics of EEG elements are frequency and amplitude. Frequency is inverse value of duration of EEG segment. The frequency range is divided in to four bands: beta (12Hz and higher), alpha (8-12Hz), theta (4-8Hz) and delta (0, 1-4Hz). Amplitude of EEG is taken as the peak to peak value. After the magnitude of amplitude EEG signal is divided into low-voltage, middle and high- voltage EEG. For delta, theta and alpha bands these values are following: 10-30 μV for low voltage, 30-70 μV for middle voltage and above 70 μV for high voltage EEG. For beta band, the values are lower: below 10 μV low voltage, 10-25 μV middle voltage, and above 25 μV high voltage EEG.

Beta activity is typical during wakefulness. Alpha occurs in relaxed state with eyes closed. Theta waves are dominant in normal wake state in children; in adult people theta activity appears only in small amount especially in drowsiness. Delta waves are present in deep sleep; in healthy people do not exist in wake state. Sleep spindles are rhythmic activity in 12-14Hz frequency range and amplitude below 50 μV. The power spectra for the original (solid line) and the surrogate (dotted line) data are shown in **Figure 8**. Three peaks around 1-14Hz can be seen, indicating the presence of synchronized activities at these frequencies. According to the traditional classification first peak belongs to the delta band (1-4Hz) and the second peak belongs to the alpha band (8-12Hz) and third peak belongs to the beta band (>12Hz). Past research has examined whether such oscillatory neural activities self-couple and couple each other in a nonlinear fashion [17]. We study this issue with the new surrogate test method.

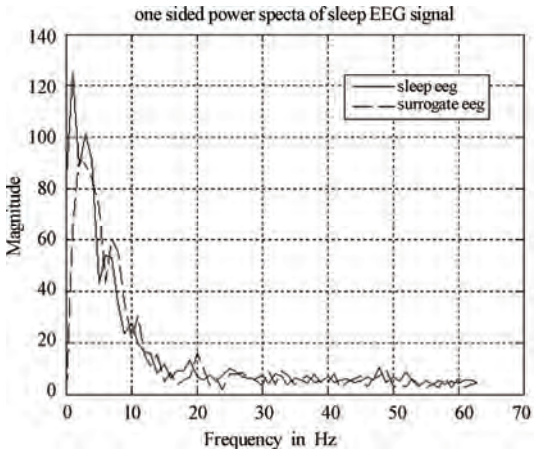

Figure 8. One sided power spectra estimated recording from P3O1 electrode on 1s period. The solid line is for the original data and dotted line is for surrogate data.

Table 3 provides comparison between E. Olbrich *et al.* and our study. However, a few spindles are not detected by the algorithm with the chosen parameters, i.e. the maximum of r_k remains smaller than the threshold r_b. Therefore, in our method proposed is using a surrogate data approach needs to be further optimized for more sensitive spindle detection.

5. DISCUSSION AND SUMMARY

In this study sleep spindles were detected in 1s overlapped segments, wide 0.5-16Hz band containing delta and theta was used for better eye movement separation. Alpha activity was excluded as it would increase auto covariance. With consensus scoring we would expect the agreement to improve [5]. The cost benefit of this laborious task would have been low. There was no manual artifact handling and it is possible that some misclassifications are the results of the artifacts undetected by the corresponding threshold r_k and were generated surrogate data with ziggurat method. In this algorithm there are two different thresholds but as it can be seen from **Table 3**, the amplitude criterion was most important (i.e. mostly amplitude in REM sleep is less than 50 μV and NREM sleep is greater than 100 μV). Schwilden *et al.* [14] reported that 90% of the EEG did not show any nonlinearity. They suggested that only under some pathological conditions, such as epilepsy, the brain signals manifest nonlinear effects. Other studies [15,16], have shown that non linear characteristics exist between theta and gamma EEG signals during short term memory processing. To settle these debates, one needs carefully constructed statistical tests. The method proposed here represents our effort in this direction. We will contrast our method with other often applied techniques in this area.

5.1. Comparison with other Surrogate Data Method

Multiple ways are currently in use to generate surrogate data sets to test the significance of the sleep spindle detection. In one method, the Fourier Transform (FT) is estimated for each segment and the phase of the Fourier Transform is randomized without changing the Fourier amplitude. The result is then inverse Fourier Transformed to generate a surrogate time series [14,17]. While the phase randomization destroyed nonlinearity and leads to linear Gaussian process [18], the Fourier amplitudes are random variables for a stationary process as well. By keeping them constant, one loses an important degree of freedom [12]. In contrast, our method, in which both amplitudes and phases of the Fourier Transform are randomly generated, produces surrogate data sets that are explicitly Gaussian, linear and share the same second order statistics with the original data. Another method, called amplitude adjusted Fourier Transform (AAFT), has been used in recent studies [19]. AAFT was designed to test the null hypothesis that the observed time series is a monotonic nonlinear transformation of a linear Gaussian process. This method has the same problems as the previous phase randomization method. In addition, the generated surrogate data sets usually do not have the same power spectrum as the original data, leading to false rejections when the discriminating statistics are sensitive to second-order statistical properties [20].

5.2. Final Remarks

We make several additional remarks regarding our method. First, generating the null hypothesis distribution for the test statistic is a very time-consuming process. The application of the extreme value theory mitigates this problem. Our examples show that the probability distribution function based on the extreme value theory fits the empirical distribution well. In agrees with that from the empirical histogram. Secondly, when the original data with length L need to be zero padded to length N (N > L), the surrogate data we generated have length N. To make sure that the surrogate data still have the same power spectra with the original data, the surrogate data need to be normalized by L, instead of the real data length N. Third, the periodogram method is used to estimate the power spectra. Consequently, all of the limitations associated with the periodogram method were inherent in our method, including poor frequency resolution for short data, fourth when we generated surrogate data set using ziggurat method does not generate random numbers effectively in tail regions because Matlab does not execute greater than 500 function calls [11]. Finally,

Table 3. Comparison between AR model and AR model with surrogate data approach.

S. No.	Name of the Electrode	AR-Model (E. Olbrich *et al.* 2003)		This study	
		Bandwidth (Hz)	Amplitude (μV)	**Bandwidth (Hz)**	**Amplitude (μV)**
1	C3A2	9-15	≈32	**10-16**	**≈27**
2	C4P4	11-15	25-42	**12-14**	**22-46**
3	F3C3	Relaxatory pole in the AR model (zero frequency)	---------	**11-16**	**≈118**
4	P3O1	Relaxatory pole in the AR model (zero frequency)	----------	**10.5-15**	**≈36**
5	P4O2	10-16	<15	**12-15**	**<10**

the discrimination power of our statistical test is unclear. This can be determined empirically by repeating the test many times on different realization for the data [20]. We will consider this issue as part of our future research.

In summary, detection of sleep spindles using the surrogate method proposed in this paper is shown to give accurate results when applied to test the significance of power spectral amplitudes. It is based on solid statistical principles and overcomes some weaknesses in previous methods for the same purpose. It is expected to become a useful addition to the repertoire of nonlinear analysis methods for neuroscience and other biomedical signal processing applications.

6. ACKNOWLEDGEMENTS

The authors wish to express their kind thanks to Ms. Kristina Susmakova for providing EEG sleep data and invaluable help and discussions.

REFERENCES

[1] Buzsaki, G., (2006) Rhythms of the brain, Oxford, U. K: Oxford University Press.

[2] Chen, Y. H., Bressler, S. L., Knuth, K. H., Truccolo, W. A., and Ding, M. Z., (2006) Stochastic modeling of neurobiological time series: Power, coherence, granger causality, and separation of evoked response from ongoing activity, Chaos, **16**.

[3] Barlow, J. S., (1979) Computerized clinical electroencephalography in perspective, IEEE Transactions Biomed. Eng., **26 (7)**, 377–391..

[4] Franaszczuk, P. J. and Blinowska, K. J., (1985) Linear model of brain electric activity EEG as a superposition of damped oscillatory models, Biol. Cybern., **53**, 19–25.

[5] Olbrich, E. and Achermann, P., (2003) Oscillatory events in the human sleep EEG detection and properties, Elsevier Science March., 1–6.

[6] Olbrich, E., Achermann, P., and Meier, P. F., (2002) Dynamics of human sleep EEG, Neuro computing CNS.

[7] Theiler, J., Eubank, S., Longtin, A., Galdrikian, B., and Farmer, J. D., (1992) Testing for linearity in time series: The method of surrogate data, Phys. D., **58**, 77–94,.

[8] Wang, X., Chen, Y. H., and Ding, M. Z., (2007) Testing for statistical significance in Bispectra: A surrogate data approach and application to neuroscience, IEEE Transactions on Biomedical Engineering, **54(11)**, 1974–1982.

[9] Wu, W. B., (2005) Fourier transform of stationary processes, Proc. Amer. Math. Soc., **133**, 285–293.

[10] Bendat, J. and Persol, A., (1986) Random data analysis and measurement procedures, 2nd ed. New York: Wiley.

[11] Marsagli, G. and Tsang, W. W., (2000) The ziggurat method for generating random variables, J. Stat. Softw., **5**, 1–6.

[12] Timmer J., "On Surrogate data testing for linearity based on the periodogram", eprints arxiv: comp-gas/9509003, 1995.

[13] Evans, M., Hastings, N., and Peacock, B., (1993) Statistical distributions, 2nd ed, New York: Wiley.

[14] Schwilden, H. and Jeleazcov, C., (2002) Does the EEG during isoflurane/alfentanil anesthesia differ from linear random data, J. Clin. Monit, Comput., **17**, 449–457.

[15] Schack, B., Vath, N., Petsche, H., Geissler, H. G., and Moller E., (2002) Phase coupling of theta-gamma EEG rhythms during short term memory processing, Int. J. Psychophys., **44**, 143–163,.

[16] Shils, J. L., Litt, M., Skolnick, B. E., and Stecker, M. M., (1996) Bispectral analysis of visual interactions in humans, Electroencephalography Clinical Neurophys., **l98**, 113–125.

[17] Schanze, T. and Eckhorn, R., (1997) Phase correlation among rhythms present at different frequencies: Spectral methods, application to microelectrode recording from visual cortex and functional implications, Int. J. Psychophyus., **26**, 171–189.

[18] Venema, V., Bachenr, S., Rust, H. W., and Simmer, C., Statistical characteristics of surrogate data based on geophysical measurements, Non linear Processes Geophys., **13**, 449–466.

[19] Chon, K. H., Raghavan, R., Chen, Y. M., Raghavan, D. J., and Yip, K. P, (2005) Interactions of TGF-dependent and myogeneic oscillations in tubular pressure, Amer. J. Physiol., **288**, F298–FF307.

[20] Schreiber, T. and Schmitz, A., (1997) Discrimination power of measures for nonlinearity in a time series, Phys, Rev. E, **55**, 5443–5447.

J. Biomedical Science and Engineering, 2009, 2, 304-311 **JBiSE**
10.4236/jbise.2009.25045 Published Online September 2009 (http://www.SciRP.org/journal/jbise/).

Fine-scale evolutionary genetic insights into *Anopheles gambiae* X-chromosome

Hemlata Srivastava[1], Jyotsana Dixit[1], Aditya P. Dash[2], Aparup Das[2]

[1]Evolutionary Genomics and Bioinformatics Laboratory, National Institute of Malaria Research, Sector 8, Dwarka, New Delhi-110 077, India. [2]Present address: World Health Organization, Southeast Asian Regional Office, New Delhi, India. [1]Equal contributions. Email: aparup@mrcindia.org

Received 28 April 2009; revised 10 May 2009; accepted 15 May 2009.

ABSTRACT

Understanding the genetic architecture of individual taxa of medical importance is the first step for designing disease preventive strategies. To understand the genetic details and evolutionary perspective of the model malaria vector, *Anopheles gambiae* and to use the information in other species of local importance, we scanned the published X-chromosome sequence for detail characterization and obtain evolutionary status of different genes. The telocentric X-chromosome contains 106 genes of known functions and 982 novel genes. Majorities of both the known and novel genes are with introns. The known genes are strictly biased towards less number of introns; about half of the total known genes have only one or two introns. The extreme sized (either long or short) genes were found to be most prevalent (58% short and 23% large). Statistically significant positive correlations between gene length and intron length as well as with intron number and intron length were obtained signifying the role of introns in contributing to the overall size of the known genes of X-chromosome in *An. gambiae*. We compared each individual gene of *An. gambiae* with 33 other taxa having whole genome sequence information. In general, the mosquito *Aedes aegypti* was found to be genetically closest and the yeast *Saccharomyces cerevisiae* as most distant taxa to *An. gambiae*. Further, only about a quarter of the known genes of X-chromosome were unique to *An. gambiae* and majorities have orthologs in different taxa. A phylogenetic tree was constructed based on a single gene found to be highly orthologous across all the 34 taxa. Evolutionary relationships among 13 different taxa were inferred which corroborate the previous and present findings on genetic relationships across various taxa.

Keywords: *Anopheles gambiae*; Comparative Genomics; Evolution; Malaria; Orthologous Genes; X-chromosome

1. INTRODUCTION

Determination of genetic architecture of different taxa in a vector borne disease model, helps not only in understanding the genetic pattern of host-parasite-vector interaction but also adds in devising methods for control measures. Further, characterization of different genes in the entire chromosome leads to identification of novel genes of essential functions and evolutionary process that governs these genes in populations. These determinations of genetic architecture should start with deep understanding and evolutionary inference of each individual gene of known function at the chromosomal level. The detail knowledge on the relative size of the genes [1], differential compositions of coding and non-coding elements in each gene [2] and contribution of non-coding DNA to the average length of the gene [3] could easily be evaluated with such kind of studies. This is further important when scanning is performed on chromosome-to-chromosome basis, so that differential genetic composition in each chromosome of a species can be compared [4]. Further, comparing genes among different taxa exploits both similarities and differences of different organisms to infer how Darwinian natural selection might have acted upon on these elements in the course of evolution. Considering the genomes as “bags of genes” and measuring the fraction of orthologs shared between genomes could provide vital information on the evolutionary history of the genes [5]. Also, if any particular gene is found to be conserved in many organisms, reconstruction of phylogeny among these organisms is possible. However, such kinds of studies are possible only when adequate genome information is at hand. Fortunately, many organisms have been fully sequenced in recent years providing opportunities to fine-scale understanding of the genetic architecture of species of medical and agricultural importance and comparison across species and taxa [6].

To this respect, malaria is a devastating disease with global cases of about 300 to 500 million infections per year and deaths of about one and half millions [7]. Global efforts to eradicate malaria failed immaturely and scientist and policy makers are now focusing on the control of this disease. However, emergence and spread of drug-resistant parasites and insecticide-resistant vectors have seriously hampered the efforts and put new challenges to tackle with the situation [8]. This situation invites a close and deep genetic understanding of both parasites and vectors and devise new methods for malaria control.

The whole genome sequence information of the mosquito *Anopheles gambiae* [9], the principal vector of malaria in Africa is available in the public domain. However, the vector species are not all the same across different malaria endemic zones in the globe as different other species of the genus *Anopheles* are of local importance. Since controlling the malaria vector is one of the finest strategies to control malaria, understanding the genetic composition of different endemic *Anopheles* species in different localities is the need of the hour for development of effective malaria control strategies. Keeping in view that the whole genome sequence information is only available for one of the malaria vector *An. gambiae*, utilization of such information might lead to understanding the genetics of vector potentiality, insecticide resistance, etc. and extend the information to other species of local and focal importance. In addition, due to lack of genome information in other *Anopheles* species, the information from *An. gambiae* could be utilized in designing genetic markers for evolutionary studies in genes and populations of vectors in the malaria endemic zones of the globe.

We herewith utilize the whole genome sequence information of *An. gambiae* to characterize the whole X-chromosome for different gene compositions and fine-scale study of each individual genes of known function. We performed homology searches of each of the known genes of *An. gambiae* X-chromosome in 33 taxa with published whole genome sequences and also constructed phylogenetic tree. The results not only provide detail understanding on differential compositions of genetic elements in *An. gambiae* X-chromosome, but also would help in developing genetic markers to study genetic diversity and population histories of other species of *Anopheles* of local importance.

2. MATERIAL AND METHODS

The *An. gambiae* genome comprises of 3 pairs of chromosomes, 2 pairs of autosomes and a pair of sex chromosome. Whole genome sequence information is available at the public domain for the pest strain of *An. gambiae* [9]. We used the Ensemble web database (www.ensembl.org) from release 45-June 2007, to retrieve genetic information on the telocentric X- chromosome. We started our scanning for different genes from one end of the X-chromosome and proceeded till we reached the end. We looked for genes that have known functions (known genes) and also genes that are completely new (novel genes) following the classifications provided at the Ensemble database. Due to functional importance, we deeply characterized only the known genes leaving apart the novel genes. For the convenience of further analysis, we classified the known genes based on length of nucleotide bases as, Class 1 (0 to 1 kb); Class 2 (1-2 kb); Class 3 (2-3 kb); Class 4 (3-4 kb); Class 5 (4-5 kb) and Class 6 (above 5 kb). The composition of different genes in the *An. gambiae* X- chromosome was determined as per information in the Ensemble web database. Further, information on 33 other taxa with whole genome sequence information was also available at the Ensemble web database. We utilized this information to infer X-chromosome genes of *An. gambiae* having orthologs (orthologs are genes derived from single ancestral gene in last common ancestor of compared species) and paralogs (paralogous genes develop by gene duplication in the similar lineage) across 33 different taxa. The genes of *An. gambiae* with no ortholog or paralog were considered to be unique genes to this species. Three criteria were followed to define the candidate orthologous genes suggested by [8] in the Ensemble web database. First, the sequences of genes should have highest level of pair-wise identity when compared with genes in the other genome. Second, pair-wise identity should be significant (E, the expected fraction of false positives should be smaller than 0.01) and third, the similarity extends to at least 60% of one of the gene. We followed similar procedures to classify the orthologous genes in *An. gambiae* X-chromosome. Out of the many orthologs found, one particular gene was found to be present in all the 34 different taxa (included *An. gambiae*) presently studied. We constructed an un-rooted neighbor-joining (NJ) tree to infer the evolutionary status of different taxa at this conserved gene (AGAP001043). However, due to high sequence dissimilarity, only 13 taxa could be utilized for a meaningful phylogenetic tree construction. Length of each branch and bootstrapped values for each internal node were also estimated using VEGA ZZ software downloaded from internet (http://www.ddl.unimi.it/vega/index.htm). For all statistical analyses, the free version of 'analyze-it' a Microsoft Excel add-in was used.

3. RESULTS

Scanning of the whole X chromosome of *An. gambiae* revealed the presence of 1088 genes, out of which 982 were novel and 106 were genes of known functions. Due to functional relevance, the known genes were further analyzed. These genes were classified based on size (see materials and methods). Out of the 106 known genes,

most (62 genes, 58%) were small and thus fall under Classes 1 and 2. Thus, majority of the known genes in *An. gambiae* X-chromosome are small in size (**Figure 1**). Only 18% of the total known genes falls under Classes 3, 4, and 5, whereas 23% comes under Class 6 (more than 5 kb). Thus, the distribution of known genes in *An. gambiae* seems to be quite uneven, as small and large sized genes constitute 81% of the total known genes in the *An. gambiae* X-chromosome (**Figure 1**).

Since genes in the eukaryote genome are often found to bear introns (non-coding part of the gene, flanked on each side by the coding parts) and considering *An. gambiae* as a higher eukaryote, we determined the distribution of exons (coding part of the gene) and introns of each known gene (**Figure 2**). The distribution of genes with different number of introns is shown in **Figure 2**. It is interesting to note that almost two-third of the known genes (79 genes, 74.52%) have either no or very less number (maximum of three) of introns. Genes having more than three introns contribute to only 17% of the total known genes of X-chromosome of *An. gambiae*. Further, we looked for size of each intron and exon in each gene and calculated the average intron and exon length and their ratio (**Figure 3**). The average ratio of exon to intron was higher in genes with less number of introns (**Figure 3**), as compared to genes with more number of introns. Thus, it seems that the average length of introns in a gene increases with the increase in number of introns. In order to test this hypothesis, we calculated Pearson's correlation coefficient (r) which was found to be positive and highly statistically significant (r=0.99, P<0.0001). Moreover, in order to test the hypothesis if the accumulation of introns has considerably contributed in increasing the length of the gene in general, we calculated r value between intron length and gene length which was found to be positive and highly statistically significant (r=0.49, P<0.0001) as well. Thus, it is clear that introns play a major role in the overall length of genes in the X-chromosome of *An. gambiae*.

As many as 86 known genes out of 106 total known genes of *An. gambiae* X-chromosome were found to have homologs (both orthologs and paralogs) across 33 different taxa. Out of these 86 genes, 41 have only orthologs, 3 have only paralogs and 42 have both orthologs and paralogs. No homologs could be detected in the rest 20 genes, thus are considered unique to *An. gambiae* (**Figure 4**). Thus, in total, 83 (41+42) have orthologs and 45 (3+42) have paralogs in the X-chromosome known genes of *An. gambiae*. However, the distribution of orthologs varies across 33 different taxa; *Aedes aegypti* seems to bear most of the *An. gambiae* homologs (78 out of 83 orthologs) and the yeast *S. cerevisiae* bears the least (6 out of 83 orthologs) (**Figure 5**). These are at the highest and lowest ends of the homology prediction of 83 X-chromosome genes of *An. gambiae*.

Since majority of the known genes of X-chromosome of *An. gambiae* are either short or large in size (**Figure 1**), we were interested to know the distribution pattern of different types of genes based on homology predictions (orthologous, paralogous and unique) in different classes based on size (**Figure 1**). The details of such distribution are shown in **Figure 6**, which seems to be random. Whereas the orthologous genes are slightly abundant in Classes 2 and 6, the paralogous genes show a clear pattern of decreasing abundance from Class 1 to Class 6. In contrast unique genes are found to be much prevalent in Class 2 and least in Class 6 (**Figure 6**). We further looked at the distribution of these three types of genes (orthologous, paralogous and unique) based on the number of introns they posses (**Figure 7**) and found that

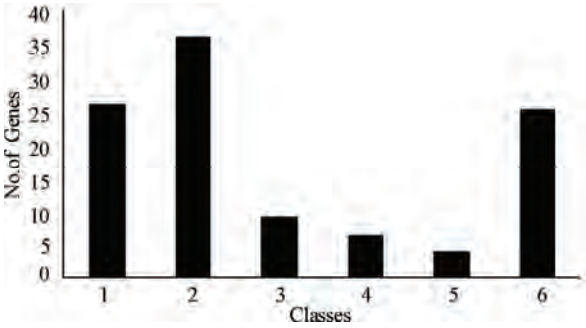

Figure 1. Classification of known genes of *An. gambiae* X-chromosome based on size (nucleotide base pair).

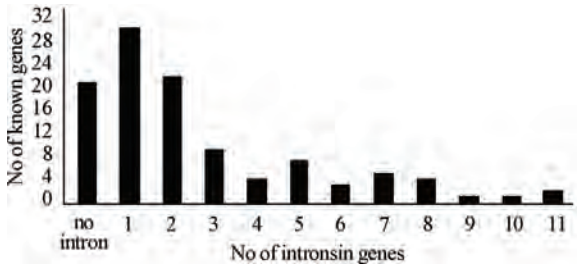

Figure 2. Distribution of *An. gambiae* X-chromosome known genes according to the number of introns.

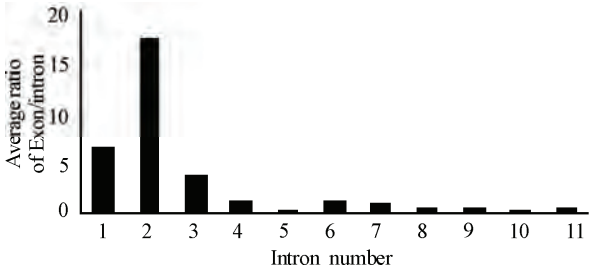

Figure 3. Average exon to intron ratio of *An. gambiae* X-chromosome known genes.

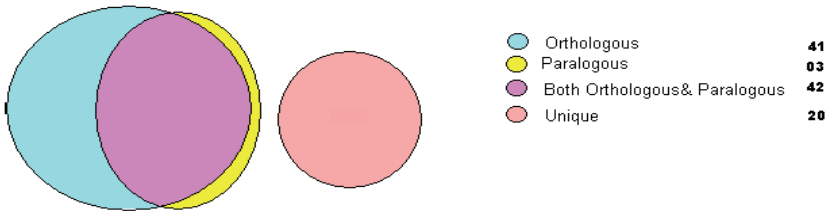

Figure 4. Distribution of different gene types (based on homology prediction) in X-chromosome of *An. gambiae.*

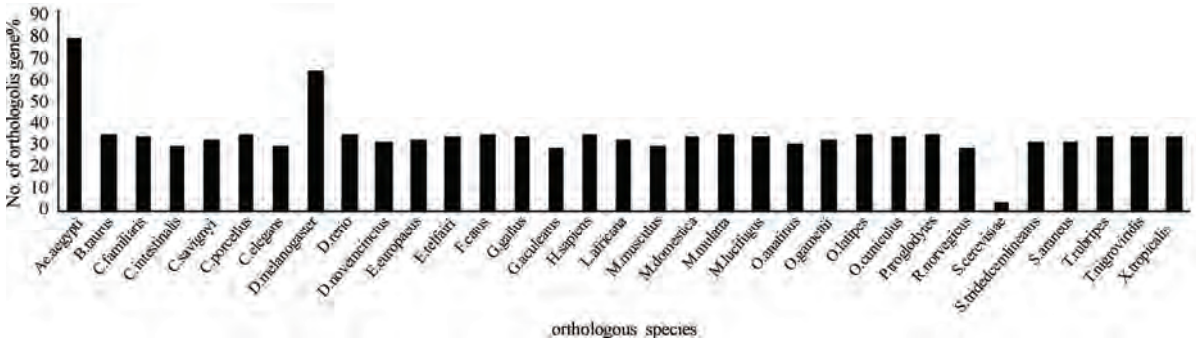

Figure 5. Distribution of different taxa showing number of shared genes with *An. gambiae*.

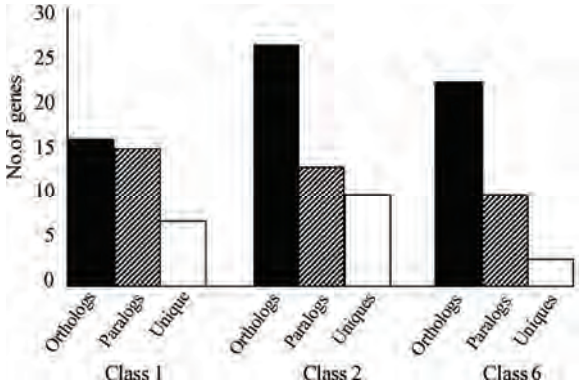

Figure 6. Distribution of orthologous, paralogous and unique genes of *An. gambiae* X-chromosome across different classes as in **Figure 1**.

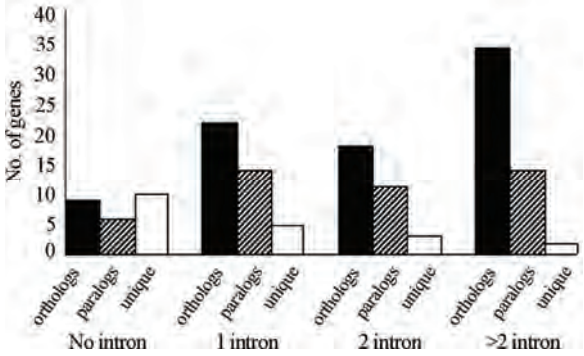

Figure 7. Distribution of orthologous, paralogous and unique genes of *An. gambiae* X-chromosome based on intron number.

most of the orthologous genes are biased towards more number of introns (>2) and majority of unique genes are without introns. There seem to be no biasness on the distribution of paralogous genes based on the number of introns, although a comparatively less number of paralogous genes were found to be without introns. In contrast, most of the unique genes are found to be without intron and the number decreases with increase in the number of introns. However, no significant correlation was found to exist between these two variables (r=-0.04, P=0.88).

In the process of homology prediction, we found a single gene (AGAP001043) of *An. gambiae* having orthologs in all other 33 taxa. This situation provided us an opportunity to look for evolutionary history, based on this conserved gene across all the 34 taxa. For this we constructed un-rooted neighbor joining (NJ) tree with only the coding sequences (exons) considering all 34 taxa, but due to lots of non-homologous sequences, no proper alignment among sequences could be obtained. Thus we went on deleting taxa with more number of non-homologous stretches and ended-up with only 13 taxa where meaningful alignment and construction of a phylogenetic tree was possible (**Figure 8**). Length of each branch leading to taxa was calculated as also the strength of each internal node through estimation of bootstrapped trees (**Figure 8**). Although in most cases, known closely related species came together in a single clade, (*e.g. Aedes aegypti*, *An. gambiae* and *Drosophila melanogaster*), the separation of human and chimpanzee branch is somehow an interesting observation (**Figure 8**). The strength of

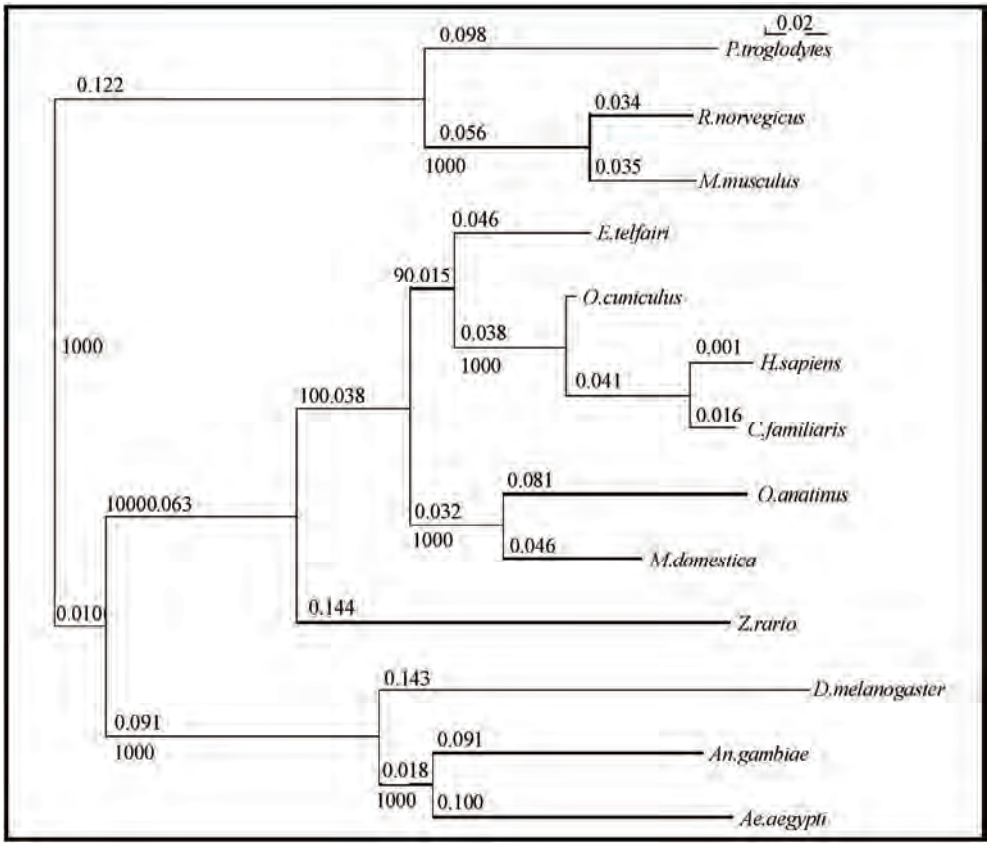

Figure 8. Phylogenetic tree with bootstrap values (in bold font) and branch length (in normal font) in13 different taxa.

each internal node was found to be absolute in all the cases, signifying the phylogenetic tree is robust enough to be considered significant.

4. DISCUSSION

Although about two third part of the world is colonized by different species of mosquitoes and various species of the genus *Anopheles* is of great abundance, whole genome sequence information from only a single species, *An. gambiae* is so far available at the public domain. This situation possesses great constraint on researchers working on species of non-African importance. The preliminary objective of this study is to understand genomic architecture of *An. gambiae* through fine-scale dissection of the X-chromosome and utilize the information in developing nuclear DNA markers for estimating genetic diversity to infer both population demography and natural selection in species of importance in non-African malaria vectors. To start with, we have studied the X-chromosome, since it has several advantages over the autosomes. For example, X-chromosome is known to bear a rich resource of easily accessible genetic data, and provides a unique tool for population genetic studies [10]. Further, majority of population genomic studies have been undertaken on the model organism, *Drosophila* utilizing X-linked genes [11,13].

We have considered genes of known function for detail characterization and analyses as they are the store house of important identifiable characters. More than a half of the known genes in *An. gambiae* X-chromosome are of short length and about 40% of the total known genes are engaged in housekeeping functions. Housekeeping genes are known to be often compact in size, which is attributed to selection for economy in transcription and translation [14,15]. Although a direct correlation between the function and size of the genes was not found (data not shown), abundance of shorter genes in *An. gambiae* might be due to the fact that most of the genes are engaged in housekeeping functions. However, long-sized genes (of more than 5kb length) were also abundant to certain extent (20%) in this chromosome. In contrast, genes of intermediate length (2kb to 5kb) were very less in occurrence. As far our knowledge goes, no study has reported this trend in the distribution of variable gene length across a single chromosome in any organism.

Majority of genes in *An. gambiae* X-chromosome shows a clear tendency of having either no or a very few (about three) introns (**Figure 2**). It has been suggested

that intronless gene families can evolve rapidly either by gene duplication or by reverse transcription/integration [16]. In *Oryza* and *Arabidopsis*, intronless genes have no homology and perform species-specific functions that are unique in respective species [17]. Thus, the findings of biasness towards either no or a few introns in majority of genes of known functions point towards the role of natural selection in reducing the size or presence of introns, thus reducing the overall transcriptional cost for effective expression. Findings of genes with very few numbers of introns in eukaryotic genome in general [18], further corroborate our contention.

The present study revealed the presence of only four genes with an appreciably high number of introns (9-11). Three of these four genes belong to nicotinic acetylcholine receptor gene families [19] which are the known targets of insecticides, neonicotinoids [20], as well as naturally derived spinisyns [21]. The presence of such high number of introns in these genes shows that they require more variability in their protein products and more number of introns make these genes more versatile in their expression by increasing the chances of alternative splicing and less 5′splice site biasness [22]. These genes are of much importance as far as growing insecticide resistance in almost all species of malaria vectors is concerned. Understanding of molecular mechanisms of resistance and molecular evolutionary studies should be targeted towards these genes for better understanding on evolution of insecticide resistance in malaria vectors.

We found strong positive correlations between gene length and intron length and intron length and intron number, which clearly suggests that size of the X-chromosome known genes in *An. gambiae*, is somehow dependent on accumulation of introns. These findings are in complete agreement with the general pattern observed in eukaryotic genome, where enlargement of genome size and decrease in genome compactness with increase in number and size of introns was supposed to be a general pattern during evolution of eukaryotes [5].

Based on evolutionary status, known genes in *An. gambiae* fall in all three categories (orthologous, paralogous and unique). Further, there is a clear distinction on the size, intron number and non-coding DNA content in different gene categories. Orthologous genes are comparatively larger in length and also contain more number of introns. These observations corroborate the fact that conserved or orthologous genes show more number of introns [23], possibly due to their slow evolution rate. Further, these types of genes tend to gain more and lose fewer introns [24]. In contrast to the characters of orthologous genes, no clear pattern was observed for the paralogous genes. This observation fits to the findings in the malaria parasite, *Plasmodium falciparum* and *P. yoelli yoelii*, where duplicate genes or paralogous genes in both the species exhibit a dramatic acceleration of intron gain/loss and protein evolution in comparison with orthologous genes, suggesting increased directional and/or relaxed selection in duplicate genes [25]. In contrast, the unique genes are mostly intron-less and might be evolving at a faster rate loosing the non-coding portions; hence homologs of these genes are no more recognizable [26].

We detected a close genetic affinity at the X-chromosome known genes among three taxa of insects; *An. gambiae*, *Ae. aegypti* and *D. melanogaster*. This is not surprising, as three of them belong to the similar order Diptera. Similar observations have been made in earlier studies [27] as also among *Drosophila* species with comparative genomic approaches [6]. Although *S. cerevisiae* was found to be farthest in homology, six genes of *S. cerevisiae* show homology to *An. gambiae* genes. The function of these genes was found to be tyrosyl-t RNA synthetase, peroxiredoxin dependent peroxidase and glutathione reductase, one was putative membrane bound O-acyltransferase. However, these genes possess very few introns. Although it is apparent that gene size has increased through accumulation of introns in higher taxa, it is surprising that these six genes remained conserved in the long evolutionary process from yeast to insects. It is probable that, these genes might be under some functional constraint and natural selection saved their compositions across different lineage.

We considered a gene present in all the 34 taxa to infer evolutionary history through phylogenetic tree construction. The pattern in the tree was mostly found to comply with general patterns of phylogenetic relationships among organisms. The placement of *An. gambiae*, *D. melanogaster* and *Ae. aegypti* in a single clade further corroborates our observation of close genetic relatedness among these three taxa (see above). However, it was surprising to note that human and chimpanzee are placed in two separate clades. Although, human and chimpanzee are genetically close to each other [28], gross differences at several genes have also been observed [29]. Included in these genes is a gene responsible for malaria susceptibility in humans and chimpanzee [30]. These two taxa differ in their susceptibility to malaria due to human specific loss of N-glycolylneuraminic acid, which is present in primates. It might then be true that genomic difference between two species only can be traceable at selected genes and the presently studied gene is one of them. This gene codes for a protein which is involved in signal transduction process and participates in transmission of developmental information by associating with alpha or beta catenin. Whereas basic function of this gene is conserved, little functional differences exist across almost all taxa. Further in depth study revealed that however, the gene function is conserved in taxa falling in a particular clade found here, whereas few differences were observed across clades in the phylogenetic tree (**Figure 8**). Thus, functional con-

servation of this gene is exactly overlaps with the position of taxa in the phylogenetic tree.

In conclusion, the present study not only provides fine-scale views to the genetic architecture of the X-chromosome of the model malaria vector of African importance, but also reveals several interesting features on evolutionary insights into genes and taxa of different taxonomic status. The information is of great importance, especially to the population geneticists, to understand genetic diversity and infer the respective roles of demography and natural selection in evolution of genes in different *Anopheles* species populations of local importance.

5. ACKNOWLEDGEMENTS

Extramural funding from the Indian Council of Medical Research (ICMR), New Delhi in the form of an Ad-hoc research grant to AD is thankfully acknowledged. We thank Dr. Neena Valecha for her kind support to HS during the initial phase of the study. Lily Basu, Deepshikha Lal, Garima Goyal and Suchita Singh helped in organizing the initial work elements.

REFERENCES

[1] Hahn, M. W., Han, M. V., and Han, S. G., (2007) Gene family evolution across 12 Drosophila genome, Public Library of Science Genetics, **3,** 1–12.

[2] Matthee, C. A., Eick, G., Willows, M. S., Montgelard, C., Pardini, A. T., and Robinson, T. J., (2007) Indel evolution of mammalian introns and the utility of non coding nuclear markers in eutherian phylogenetics, Molecular Phylogenetics and Evolution, **42**, 827–837.

[3] Cardazzo, B., Bargelloni, L., Toffolatti, L., and Patarnello, T., (2003) Intervening sequences in paralogous genes: A comparative genomic approach to study the evolution of X chromosome introns, Molecular Biology and Evolution, **20,** 2034–2041.

[4] Gazave, E., Bonet, T. M., Fernando, O., Charlesworth, B., and Navarro, A., (2007) Patterns and rates of intron divergence between humans and chimpanzees, Genome Biology, **8,** 1–13.

[5] Huynen, M. A. and Bork, P., (1998) Measuring genome evolution, Proceedings of National Academy of Sciences USA, **95,** 5849–5856.

[6] Clark, A. G., Eisen, B. M., Smith, D. R., Bergman, C. M., Oliver, B., Markow, T. A., *et al*., (2007) Evolution of genes and genomes on the Drosophila phylogeny, Nature, **450,** 203–218.

[7] WHO. (2005) World malaria report. http://www.rbm.who.int/wmr.

[8] Zakeri, S., Afsharpad, M., Raeisi, A., and Djadid, N. D., (2007) Prevalence of mutations associated with antimalarial drugs in Plasmodium falciparum isolates prior to the introduction of sulphadoxine-pyrimethamine as first-line treatment in Iran, Malaria Journal, **6,** 1–2.

[9] Holt, R. A., Subramanian, G. M., Helpern, A., Sutton, G. G., Charlab, R., Nusskern, D. R., *et al*., (2002) The genome sequence of the malaria mosquito Anopheles gambiae, Science, **298,** 129–149.

[10] Stephen, S. F., (2004) The X chromosome in population genetics, Nature Reviews Genetics, **5,** 43–51.

[11] Vogl, C., Das, A., Beaumont, M., Mohanty, S., and Stephan, W., (2003) Population subdivision and molecular sequence variation: Theory and and analysis of Drosophila ananassae data, Genetics, **165,** 1385–1395.

[12] Bains, J. F., Das, A., Mousset, S., and Stephan, W., (2004) The role of natural selection in genetic differentiation of worldwide populations of Drosophila ananassae, Genetics, **168**, 1987–1998.

[13] Das, A., Mohanty, S., and Stephan, W., (2004) Inferring the population structure and demography of Drosophila ananassae from multilocus data, Genetics, **168,** 1975–1985.

[14] Castillo-Davis, C. I., Mekhedov, S. L., Hartl, D. L., Koonin, E. V., and Kondrashov, F. A., **(**2002) Selection for short introns in highly expressed genes, Nature Genetics, **31,** 414–418.

[15] Vinogrado, A. E. (2004) Compactness of human housekeeping genes: Selection for economy or genomic design, Trends in Genetics, **20,** 248–253.

[16] Jain, M., Tyagi, A. K., and Khurana, J. P., (2006) Genome wide analysis, evolutionary expansion, and expression of early auxin-responsive SAUR gene family in rice (Oryza sativa), Genomics, **88**, 360–371.

[17] Jain, M., Khurana, P., Tyagi, A. K., and Khurana, J., (2007) Genome-wide analysis of intronless genes in rice and Arabidopsis, Functional & Integrative Genomics, In Press.

[18] Simpson, A. G. B., Macquarrie, E. K., Roger, A. J., (2002) Eukaryotic evolution: Early origin of canonical introns, Nature, **419**, 270.

[19] Jones, A. K., Grauso, M., and Sattelle, B. D., (2004) The nicotinic acetylcholine receptor gene family of the malaria mosquito, Anopheles gambiae, Genomics, **85**, 176–187.

[20] Matsuda, K., Buchigham, S. D., Kleier, D., Rauh, J. J., Grauso, M., and Sattelle, D. B., (2001) Neonicotinoids: Insecticides acting on insect nicotinic acetylcholine receptors, Trends in Pharmacological Sciences, **22**, 573–580.

[21] Bond, G. J., Marina, C. F., and Williams, T., (2004) The naturally derived insecticide spinosad is highly toxic to Aedes and Anopheles mosquito larvae, Medical and Veterinary Entomology, **18,** 50–56.

[22] Manuel, I., David, P., and Scott, W. R., (2007) Coevolution of genomic intron number and splice sites, Trends in Genetics, **23**, 321–325.

[23] Jordan, I. K., Marino-Ramirez, L., Wolf, Y. I., and Koonin, E. V., (2004) Conservation and co-evolution in the scale-free human gene co-expression network, Moleculer Biologyand Evolution, **21**, 2058–2070.

[24] Carmel L., Rogozin I. B., Wolf, Y. I., and Koonin, E. V., (2007) Evolutionarily conserved genes preferentially accumulate introns, Genome Research, **17,** 1045–1050.

[25] Castillo-Davis, C. I., Bedford, T. B. C., and Hartl, D. L., (2004) Accelerated rates of intron gain/loss and protein evolution in duplicate genes in human and mouse malaria parasite, Molecular Biology and Evolution, **21**, 1422–1427.

[26] Stirling, B., Yang, Z. K., Gunter, L. E., Tuskan, G. A., and Bradshaw, H. D., (2003) Comparative sequence

analysis between orthologous regions of the Arabidopsis and Populus genomes reveals substantial synteny and microcollinearity, Canadian Journal of Forest Research, **33**, 2245–2255.

[27] Bohbot, J., Pitts, R. J., Kwon, H. W., Rutzler, M., Robertson, H. M., and Zwiebel, L. J. (2007) Molecular characterization of Aedes aegypti odorant receptor gene family, Insect Molecular Biology, **16**, 525–537.

[28] Uddin, M., Wildman, D. E., Liu, G., Xu, W., Johnson, R. M., Hof, P. R., *et al*., (2004) Sister grouping of chimpanzees and humans as revealed by genome-wide phylogenetic analysis of brain gene expression analysis, Proceedings of National Academy of Sciences, **101**, 2957–2962.

[29] Gilad, Y., Man, O., and Glusman, G., (2005) A comparison of the human and chimpanzee olfactory receptor gene repertoires, Genome Research, **15**, 224–230.

[30] Martin, M. J., Rayner, J. C., Gagneux, P, Barnwell, J. W., and Varki, A., (2005) Evolution of human-chimpanzee differences in malaria susceptibility: Relationship to human genetic loss of N-glycolylneuraminic acid, Proceedings of National Academy of Sciences, **102**, 12819–12824.

J. Biomedical Science and Engineering, 2009, 2, 312-317 **JBiSE**
doi: 10.4236/jbise.2009.25046 Published Online September 2009 (http://www.SciRP.org/journal/jbise/).

Recent advances in fiber-optic DNA biosensors

Yi-Ming Wang[1,2*], Xiao-Feng Pang[1], Yu-Yu Zhang[2]

[1]College of Life Science and Technology, University of Electronic Science and Technology of China, Chengdu, China; [2]College of Material and Chemistry & Chemical Engineering, Chengdu University of Technology, Chengdu, China.
Email: wangyiming@cdut.cn

Received 1 December 2008; revised 13 May 2009; accepted 18 May 2009.

ABSTRACT

Fiber-optic DNA biosensors are a kind of analytic setups, which convert the Waston-Crick base pairs matching duplex or Hoogsteen's triplex (T/A-T, C/G-C) formation into a readable analytical signals when functionalized single-strands DNA (ssDNA) or double-strands DNA (dsDNA) of interest are immobilized on the surface of fiber-optic hybrids with target DNA or interacts with ligands. This review will provide the information about the fiber-optic DNA biosensors classified into two categories depending on the end fiber and side fiber with or without the labels—label-free fiber-optic DNA biosensors and labeled fiber-optic DNA biosensor in recent years. Both are dissertated, and emphasis is on the label-free fiber-optic DNA biosensors. Fiber-optic DNA biosensors had got great progresses because fiber-optic has more advantages over the other transducers and are easily processed by nanotechnology. So fiber-optic DNA biosensors have increasingly attracted more attention to research and develop the new fiber-optic DNA biosensors that integrated with the "nano-bio-info" technology for in vivo test, single molecular detection and on-line medical diagnosis. Finally, future prospects to the fiber-optic DNA biosensors are predicted.

Keywords: DNA Hybridization; Fiber-Optic Biosensors; Label-Free; Nanotechnology

1. INTRODUCTION

Fiber-optic DNA biosensors are a kind of analytic setups, which convert the Waston-Crick base pairs matching duplex or Hoogsteen's triplex (T/A-T or C/G-C) formation into a readable analytical signals when functionalized single-strands DNA (ssDNA) or double-strands DNA (dsDNA) [1,2] of interest are immobilized on the surface of side or end of fiber-optic hybrids with target DNA or interacts with ligands, for example pollutants [3] in the solution. This review will provide the information about the application and potential of fiber-optic DNA biosensors classified into two categories depending on the fiber with or without labels—label-free fiber-optic DNA biosensors and labeled fiber-optic DNA biosensor in recent years. With the development of nanotechnology, fiber-optic DNA biosensors have got great progresses because fiber-optic can be easily miniatured to the nanometer scale size by chemical etching [4] or tube etching [5] and mechanically pulled with CO_2 laser heating setup [6], they are immune to electromagnet [7], disposability [8] and long-distance transmission [9]. Because of these properties, fiber-optic DNA biosensors have increasingly attracted more attention to research and develop the new fiber-optic DNA biosensors that integrated with the "nano-bio-info" technology so that they can be employed for in vivo or within single cell test [10], especially in the intracellular measurement for real-time or on-line medical diagnosis [11,12]. On the basis of optical techniques that correlate changes in concentration, mass, number of molecules, or other properties to direct changes in the characteristics of light for detection of DNA hybridization or damage [13], different label-free fiber-optic DNA biosensors are depicted in details. Finally, future prospects to fiber-optic DNA biosensors are brought forward.

2. ADVANTAGES AND DISADVANTAGES OF FIBER-OPTIC DNA BIOSENSORS

Nanoparticles [14,15], nanotubes [16,17], nanowires [17,18,19,20,21,22,23] and fiber-optics as the matrices of DNA biosensors to detect DNA specific sequence and DNA hybridization have been reported. Fiber optic-based DNA biosensors have many advantages over other matrices-based DNA biosensors as following:

1) Fibers have a flexible geometry and can be tractably miniaturized at low cost to nanosacle structure for *in vivo* measurements.

2) Fibers are immune to electromagnet, lower temperature-dependence and low loss over long distance transmission [7,8,9].

3) Proper adjustment of the refractive index of the waveguide and the surrounding media enables the performance of surface-specific spectroscopy [25].

4) Fibers can guide light of different wavelengths at the same time and in the different directions, so more than one analyte can be responded simultaneously immobilized multiple DNA probe molecules on the fiber with a monitoring central unit.

5) Fibers have high Security and no reference electrode.

6) They are highly stable with respect to calibration, especially if one can measure the ratio of the intensities at two wavelengths [26].

However, some disadvantages could confine their applicability and were present [25,26].

1) They are subjected to ambient light interference, background absorbance, Raman scatter of fibers.

2) Limited stability of biological component immobilized onto a fiber surface and limited availability of optimized commercial accessories for use with fiber-optic.

3) Immobilized chemistries are subjected to problems with inadequate path length, path length instability due to matrix swelling, reagent photolability and reagent leaching.

4) They have a limited dynamic range in comparison to electronic sensors.

5) Existing techniques are difficult to directly characterize the functionalized surface of fiber because of small size.

3. LABELD FIBER-OPTIC DNA BIOSENSORS

Fluorescence labels were often used for biological research protocols. Fluorescence measurement is readily upscaled for multiplexing and can selectively associate with dsDNA. Advances in the fluorescence-labeled fiber-optic DNA biosensors-classified into two formats depending on the interaction between fluorescent agents and probe DNA sequence were introduced to detect DNA hybridization, concentration, damage and single base mismatch.

3.1. Fluorescent Reagents Intercalation into dsDNA for Detection of Hybridization

Intercalators, such as ethidiun bromide (EB), acridine orange (AO) and thiazole orange (TO), were selectively tethered into DNA hydrids by noncovalent bond in these DNA biosensors. Once these intercalators intercalated with dsDNA, it will yield an increase in the intensity of fluorescence by excitation (**Figure 1**).

Niu *et al.* [27] had designed a fluorescence fiber-optic DNA biosensor using p-Hydroxyphenylimidazo[f] 1, 10-phenanthroline Ferrum(III) ($[Fe(phen)_2 \cdot PHPIP]^{3+}$) as indicator to detect DNA hybridization. In this experiment, 16*B (biotin-5′-CAC AAT TCC ACA CAA C-3′ S_1) as capture probe was immobilized on the fiber-optic, and hybridized with the different concentrations complementary strand 16*C (5′-GTT GTG TGG AAT TGT G-3′ S_2). After hybridization, fiber-optic obtained was washed with doubly distilled water to remove oligonucleotide bound nonspecifically. In order to detect nonspecific binding, a noncomplementary, 20-mer oligonucleotide 20*N (5′-CTG CAA CAC CTG ACA AAC CT-3′ S_3) was used. Then the DNA-modified optical fiber was immersed in $[Fe(phen)_2 \cdot PHPIP]^{3+}$ aqueous solution, and subsequently subjected to fluorescence spectroscopy studies. The result showed that there was no response at S_1/fiber-optic and S_1–S_3/fiber-optic to testify the selective hybridization and not absorption of the target ssDNA on the fiber-optic (**Figure 2** curve a and b). While the enhancement of fluorescence indicated that $Fe(phen)_2 \cdot PHPIP]^{3+}$ molecules were reconcentrated on the S_1–S_2/fiber-optic surface for the binding interaction (**Figure 2** curve c-g).

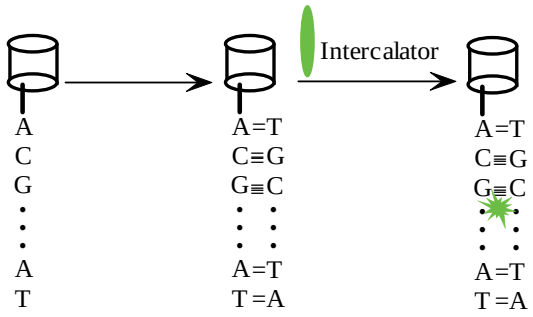

Figure 1. Scheme of intercalators as fluorescent labels tethered into dsDNA immobilization on the exposed core of fiber-optic for detection of DNA hybridization.

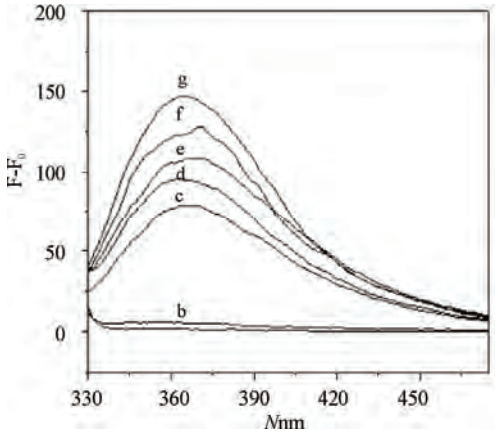

Figure 2. Fluorescent intensity of Fe $(phen)_2 \cdot PHPIP \cdot 3ClO_4 \cdot 2H_2O$ on (a) S_1/ fiber-optic; (b) S_1–S_3/ fiber-optic; and (c-g) S_1-S_2/ fiber-optic. C_{PBS} (pH 6.0): 0.20 M, $C_{[Fe(phen)_2PHPIP]^{3+}}$: 8.0×10^{-6}M, (c) Cs_2: 1.98×10^{-6} M; (d) Cs_2: 2.96×10^{-6} M; (e) Cs_2: 3.92×10^{-6} M; (f) Cs_2: 4.89×10^{-6}M; (g) Cs_2: 58.25×10^{-6}M [27].

Piunno *et al.* [28] had established a fluorescence fiber-optic DNA sensor system to detect the DNA hybridization using EB as an intercalation. In order to test the reproducibility of the sensor, another same DNA sample was determined by same experimental condition, and the fluorescence intensity was again measured. The results indicated that an increase in fluorescence intensity was observed which was similar in magnitude to that observed from the first dsDNA analysis. It demonstrated that the detection system was shown to be reproducible.

In addition, many experiments [29,30,31,32] had been performed by Svanvik research group using intercalators for the detection of DNA hybrid. Piunno *et al.* [33] had investigated a fiber-optic biosensor for detection of DNA hybridization using fluorescent DNA stain ethidium bromide. These biosensors didn't require traditional labeling step prior to analysis of a sample [34], but they are influenced to ambient temperature and solution ionic strength.

3.2. Fluorescent Agents Covalently Bind to ssDNA for Detection of DNA Hybridization

The detection of DNA hybrid was performed using fluorescent agents immobilized on the ssDNA through the format of covalent bond. The fluorescent enhancement or quenching was occurred when the complementary DNA was associated with the probe sequence (**Figure 3**).

Wang and Krull [35,36,37] had investigated thiazole orange dyes were covalently linked to the 5'- end of the oligonucleotides, providing for a self-contained labeling strategy for detection of hybrids. The biosensors provided changes in steady-state fluorescence intensity signals upon hybridization that reached saturation in seconds to minutes, and were able to provide a quantitative determination of hybridization at nanomolar detection limits. Some important parameters, the length of tether, density of the probe molecules and ionic strength had been discussed to characterize the thermodynamic and kinetic performance of these biosensors in their papers. Rogers *et al.* [13] had established a method for detection of DNA damage exposed to ionizing radiation with fluorescently labeled complementary DNA sequence in the solution.

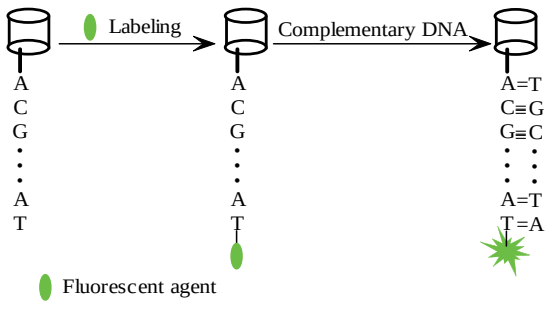

Figure 3. Scheme of fluorescent agents covalently bond to probe sequence immobilization on the exposed core of fiber-optic for detection of DNA hybridization.

These biosensors can be employed repeatedly and not require fluorescent agents in subsequent experiments. These fluorescence-label fiber-optic DNA biosensors had been extensively researched to detect the DNA hybridization or determine the DNA quantities, yet it was not to avoid the side effect on photoleaching that is intrinsic flaw. So some researchers had begun to study the label-free fiber-optic DNA biosensors.

4. LABEL-FREE FIBER-OPTIC DNA BIOSENSORS

Comparing with the large variety of labeled methods, few label-free methods, such as optical [38,39] acoustic [40,41] and electrochemical analytical methods [42,43, 44,45,46,47] could be applied to detect DNA hybridization. Label-free detection could remove experimental uncertainty induced by the effect of the label on molecular conformation, blocking of active binding epitopes, steric hindrance, inaccessibility of the labeling site, or the inability to find an appropriate label that functions equivalently for all molecules in an experiment, and greatly simplify the time and effort required for assay development, while removing experimental artifacts from quenching, shelf life and background fluorescence [48]. Optical DNA biosensors are easy to develop and commercialize for the detection of DNA hybridization, so fiber-optic will play an important role in label-free detection of DNA hybridization or single base mismatch. Here several fiber-optic DNA biosensors based surface plasmon resonance (SPR) [2,49,50,51], ellipsometry, evanescent wave are depicted below.

4.1. Surface Plasmon Resonance (SPR) Fiber-Optic DNA Biosensors

SPR is an optical reflectance procedure which is sensitive to changes in the optical properties of the medium close to a metal surface [52] and was employed for gene mutation [53], DNA hybridization [54,55] and virus [56]. In SPR fiber-optic DNA biosensors, ssDNA was immobilized onto the surface of ultrathin metal (Au or Ag) film of a lower refractive index deposited on the side of fiber-optic. When light penetrates through fiber-optic and on the metal surface satisfying the condition of surface plasmon resonance, the refractive index will be altered between metal film and solution interface to result in the change of resonant angle after DNA hybridization. The angle at which minimum reflection occurs is monitored and converted to the refractive index units for DNA quantification depending on notably refractive index, wavelength of incident light and properties of metal film [57].

Lin *et al.* [58] had investigated a multimode fiber sensor based on surface plasmon resonance with a halogen light source for detection of DNA hybridization. The side of fiber was polished and coated with 37nm gold

thin film to immobilize the probe DNA that hybrid with complementary DNA. The characteristics of SPR DNA biosensor, including the stability, repeatability and resolution calibration were examined as well. The resolution was 3×10^{-6} refractive index units and the SPR dip shift in wavelength which was hybridized at 0.1 μM of the target DNA to the probe DNA, was 8.66 nm.

4.2. Ellipsometry-Based Fiber-Optic DNA Biosensors

Ellipsometry is a versatile, sensitive and powerful optical technique for determining the properties of a material from the characteristics of light reflected from its sensing surface, which is non-destructive and contactless. Once the sample's properties, for example thickness, complex refractive index of thin films at interfaces were changed, the ellipsometry parameter was determined to calculate the surface concentration, and solution concentration. Wang [59] had elucidated the principle of waveguide ellipsometry sensors including light propagation in waveguide and ellipsometry parameter analysis, its arrangement and instrumentation, and preliminary experimental results are given as well. Ellipsometry-based sensors had been proposed for biosensor applications for monitoring protein-protein interactions [60,61].

Advantages of ellipsometry are present as follow:

1) The measurement is independent of light intensity and the waveguide coupler quality [60].

2) Optic fibers are feasible to fabricate the waveguide ellipsometry sensors because of their properties of low-cost, low loss, high performance, multicapability and security for application commercially.

3) Ellipsometry is less affected by intensity instabilities of the light source or atmospheric absorption.

4) High sensitivity and accuracy because of simultaneous determination of two parameters-relative phases and amplitudes.

Emma Hitt [62] thought imaging ellipsometry is suited for the detection of DNA hybridization to measure the change in the state of polarization of the light reflected, according to the EP3 ellipsometer. However, few information were occurred to directly study the DNA hybridization on the surface of fiber-optic by ellipsometry which was used to characterize the thickness of thin film or DNA interaction with surfactant [63,64,65].

4.3. Evanescent Wave-Based Fiber-Optic DNA Biosensors

Light transmits through fiber with different refractive index ($n_2<n_1$) at an angle beyond the critical angle for Total Internal Reflection (TIR), it will produce a limited attenuated electric filed transversely transporting though the side of fiber to form an evanescent waves (EW) that the intensity of evanescent waves decreases exponentially with short distance from the interface (see formula).

$$\frac{\lambda}{d_p} = 2\pi n_1 \sqrt{\sin^2\beta - \left(\frac{n_2}{n_1}\right)^2}$$

λ-Incident wavelength, d_p-Thickness of sensitivity, β-Critical angle of total internal reflection, n_1-Refractive index of core, n_2-Refractive index of coating.

The evanescent energy has an effect on DNA molecules in its sensitive distance. When the EW transmits through the sensitive element attached to the side of fiber-optic, the frequency, phase or intensity of light in fiber-optic will be altered with the quantity or the configuration of DNA molecules (**Figure 4**).

David Hradetzky *et al.* [66] had presented an evanescent wave sensing system based on the interferometric approach using Young's double slit configuration for detecting biomolecular interactions without labels. With refractometric measurements, a mean resolution of the effective refractive index was 0.9×10^{-6} and a reproducibility was below 0.1×10^{-6}. The hybridization of 21-mer DNA was detected using this highly sensitive biosensor. Rindorf *et al.* [67] have first presented incorporation of a microstructured optical fiber (MOF) into biochip. The MOF is functionalized towards the capture of a specific ssDNA by immobilizing a sensing layer on the internal surfaces of the fiber. Optical detection of the captured DNA was carried out using the evanescent-wave-sensing principle.

5. TRENDS

Fiber-optic-based DNA biosensors have been studied in all country providing much information about biological properties of DNA molecular recognition for medical diagnosis. The sensitivity, stability and response time are not optimal to the application and commercialization. It is necessary to develop the high-performance or new fiber-optic DNA biosensors. An efficient method will be applied to improve the sensitivity, stability and selectivity of fiber-optic DNA biosensors coupled with single-photon counter or optical computer. Combining with the nanoelectromechanical systems and nanotechnology, the portable, miniature and intelligent fiber-optic DNA nanobiosensors are exploited for in vivo measurement or in single cell monitoring to realize the single molecule

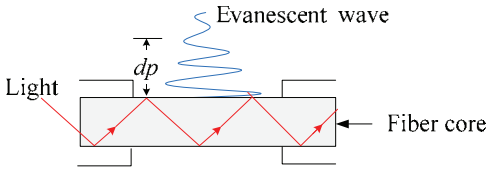

Figure 4. Schemes of evanescent field-based fiber-optic DNA biosensors without labeling.

detection. The kinetic studies demonstrated this surface modification to be superior to other methods of immobilization [68], so surface modification will be improved with advanced surface chemistry technique and new assembly technique to increase the stability, homogeneity, lifetime and frequency of fiber-optic DNA biosensors.

REFERENCES

[1] Uddin, A. H., Piunno, P. A., Hudson, R. H., Damha M. J., and Krull U. J., (1997) Nucleic Acids Research, **25(20)**, 4139–4146.

[2] Bates, P. J., Reddoch, J. F., Hansakul, P., Arrow, A., Dale, R., and Miller, D. M., (2002) Anal. Biochem., **307(2)** 235–243.

[3] Wang, J., Rivas, G., Cai, X., Palecek, E., Nielsen, P., Shiraishi, H., *et al*. (1997) Anal. Chim. Acta., **347(1)**, 1–8.

[4] Hoffmann, P., Dutoit, B., and Salathé, R. P., (1995) Ultramicroscopy, **6**, 165–170.

[5] Stöckle, R., Fokas, C., Deckert, V., Zenobi, R., Sick, B., Hecht, B., *et al*. (1999) Appl. Phys. Lett., **75(2)**, 160–162.

[6] Liu, X. M., Wang, J., and Li, D. C., (1998) Rev. Scient. Instrum., **69(9)**, 3439–3440.

[7] Lee, B., (2003) Optical Fiber Technology, **9(2)**, 57–59.

[8] Mitsuaki, W. and Kotaro, K., (2003) Sensors and Actuators B: Chemical, **89(1)**, 126–130.

[9] Han, Y. G., Tran, T. V. A., Kim, S. H., and Lee, S. B., (2005) Opt. Lett., **30(11)**, 1282–1284.

[10] Cullum, B. M., Griffin, G. D., Miller, G. H., and Vo-Dinh, T., (2000) Analytical Biochemistry, **277(1)**, 25–32.

[11] Chen, X., Zhang, L., Zhou, K., Davies, E., Sugden, K., and Bennion, I., *et al*., (2007) Opt. Lett., **32(17)**, 2541–2543.

[12] Vo-Dinh, T., Cullum, B. M., and Stokes, D. L., (2001) Sensors and Actuators B: Chemical, **74(1)**, 2–11.

[13] Rogers, K. R., Apostol, A., Steen, Madsen, J., and Spencer, C. W., (2001) Analytica Chimica Acta, **444(1)**, 51–60.

[14] Maxwell, D. J., Taylor, J. R., and Nie, S. M., (2002) J. Am. Chem. Soc., **124(32)**, 9606–9612.

[15] Zhang, D., Chen, Y., Chen, H. Y., and Xia, X. H., (2004) Anal. Bioanal. Chem., **379(7)**, 1025–1030.

[16] Li, J., Ng, H. T., Cassell, A., Fan, W., Chen, H., and Ye, Q., *et al*., (2003) Nano Lett., **3(5)**, 597–602.

[17] Balasubramanian, K. and Burghard, M., (2006) Anal. Bioanal. Chem., **385(3)**, 452–468.

[18] Li, Z., Rajendran, B., Kamins, T. I., Li, X., Chen, Y., and Williams, R. S., (2005) Applied Physics A: Materials Science & Processing, **80(6)**, 1257–1263.

[19] Zheng, G. F., Patolsky, F., Cui, Y., Wang, W. U., and Lieber, C. M., (2005) Nature Biotechnology, **23(10)**, 1294–1301.

[20] Cui, Y., Wei, Q. Q, Park, H. K, and Lieber, C. M., (2001) Science, **293 (5533)**, 1289–1292.

[21] Li, Z., Chen, Y., Li, X., Kamins, T. I., Nauka, K., and Williams, R. S., (2004) Nano Lett., **4(2)**, 245–247.

[22] Park, I., Li, Z. Y., Li, X. M., Pisano, A. P., and Williams, R. S., (2007) Biosensors and Bioelectronics, **22(9)**, 2065–2070.

[23] Kamins, T. I., Sharma, S., Yasseri, A. A., Li, Z., and Straznicky, J., (2006) Nanotechnology, **17(11)**, S291–S297.

[24] Lou, J. Y., Tong, L. M., and Ye, Z. Z., (2005) Optics express, **13(6)**, 2135–2140.

[25] Marazuela, M. and Moreno-bondi, M., (2002) Anal. Bioanal. Chem., **372(5)**, 664–682.

[26] Mehrvar, M., Bis, C., Scharer, J. M., Moo, M., and Luong, J. H., (2000) Analytical Sciences, **16(7)**, 677–692.

[27] Niu S. Y., Wang S. J., Shi C., Zhang S. S., (2008) J Fluoresc, **18**, 227–235.

[28] Piunno, P. A. E., Krull, U. J., Hudson, H. E., Damha, M. J., and Cohen, H., (1994) Analytica Chimica Acta, **288(3)**, 205–214.

[29] Svanvik, N., Stahlberg, A., Sehlstedt, U., Sjoback, R., and Kubsita, M., (2000) Anal. Biochem., **287(1)**, 179–182.

[30] Isacsson, J., Cao, H., Ohlsson, L., Nordgren, S., Svanvik, N., and Westman, G., *et al*., (2000) Mol. Cell Probes, **14(5)**, 321–328.

[31] Svanvik, N., Westman, G., Wang, D., and Kubsita, M., (2000) Anal. Biochem., **281(1)**, 26–35.

[32] Svanvik, N., Nygren, J., Westman, G., Kubsita, M., (2001) J. Am. Chem. Soc., **123(5)**, 803–809.

[33] Piunno, P. A. E., Krull, U. J., Hudson, H. E., Damha, M. J., and Cohen, H., (1995) Anal. Chem., **67(15)**, 2635–2643.

[34] Monk, D. J. and Walt, D. R., (2004) Anal. Bioanal. Chem., **379(7)**, 931–945.

[35] Wang, X. F. and Krull, U. J., (2002) Analytica Chimica Acta, **470(1)**, 57–70.

[36] Wang, X. F. and Krull, U. J., (2005) J. Mater. Chem., **15(27),** 2801–2809.

[37] Wang, X. F. and Krull, U. J., (2005) Bioorg. Med. Chem. Lett., **15(6)**, 1725–1729.

[38] Baird, C. L. and Myszka, D. G., (2001) J. Mol. Recognit., **14(5)**, 261–268.

[39] Rich, R. L. and Myszka, D. G., (2002) J. Mol. Recognit., **15(6)**, 352–376.

[40] Hur, Y., Han, J., Seon, J., Pak, Y. E., and Roh, Y., (2005) Sensors and Actuators A: Physical, **120(2)**, 462–467.

[41] Minunni, M., Mannelli, I., Spiriti, M. M., Tombelli, S., and Mascini, M., (2004) Analytica Chimica Acta, **526(1)**, 19–25.

[42] Xu, Y., Jiang, Y., Yang, L., He, P. G., and Fang, Y. Z., (2005) Chinese Journal of Chemistry, **23(12)**, 1665–1670.

[43] Chen, Y., Elling, Lee, Y., and Chong, S., (2006) J. Phys. Conf. Ser., **34**, 204–209.

[44] Kerman, K., Morita, Y., Takamura, Y., and Tamiya, E., (2005) Anal. Bioanal. Chem., **381(6)**, 1114–1121.

[45] Kerman, K., Morita, Y., Takamura, Y., and Tamiya, E., (2003) Electrochem. Comm., **5(10)**, 887–889.

[46] Peng, H., Soeller, C., Vigar, N., Kilmartin, P. A., Cannell, M. B., Bowmaker, G. A., *et al*. (2005) Biosensors and Bioelectronics, **20(9)**, 1821–1828.

[47] Mir1, M. and Katakis, I., (2005) Anal. Bioanal. Chem., **381(5)**, 2618–2642.
[48] Li, P. Y., Lin, B., Gerstenmaier, J., and Cunningham, B. T., (2004) Sensors and Actuators. B: Chemical, **99(1)**, 6–13.
[49] Bianchi, N., Rutigliano, C., Tomassetti, M., Feriotto, G., Zorzato, F., and Gambari, R., (1997) Clin. Diagn. Virol., **8(3)**, 199–208.
[50] Minunni, M., Tombelli, S., Mariottie, E., and Mascini, M., (2001) Fresenius J. Anal. Chem., **369(7)**, 589–593.
[51] Persson, B., Stenhag, K., Nilsson, P., Larsson, A., Uhlen, M., and Nygren, P., (1997) Anal. Biochem., **246(1)**, 34–44.
[52] Collings, A. F. and Caruso, F., (1997) Rep. Prog. Phys., **60(11)**, 1397–1445.
[53] Jiang, T., Minunni, M., Wilson, P., Zhang, J., Turner, A. P. F., and Mascini, M., (2002) Biosensors and Bioelectronics, **20(10)**, 1939–1945.
[54] Peterlinz, K. A., Georgiadis, R. M., Herne, T. M., and Tarlov, M., (1997) J. Am. Chem. Soc., **119(14)**, 3401–3402.
[55] Peterson, A. W., Wolf, L. K., and Georgiadis, R. M., (2002) J. Am. Chem. Soc., **124(49)**, 14601–14607.
[56] Bianchi, N., Rutigliano, C., Tomassetti, M., Feriotto, G., Zorzato, F., and Gambari, R., (1997) Clin. Diagn. Virol., **8(3)**, 199–208.
[57] Kambhampati, D. K. and Knoll, W., (1999) Current Opinion in Colloid & Interface Science, **4(4)**, 273–280.
[58] Lin, H. Y., Tsai, W. H., Tsao, Y. C., and Sheu, B. C., (2007) Applied Optics, **46(5)**, 800–806.
[59] Wang, J. Y., (1992) SPIE Fiber Optic Medical and Fluorescent Sensors and Applications, **1648**, 44–50.
[60] Tiberg, F., Brink, C., Hellsten, M., and Holmberg, K., (1992) Colloid & Polymer Science, **270(12)**, 1188–1193.
[61] Mahltig, B., Werner, C., Müller, M., Jérôme, R., and Stamm, M., (2001) Journal of Biomaterials Science, Polymer Edition, **12(9)**, 995–1010.
[62] Emma Hitt, (2005) Drug Discovery & Development, http://cmliris.harvard.edu/news/2004/DrugDiscDev_Sep04.pdf.
[63] McLoughlin, D. and Langevin, D., (2004) Physicochemical and Engineering Aspects, **250**, 79–87.
[64] Wong, A. K. Y. and Krull, U. J., (2005) Anal. and Bioanal. Chem., **383(2)**, 187–200.
[65] Shabani, A., Mak, A. W. H., Gerges, I., Cuccia, L. A., and Lawrence, M. F., (2006) Talanta, **70(3)**, 615–623.
[66] Hradetzky, D., Mueller, C., and Reinecke, H., (2006) J. Opt. A: Pure Appl. Opt., **8(7)**, S360–S364.
[67] Rindorf. L., Høiby, P. E., Jensen, J. B., Pedersen, L. H., Bang, O., and Geschke, O., (2006) Anal. Bioanal. Chem. **385(8)**, 1370–1375.
[68] Zeng, J., Almadidy, A., Watterson, J., and Krull, U. J., (2003) Sensors and Actuators B: Chemical, **90(1)**, 68–75.

J. Biomedical Science and Engineering, 2009, 2, 318-322 **JBiSE**
doi: 10.4236/jbise.2009.25047 Published Online September 2009 (http://www.SciRP.org/journal/jbise/).

Dendritic compound of triphenylene-*2*,*6*,*10*-trione ketal-tri-{*2*,*2*-di-[(*N*-methyl-*N*-(*4*-pyridinyl) amino) methyl]-*1*,*3*-propanediol}: an easily recyclable catalyst for Morita-Baylis-Hillman reactions

Rong-Bao Wei, Hong-Lin Li*, Ya Liang, Yan-Ru Zang

School of Chemistry and chemical Engineering, Tianjin Institute of Technology, Tianjin, China.
Email: hlli515@163.com

Received 11 April 2009; revised 10 May 2009; accepted 13 May 2009.

ABSTRACT

A novel Dendritic Compound (2) of triphenylene-*2,6,10*-trione ketal-tri-{*2,2*-di-[(*N*-methyl-*N*-(*4*-pyridinyl) amino)methyl]-*1,3*-propanediol} was conveniently synthesized by aromatization of cyclohexanedione mono-ketal, ketal-exchange reaction with *2,2*-dibromomethyl-*1,3*-propanediol and nuclophilic substitution with N-methylaminopyridine as nuclophilic reagent. The Morita-Baylis-Hillman reaction of various aryl aldehydes with methyl vinyl ketone and acrylonitrile in (DMF/cyclohexane, 1/1, v/v) has been investigated by using Dendritic Compound (2) as catalyst. The corresponding Morita-Baylis-Hillman adducts was obtained in good yields by using the recycled and reactivated dendritic catalyst.

Keywords: Morita-Baylis-Hillman Reaction; Methyl Vinyl Ketone; Aryl Aldehydes; Dendritic Compound; DMAP

1. INTRODUCTION

The Morita-Baylis-Hillman reaction possesses cheap and easy availability of starting materials, easing performance, atom economy, forming chemo-specific functional groups in the product, providing an avenue for introducing asymmetry, and fitting for simulation on the solid phase as a prelude for combinatorial synthesis represent some of the reasons, which have led to an exponential increase in the synthetic utility of this reaction [1,2,3,4,5,6,7,8,9,10]. The Morita-Baylis-Hillman reaction can be promoted by using organic bases. However, almost all the Morita-Baylis-Hillman reactions reported so far use small molecular homogeneous catalyst, and it impedes the reusing of the catalyst. In addition, this reaction could be accomplished in a perfect atom-economic way if a recyclable Lewis base was employed as the promoter. Recently, Corma *et al*. [11] developed a heterogeneous catalyst system by using an insoluble Merrifield type resin-supported 4-(*N*-benzyl-*N*-methyl amino)pyridine as reusable catalyst for the Morita-Baylis-Hillman coupling of aromatic aldehydes and unsaturated ketones. Shi [12] reported the use of soluble polymer-supported Lewis bases, such as PEG4600-(PPh2)2 and linear poly (DMAP) in the Morita-Baylis-Hillman reactions of *N*-tosylimines with unsaturated ketones.

Yang [13] employed the dendritic Lewis base as the catalyst together with a binary solvent system (DMF-cyclohexane, 1:1, v/v) ,which could become homogeneous when heated up to 60˚C and then could be readily separated by cooling the system to room temperature. Several other examples of immobilized praline are reported in literature: poly-(ethylene glycol)-supported praline [14], proline immobilized on polyethyleneglycol grafted on cross-linked polystyrene [15], proline immobilized on mesoporous silica [16], polystyrene-supported praline [17] or polymer-supported proline-decorated dendrons [18,19].

Dendritic compound of triphenylene-*2*,*6*,*10*-trione ketal-tri-{*2*,*2*-di-[(*N*-methyl-*N*-(*4*-pyridinyl) amino) methyl]-1,3-propanediol} provided the following key advantages: a) reaction system provides complete miscibility under the reaction temperature; b) the structure of dendrier catalyst is well-defined; c) the dosage of catalyst is less than other catalysts.

2. RESULTS AND DISCUSSION

We chose a dendritic compound of triphenylene-*2*,*6*,*10*-trione ketal-tri-{*2*,*2*-di-[(*N*-methyl-*N*-(*4*-pyridinyl) amino)methyl-1,3-propanediol} **2** as catalyst for Morita-Baylis-Hillman reaction, which was conveniently prepared according to following synthesis procedure (Scheme 1).

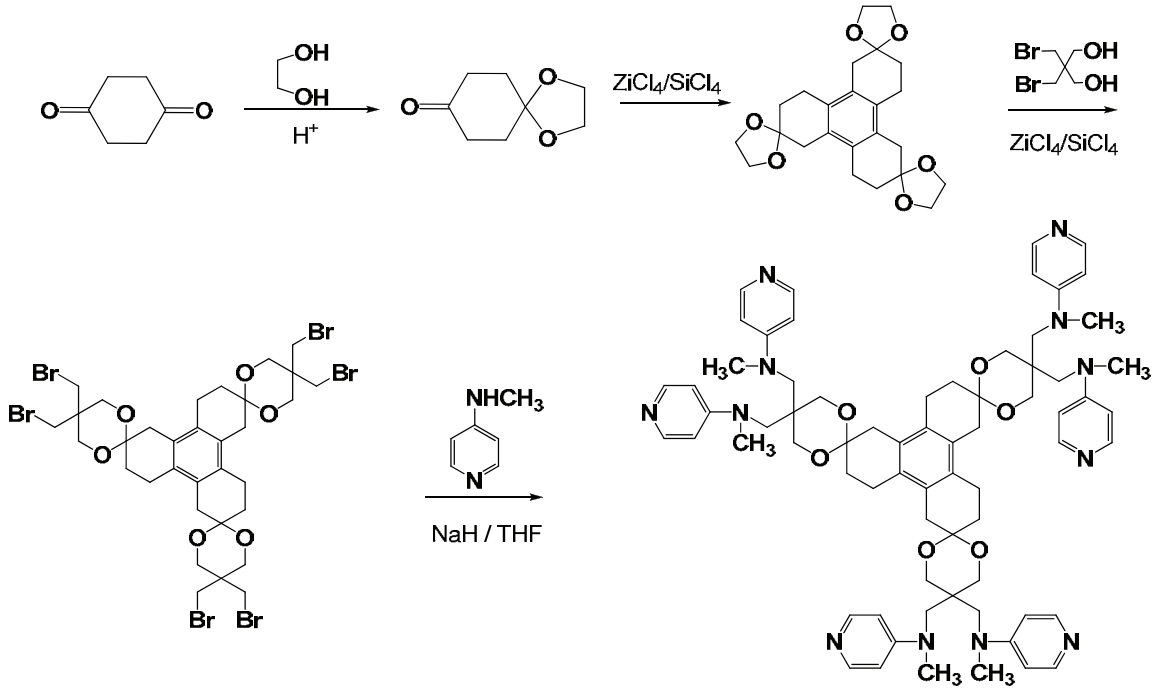

(1) (2)

Scheme 1

The Compound **(1)** was prepared by one-pot method. Through the exchange reaction after the aromatization, the five-membered ketal transformed to the more stable six-membered ketal. It omitted the hydrolysis of the ketal and separation steps. The reaction was in the Lewis acid, so the dehydration was reduced.

Because Compound **(1)** contains six bromine atoms, the amount of the alkaline must be controlled seriously in case of more side-reaction such as HBr elimination. The content of 30%NaH should be tested before use. Even so, they were forming some cross linked macromolecules. These were obviously increased in the NaOH/H_2O system.

The advantages of grafted DMAP to dendritic compound are as follows: for the macromolecular compound can be dissolved in most of the organic solvent instead of water, so it can be isolated by adding water after reaction and be used after activation by alkaline; for it has large cavities and dissolves in organic phase, it is helpful for contacting the reactant and catalyst and thus the reaction rate is higher than that of the polymer carried DMAP. So it combines the advantages of both forms of DMAP.

In order to determine the activity of this dendritic catalyst, we chose the coupling of 4-nitrobenzaldehyde with methyl vinyl ketone (MVK) as the model reaction, which is a paradigmatic example of the Morita-Baylis-Hillman reaction. In all cases only the normal Morita-Baylis-Hillman product was found [20,21,22]. The results were summarized in **Table 1**. As seen from the table, the highest yield was achieved when the molar ratio of aldehyde:MVK: dendritic-DMAP being 1:3:0.2, making it in the condition that the reacting time reach 48 h (**Table 1**, Entry **5**).

The dendritic catalyst could be easily recovered by cooling the reaction mixtures to room temperature and adding water at the end of the reaction. In order to regain the catalyst activity, the deactivated catalyst was treated with 2M NaOH at 45˚C for 2 h and subsequent was applied to the reaction under the same conditions, giving good yields. (see **Table 1**: Entries (9-13))

To demonstrate the applicability of dendritic DMAP as a homogeneous catalyst for the Morita-Baylise-Hillman reaction, various aldehydes were tested as reactants reacting with MVK or acrylonitrile and the results are shown in **Table 2**. It was found that the aryl aldehydes had strongly electron-withdrawing groups on the benzene rings such as dinitrobenzaldehyde and nitrilbenzaldehydes reacting with MVK and acrylonitrile gave the corresponding Morita-Baylis-Hillman adducts with high yields (1a,2a, 4a,7a,10a, 1b,2b, 4b,7b,10b). On the contrary, other aryl aldehydes, in particular with electron-donating substituents, provided low yields.

3. CONCLUSIONS

In summary, we have described a new catalytic system by using dendritic derivative of 4-(*N*,*N*-dimethylamino) pyridine as catalyst for the Morita-Baylis-Hillman reactions of aryl aldehydes with MVK and acrylonitrile. The recyclability and applicability of this catalytic system has been well demonstrated.

Table 1. Morita-Baylis-Hillman Reactions of 4-nitrobenzaldehyde (1.0 equiv.) with MVK in the presence of Cat 1.

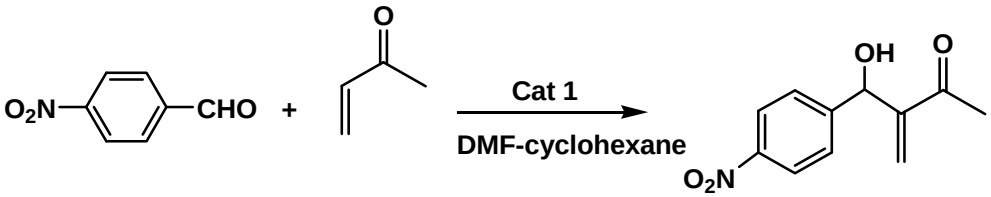

Entry	Aldehyde: MVK: Cat 1(mol)	Time (d)	Ylide(%)
1	1:1:0.2	0.5	30.5
2	1:2:0.2	0.5	45.3
3	1:3:0.2	0.5	49.7
4	1:4:0.2	0.5	50.1
5	1:3:0.2	1	88.6
6	1:3:0.2	2	90.5
7	1:3:0.2	3	90.0
8	1:3:0.2	4	89.4
9	1:3:0.2	2	90.5
10	1:3:0.2	2	90.5
11	1:3:0.2	2	90.5
12	1:3:0.2	2	90.5
13	1:3:0.2	2	90.5

Cat 1 is the Compound **(2)**

Table 2. The Baylis-Hillman reactions of aryl aldehydes with active alkene in the presence of Cat 1.

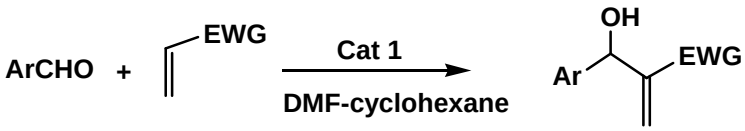

Enty	Ar	EWG	Time(d)	Yield(%)
1	4-NO_2-C_6H_4CHO	2	1a	92.2
2	2-NO_2-C_6H_4CHO	2	2a	92.2
3	3-NO_2-C_6H_4CHO	2	3a	82.2
4	4-CN-C_6H_4CHO	2	4a	90.2
5	4-Cl-C_6H_4CHO	2	5a	82.2
6	4-Br-C_6H_4CHO	2	6a	72.2
7	4-NO_2-C_5H_4NCHO	2	7a	90.2
8	4-CH_3O-C_6H_4CHO	2	8a	32.2
9	3-CH_3O-C_6H_4CHO	2	9a	52.2
10	3,4-dinitro-C_6H_3CHO	$COCH_3$	2	98.5
11	3,4-dinitro-C_6H_3CHO	CN	2	97.9
12	4-NO_2-C_6H_4CHO	CN	2	95.2
13	2-NO_2-C_6H_4CHO	CN	2	94.7
14	3-NO_2-C_6H_4CHO	CN	2	87.9
15	4-CN-C_6H_4CHO	CN	2	89.2
16	4-Cl-C_6H_4CHO	CN	2	84.2
17	4-Br-C_6H_4CHO	CN	2	79.5
18	4-NO_2-C_5H_4NCHO	2	7b	95.3
19	4-CH_3O-C_6H_4CHO	2	8b	40.3
20	3-CH_3O-C_6H_4CHO	2	9b	56.2
21	C_6H_5CHO	$COCH_3$	2	52.6
22	C_6H_5CHO	CN	2	47.2

Cat 1 is the Compound **(2)**

4. EXPERIMENTAL

4.1. General Remarks

Aryl aldehydes and acrylonitrile were stored under a nitrogen atmosphere before using. Other commercially supplied reagents were used as 4supplied without further purification. Organic solvents were dried by standard methods when necessary.

1H NMR spectra were recorded on an INOVA400 spectrometer for solution in CDCl3 with TMS as internal standard. Varian MAT 44S MS; Cavlo Eba 1106 elemental analysis instrument; WRR melting point apparatus (Shanghai Precision Instrument Co. Ltd.).

4.2. Synthesis of Dendrimer Compound (2)

$ZrCl_4/SiCl_4$ (0.5g, 1:1 in weight) was added to dissolving 1,4-cyclohexane-dione mono-ketal ethylene diol (1.56g, 10 mmol) in anhydrous ethanol (100mL). It was refluxed for 10~12 h and controlled by TCL until the 1, 4-cyclohexane-dione mono-ketal ethylene diol almost disappeared. After cooling, 2,2-dibromomethyl-1,3-propanediol (3.93g, 15 mmol) was added and refluxed for 9~12 h. Then cooling to room temperature, Ethanol was removed to 1/3 by evaporation. The raw product was crystallized by isopropyl alcohol. Compound (**1**) (2.95g) was obtained. Yield: 88.2%. M.p.:247~248℃ (decomposed).

M^+ :1013, C%: 39.14(39.08), H%:4.20(4.17), Br%: 47.27（47.28）. IR(KBr,cm^{-1}):2897,2860, 1465,1357; 1H-NMR ($CDCl_3$,δppm): 3.55 (2H,s,O-CH_2) 2.62 (2H, s,Br -CH_2), 2.02 (2H,t, J = 7.4 Hz CH_2), CH_2), 1.85(2H,t, J = 7.4 Hz CH_2), 1.52(2H,s,CH_2).

In the protection of N_2, 30 % NaH (0.48 g, 0.006 mol) was added to dissolving *N*-methyl-4-aminopyridine (0.65 g,6 mmol) in anhydrous THF (100 mL). It was refluxed for 1~2 h. After cooling, Compound (**1**) (1.01g, 1mmol) was added and refluxed for 10~15 h until *N*-methyl-4-amino pyridine could not be examined by TCL. THF was removed to 2/3 by evaporation. After cooling and filtering, the product was crystallized by $CHCl_3$:C_2H_5OH. Compound **(2)** (0.98g) was obtained. Yield: 83.5%. M.p.>300℃(decomposed).

M^+:1176.5, C%: 70.44(70.38), H%: 7.23(7.19), N%: 14.30（14.27 .IR(KBr,cm-1):3112, 3008,2875, 2861, 1605,1465,1375; 1H-NMR ($CDCl_3$,δppm): 8.41(2H, d, J = 8.0 Hz, Ar), 7.85(2H, d, J = 8.0 Hz, Ar), 3.54 (2H, s,O-CH_2) 2.64(2H,s,N-CH_2), 2.02(2H,t, J = 7.4 Hz CH_2), 1.98(2H,s, N-CH_2),1.85(2H,t, J = 7.4 Hz CH_2), 1.52 (2H,s,CH_2).

4.3. General Procedure for the Morita-Baylis-Hillman Reaction of Aryl Aldehydes with MVK and Acrylonitrile

To a 50ml bottom flask charged with aryl aldehydes (5.0 mmol) and dendritic DMAP (0.2 mmol) in 20ml DMF was added methyl vinyl ketone (MVK) (15.0 mmol) or acrylonitrile (15.0 mmol) under nitrogen atmosphere and the reacted mixture was stirred 48 h at 60℃. At the end of the reaction, the reacted mixture was cooled back to 25℃ and then adding 20ml water to the reacted mixture. The catalyst was recovered by filtration. The product was remained in the DMF/water layer, the solvent was removed under reduced pressure, and the residue was further purified by recrystalization

4.4. Characterization of the Morita-Baylis-Hillman Reaction Adducts

Compounds **1a**, **2a**, **4a**, **5a**, **6a**, **8a**,**11a,** and **1b**, **2b**, **4b**, **5b**, **6b**, **8b**,**11b** have been successfully characterized in the literature [23].

Compound **3a** ^{1}H NMR ($CDCl_3$, 400 MHZ, TMS): δ 2.35(3H, s, Me), 3.00 (1H, br., s, OH) 5.63 (1H, s, CH), 6.01 (1H,s, olefinic), 6.24 (1H, s, olefinic), 7.40 (1H, m, Ar), 8.12 (1H, m, Ar), 8.15 (1H, m, Ar), 8.25 (1H, m, Ar).

Compound **3b** ^{1}H NMR ($CDCl_3$, 400 MHZ, TMS): 3.00 (1H, br., s, OH) 5.63 (1H, s, CH), 6.11 (1H,s, olefinic), 6.27 (1H, s, olefinic), 7.35 (1H, m, Ar), 8.00(1H, m, Ar), 8.10 (1H, m, Ar), 8.20 (1H, m, Ar).

Compound **7a** ^{1}H NMR ($CDCl_3$, 400 MHZ, TMS): δ 2.35 (3H, s, Me), 3.00 (1H, br., s, OH) 5.63 (1H, s, CH), 6.01 (1H,s, olefinic), 6.24 (1H, s, olefinic), 7.59 (2H, d, J = 8.4 Hz, Ar),8.62 (2H, d, J = 8.0 Hz, Ar).

Compound **7b** ^{1}H NMR ($CDCl_3$, 400 MHZ, TMS): 3.00 (1H, br., s, OH) 5.63 (1H, s, CH), 6.01 (1H,s, olefinic), 6.24 (1H, s, olefinic), 7.50 (2H, d, J = 8.4 Hz, Ar),8.60 (2H, d, J = 8.0 Hz, Ar).

Compound **9a** ^{1}H NMR ($CDCl_3$, 400 MHZ, TMS): δ 2.00 (1H, br., s, OH), 2.13 (3H, s, Me), 3.87 (3H, s, OCH_3), 5.80 (1H, s, CH), 5.83 (1H, s, olefinic), 6.02 (1H, s, olefinic), 6.87-7.47(4H, m, Ar).

Compound **9b** ^{1}H NMR ($CDCl_3$, 400 MHZ, TMS): δ 2.00 (1H, br., s, OH), 3.87 (3H, s, OCH_3), 5.80 (1H, s, CH), 5.83 (1H, s, olefinic), 6.02 (1H, s, olefinic), 6.87-7.47(4H, m, Ar).

Compound **10a** ^{1}H NMR ($CDCl_3$, 400 MHZ, TMS): δ 2.35(3H, s, Me), 3.00 (1H, br., s, OH) 5.63 (1H, s, CH), 6.01 (1H,s, olefinic), 6.24 (1H, s, olefinic), 7.49 (1H, d, J = 8.4 Hz, Ar),8.12 (1H, d, J = 8.0 Hz, Ar) , 9.15 (1H, d, J = 3.0 Hz, Ar).

Compound **10b** ^{1}H NMR ($CDCl_3$, 400 MHZ, TMS): 3.20 (1H, br., s, OH) 5.70 (1H, s, CH), 6.21 (1H,s, olefinic), 6.27 (1H, s, olefinic), 7.47 (1H, d, J = 8.4 Hz, Ar),8.10 (1H, d, J = 8.0 Hz, Ar) , 8.95 (1H, d, J = 3.0 Hz, Ar).

5. ACKNOWLEDGEMENTS

We appreciate the National Natural Science Foundation of China (G20472064) and the Tianjin Natural Science Foundation of China

(040884311).

REFERENCES

[1] Singh, V. and Batra, (2008) S., Tetrahedron, **64**, 4511.
[2] Burke, M. D., Berger, E. M., and Schreiber, S. T., (2003) Science, **302**, 613.
[3] Basavaiah, D., Rao, K. V., and Reddy, R. J., (2007) Chem. Soc. Rev., **36**, 1581.
[4] Masson, G., Housseman, C., and Zhu, J., (2007) Angew. Chem., Int. Ed., **46**, 4614.
[5] Roy, D. and Sunoj, R. B., (2007) Org. Lett., **9**, 4873.
[6] Robiette, R., Aggarwal, V. K., and Harvey, J. N., (2007) J. Am. Chem. Soc., **129**, 15513.
[7] Leadbeater N. E. and Marco M., (2002) Chem. Rev., **102**, 3217.
[8] McNamara, C. A., Dixon, M. J., Bradley, M., (2002) Chem. Rev., **102**, 3275.
[9] Basavaiah, D., Rao, A. J., and Satyanarayana, T., (2003) Chem. Rev., **103**, 811.
[10] Singh V. and Batra S., (2003) Tetrahedron, **64**, 4511.
[11] Corma, A., Garcia, H., Leyva, A., (2003) Chem. Commun., 2806.
[12] Huang, J. W. and Shi, M., (2003) Adv. Synth. Catal., **345**, 953.
[13] Yang, F. N., Gong, H., Tang, W. J., and Fan, Q. H. J., (2005) Molecular Cat. A: Chem., **233**, 55.
[14] Benaglia, M., Cinquini, M., Cozzi, F., Puglisi, A., and Celentano, G., (2002) Adv. Synth. Catal., **344**, 533.
[15] Akagawa, K., Sakamoto, S., and Kudo, K., (2005) Tetrahedron Lett., **46**, 8185.
[16] Calderon, F., Ferna′ndez, R., and Sa′nchez, F., (2005) Adv. Synth. Catal., **347**, 1395.
[17] Font, D., Bastero, A., Sayalero, S., Jimeno, C., Pericas, M. A., (2007) Org. Lett., **9**, 1943.
[18] Kehat, T. and Portnoy, M., (2007) Chem. Commun., 2823.
[19] Giacalone, F., Gruttadauria, M., Marculescu, A. M., Anna, F., and Noto, R., (2008) Catalysis Commun., **9**, 1477.
[20] Shi, M., Li, C. Q., and Jing, J. K., (2001) Chem. Commun., 833.
[21] Krishna, P. R., Manjuvani, A., and Kannan, V., (2004) Tetrahedron Lett., **45**,1183.
[22] Shi, M., Li, C. Q., and Jing, J. K., (2003) Tetrahedron, **59**, 1181.
[23] Yang, N. Y., Gong, H., Tang, W. J., Fan, Q. H., Cai, C. Q., and Yang, L. W., (2005) J Molecular Catal. A: Chem., **233**, 55.

J. Biomedical Science and Engineering, 2009, 2, 323-335 **JBiSE**
doi: 10.4236/jbise.2009.25048 Published Online September 2009 (http://www.SciRP.org/journal/jbise/).

CANFIS—a computer aided diagnostic tool for cancer detection

Latha Parthiban[1], R. Subramanian[2]

[1]Research Scholar in Pondicherry University and working in Aarupadai Veedu Institute of Technology, Chennai, India; [2]Department of Computer Science, Pondicherry University, Puducherry, India.
Email: [1]lathaparthiban@yahoo.com, [2]subbur@yahoo.com

Received 5 November 2008; revised 20 May 2009; accepted 25 May 2009.

ABSTRACT

In this investigation, an approach using Coactive Neuro-Fuzzy Inference System (CANFIS) as diagnosis system for breast cancer has been proposed on Wisconsin Breast Cancer Data (WBCD). It is occasionally difficult to attain the ultimate diagnosis even for medical experts due to the complexity and non-linearity of the relationships between the large measured factors, which can be possibly resolved with a human like decision-making process using Artificial Intelligence (AI) algorithms. CANFIS is an AI algorithm which has the advantages of both fuzzy inference system and neural networks and can deal with ambiguous data and learn from the past data by itself. The Multi Layer Perceptron Neural Network (MLPNN), Probabilistic Neural Network (PNN) Principal Component Analysis (PCA), Support Vector Machine (SVM) and Self Organizing Map (SOM) were also tested and benchmarked for their performance on the classification of the WBCD.

Keywords: Neural Network; Coactive Neuro-Fuzzy Inference Systems; Probabilistic Neural Network; Principal Component Analysis; Stern Series; Wisconsin Breast Cancer Data

1. INTRODUCTION

Breast cancer is the most common tumor-related disease among women throughout the world, and the mortality rate caused by breast cancer is dramatically increasing. The etiologies of breast cancer remain unclear and no single dominant cause has emerged [1]. Preventive way is still a mystery and the only way to help patients to survive is by early detection. If the cancerous cells are detected before spreading to other organs, the survival rate for patient is more than 97% [25] which is the motivation factor to develop this automated diagnostic tool. Again, a major class of problems in medical science involves the diagnosis of disease, based upon several tests performed upon the patient and this has given rise, over the past few decades, to computerized diagnostic tools, intended to aid the physician in making sense out of the confusing data [2].

There have been substantial previous research works with WBCD database to achieve an automatic ultimate diagnostic system. Genetic Algorithm (GA) [2,13], Fuzzy Inference Systems(FIS) [3,4], Neural Networks (NN) [5,12], Adaptive Boosting (AdaBoost) [6,10,11] and Neuro-Fuzzy Hybrid Models [4,8] have been applied to this problem. The performances of each inference system were evaluated by calculating the degree of correctness in predicted results against diagnosed results represented as PPV (Positive Predicted Value). Each system shows the PPV within the range from less than 60% (AdaBoost) up to over 95% (Neuro-Fuzzy Hybrid Models). Among those algorithms, Neuro-Fuzzy Hybrid models provide relatively remarkable performances in diagnosis. Those models are the combination of Neural Networks and Fuzzy Inference Systems encouraging the advantages and resolving the drawbacks of both NNs and FIS models.

For our experiments, after preprocessing and cleaning of clinical data from mammogram, a modified method of using CANFIS [8,9] was applied to attain the ultimate diagnosis as being either *benign* or *malignant*. In order to find the neural network model with the highest accuracy for classification of the WBCD, we implemented five types of classifiers: Multi Layer Perceptron Neural Network (MLPNN), Probabilistic Neural Network (PNN), Principal Component Analysis (PCA), Support Vector Machine (SVM) and Self Organizing Map (SOM). To achieve fast training, the weights of these classifiers were initialized with Stern series. In applying CANFIS and other artificial intelligent algorithm, the required system size is changed in proportion to the size

of the inference system such as the number of inputs, the number of internal nodes and the number of learning iteration. Among those critical factors of the inference system, the number of internal nodes and learning iteration are changeable only in the process of designing the system. Therefore, methods for reducing the number of input factors within range of not losing the accuracy of diagnosis were considered. For this purpose, we used two methods, which are decision tree [14] and the correlation coefficient between the individual inputs and the test diagnosis results. The overall process flow chart is presented in **Figure 1**.

The rest of this paper is organized as follows: In Section 2, we briefly describe the WBCD data, data cleaning and feature extraction, dominant input selection methods, a review of the classifiers that are considered and initializing the weight of neural networks with Stern series are presented. In Section 3, we present the diagnostic system using CANFIS. In Section 4, experimental results of the classifiers trained on composite features of the WBCD data is compared in terms of positive predicted value and discussion of the presented results is provided in the light of existing studies in the literature. In Section 5, we highlight the results of the paper and finally, in Section 6, we conclude the paper.

2. METHODS

2.1. Wisconsin Breast Cancer Database

The Wisconsin Breast Cancer Diagnosis (WBCD) database is the result of efforts provided by the University of Wisconsin Hospital based on microscopic examination of breast masses with fine needle aspirate tests. Fine needle aspiration of breast masses is a common non-invasive diagnostic test that obtains information needed to evaluate malignancy [3,15].

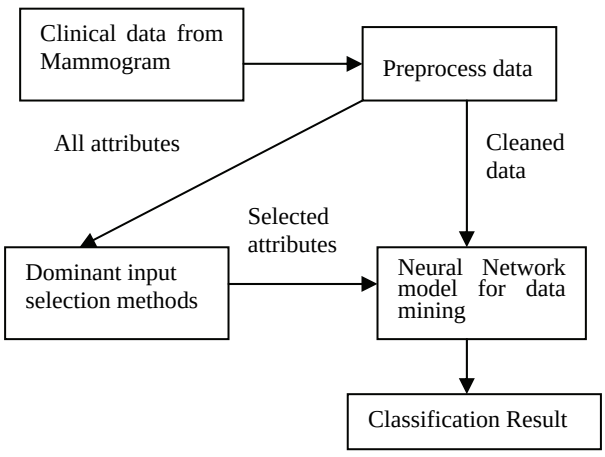

Figure 1. Overall processes flowchart.

Masses often characterize as early breast cancer before it is palpable by a woman or a physician [1]. It has its own characteristics and may be used as a clue to classify them. Masses can be circumscribed, speculated (satellite), lobulated or ill-defined (irregular) and radiologist will need to take a good look at its texture information, statistical descriptions as well as the background tissue from mammography images. Therefore, in order to classify a mass, the characteristics or attributes recorded were used as an input features. There are nine criteria recorded for masses in this dataset represented as a 1-10 integer value. (**Table 1**).

The database (**Table 2**) itself contains 699 cases, with 65.5% classified as benign and 34.5% as malignant. The diagnostics do not provide any information about the degree of benignity or malignancy. In considering the relationship between the measured values and the diagnostics, there are almost no relationships which stand out. Therefore, there is no convenient and effective method to attain the ultimate diagnostics with this original data even for the specialists.

In addition to that, there may be the possibility that one or more of the measured pieces do not affect the diagnosis result. These are the reasons that artificial intelligent system can be used as an expert to assist the specialist in diagnosing the disease correctly.

2.2. Data Cleaning and Feature Extraction

Preliminary examination on dataset chosen is compulsory before cleaning process takes place. By knowing the relationship between attributes, and how strongly they depend on each other, data quality and evaluation can be found easily. The discovery of data relationship

Table 1. Dataset features.

Criteria	Integer Value
Clump Thickness	X_1
Uniformity of Cell Size	X_2
Uniformity of Cell Shape	X_3
Marginal Adhesion	X_4
Single Epithelial Cell Size	X_5
Bare Nuclei	X_6
Bland Chromatin	X_7
Normal Nucleoli	X_8
Mitosis	X_9

Table 2. WBCD database.

Case	X_1	X_2	X_3	……..	X_9	Diagnostics
1	5	1	1	……..	1	Benign
2	5	4	4	……..	1	Benign
…	..	..	..	……..	..	…
…	..	..	..	……..	..	…
699	4	8	8	……..	1	Malignant

might lead to data cleaning rules, and therefore it can suggest improvements to its constraints. These are carried out by analyzing patterns between the attributes, using statistical tools like bivariate or multivariate analysis.

Therefore, two different cleaning processes have been carried out on the dataset. Dataset named Set A will only eliminate records with missing value and outliers, with the hypothesis that medical data are best not to be tampered or changed. While data in Set B will undergo normal statistical cleaning process where all attributes must be distributed normally. Therefore, data in Set B has been changed many times to fulfill the normal distribution functions

Using Neural Connection 2.0, 180 simulations was carried out for both dataset to test which data set is the best. As shown in **Figure 2**, set A gives 100% as the highest accuracy percentage (AP) and the smallest root mean squared (RMS) error is only 0.02751. As compared to set B, the highest AP is only 83.36% with smallest RMS error is 0.21002. It is proven that our hypothesis is true and therefore, set A will be used as an input database.

After data cleaning, the data in the WBCD database was divided into two sets: training and testing datasets. There are 444 benign and 238 malignant cases in the database. The training dataset constitutes 50% of WBCD database taken in order and the remaining is testing dataset. The training dataset was also used to figure out the most effective and dominant inputs of the inference system and the result with dominant inputs using decision tree and correlation coefficient computation was tested for correctness verification of the output.

2.3. Dominant Input Selection Methods

2.3.1. Decision Tree

The input recommender used in our experiment was a decision tree learning algorithm using SAS9™ package. The decision tree construction algorithms generate decision trees from a set D of cases. These algorithms partition the data set D into subsets D_1, D_2, ……D_M by a set of tests X with mutually outcomes X_1, X_2 ,……. X_M, where Dv contains those cases that have outcome X_i. A decision tree (DT) is known as a good classifier of huge data. It classifies input data by partitioning example spaces with entropy calculation. DT is especially useful when dataset is represented by attribute-value pairs and the target function has discrete output value. In our experiment, a binary decision tree was constructed to select dominant inputs. In each node of the tree, the most useful attribute for classifying whole data is selected by calculating the information gain (measure for deciding the relevance of an attribute) G (*D*, *X*) of an attribute X,

SET A DATASET										
architecture	9-3-1		9-3-2-1		9-4-1		9-5-1		9-6-1	
Average (%)	AP	Err	AP	Err	AP	Err	AP	Err	AP	Err
Gce	98.36	0.16486	98.26	0.16362	96.17	0.22439	97.57	0.13648	93.99	0.20895
Gse	98.66	0.10257	98.36	0.10857	98.36	0.07265	100	0.06127	94.54	0.19486
Gsp	88.84	0.22114	98.85	0.09264	100	0.016098	97.95	0.19020	97.27	0.15872
Uce	99.18	0.10076	91.76	0.21439	96.17	0.30317	96.72	0.17217	93.14	0.24408
Use	99.02	0.10022	88.13	0.22868	100	0.02804	99.18	0.06578	96.17	0.16622
Usp	91.88	0.21567	90.87	0.21386	100	0.21347	100	0.02751	97.27	0.18060
SET B DATASET										
architecture	9-3-1		9-3-2-1		9-4-1		9-5-1		9-6-1	
Average (%)	AP	Err	AP	Err	AP	Err	AP	Err	AP	Err
Gce	83.23	0.21002	70.32	0.32146	82.13	0.33121	56.89	0.34521	53.09	0.43553
Gse	83.36	0.31231	54.67	0.75463	76.56	0.43541	62.10	0.34562	62.34	0.56643
Gsp	77.08	0.43216	80.56	0.27643	67.67	0.56433	68.98	0.45632	67.09	0.65423
Uce	73.36	0.31200	75.89	0.54365	56.65	0.5674	66.43	0.56722	63.89	0.65545
Use	64.06	0.43009	78.65	0.65473	78.77	0.44120	71.56	0.45332	70.12	0.42119
Usp	57.12	0.65123	67.43	0.43301	77.05	0.54673	58.78	0.54667	57.09	0.6323

Figure 2. Simulations results of data Set A and Set B.

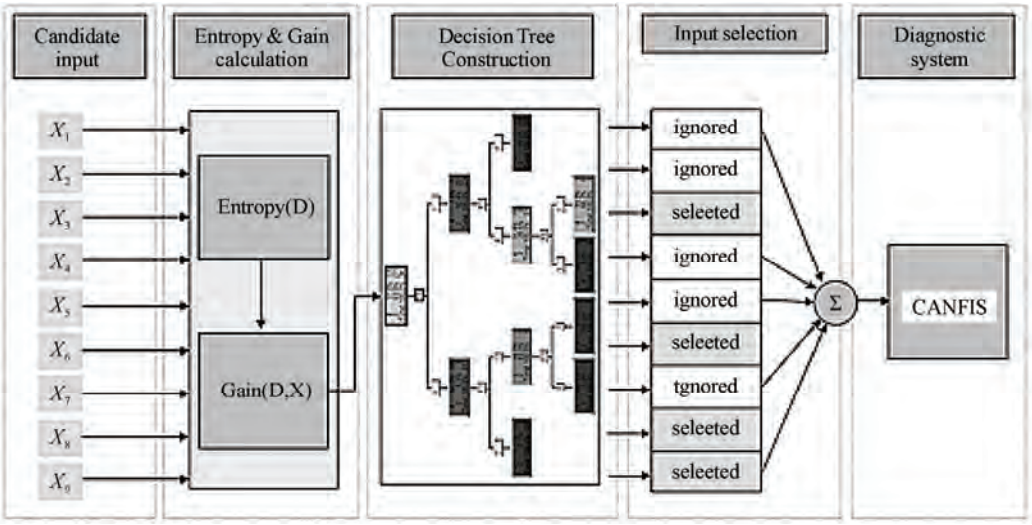

Figure 3. DT dominant input selection.

relative to a collection of examples X, with following formula.

$$Gain(D,X) = Entropy(D) - \sum_{v \in Values(X)} \frac{|Dv|}{|D|} Entropy(Dv)$$

and $Entropy(D) = \sum_{i=1}^{c} - p_i \log p_i$

where p_i denotes the proportion of classes in D that belong to the i^{th} class, *Values(X)* is the set of all possible values for attribute X, D*v* is a subset of D for which attribute X has a value v and. |Dv| represents cardinality of Dv dataset. (i.e., D={d ∈ D | X*(d)* = *v*}). The first term in the equation for *Gain* is just the entropy of the original collection D and the second term is the expected value of the entropy after D is partitioned using attribute *X*. The expected entropy described by this second term is simply the sum of the entropies of each subset *Dv*, weighted by the fraction of examples |*Dv*|/|*D*| that belong to *Dv*. *Gain* (*D,X*) is therefore the expected reduction in entropy caused by knowing the value of attribute *X*. Alternatively, *Gain*(*D,X*) is the information provided about the target attribute value, given the value of some other attribute *X*.

The DT is constructed in a way to reduce the entropy with the attribute which has the highest gain value at each node. Through this way, the final DT model has the most useful measured data on the top node, next useful one on the right node of the top node and so on. The input selection process derived by DT is presented in **Figure 3**.

2.3.2. Correlation Coefficient Computation

An efficient method for dominant input selecting process is calculating correlation coefficients between each measured input data and the diagnosis results. The Correlation Coefficient is a numerical measure of the degree of the linear relationship between two variables. The value of the correlation coefficient always falls between –1 and 1. A positive correlation coefficient indicates a direct relationship, and a negative correlation coefficient indicates an inverse relationship between two variables. In the calculation, first it is possible to assume that all the correlation coefficients by calculating with data in WBCD should be positive. Then we selected four measured input data from the one which has the highest correlation coefficient for diagnosis system. The correlation coefficient indicates the degree of linear relationship between two variables. The correlation coefficient always lies between -1 and +1. -1 indicates perfect linear negative relationship between two variables, +1 indicates perfect positive linear relationship and 0 indicates lack of any linear relationship The correlation coefficient(ρ_{ij}) can be calculated by the following formula.

$$\rho_{ij} = \frac{C_{ij}}{\sqrt{C_{ii} C_{jj}}} = \frac{\mathrm{cov}\,(X_i, X_j)}{\sigma(X_i)\,\sigma(X_j)} \quad (1)$$

$$C_{ii} = \sum (X_i - \overline{X})^2, C_{jj} = \sum (X_j - \overline{X})^2$$
$$C_{ij} = \sum (X_i - \overline{X})(X_j - \overline{X}) \quad (2)$$

where C_{ij} is the covariance of X_i and X_j, $\sum \overline{X}$ is the mean and $\sigma(X_i)$ is the standard deviation of X_i and $\sigma(X_j)$ is the standard deviation of X_j.

Each result by the correlation coefficient calculation between each measured input and the correct output indicates the degree of linear relationship between them. In this procedure, the selected input features are possibly said to have more linear relationships so that they affects the results. Therefore, the inputs highly correlated with the output were selected as dominant inputs in our experiment. The result of dominant input selection by the correlation coefficient calculation is given in **Figure 4**.

The CANCORR Procedure

Canonical Structure

Correlations Between the VAR Variables and Their Canonical Variables

		V1	rank
F1	F10	0.6974	8
F2	F10	0.9438	1
F3	F10	0.9058	3
F4	F10	0.8215	5
F5	F10	0.7953	6
F6	F10	0.8828	4
F7	F10	0.9257	2
F8	F10	0.7924	7
F9	F10	0.4274	9

Correlations Between the WITH Variables and Their Canonical Variables

		W1
F10	F10	1.0000

Correlations Between the VAR Variables and the Canonical Vairables of the WITH Variables

Figure 4. Correlation coefficient output.

2.4. Brief Review of Different Classifiers

1) Multilayer Perceptron Neural Network

The MLPNNs are the most commonly used neural-network architectures since they have features such as the ability to learn and generalize smaller training-set requirements, fast operation, and ease of implementation. One major property of these networks is their ability to find nonlinear surfaces separating the underlying patterns, which is generally considered as an improvement on conventional methods. The MLPNN is a nonparametric technique for performing a wide variety of detection and estimation tasks [12,17,18,19]. **Figure 5** shows the architecture of MLPNN. There is one neuron in the input layer for each predictor variable. In the case of categorical variables, *N*-1 neurons are used to represent the *N* categories of the variable.

Input Layer—A vector of predictor variable values ($x_1 ... x_p$) is presented to the input layer. The input layer (or processing before the input layer) standardizes these values so that the range of each variable is -1 to 1. The input layer distributes the values to each of the neurons in the hidden layer. In addition to the predictor variables, there is a constant input of 1.0, called the bias that is fed to each of the hidden layers; the *bias* is multiplied by a weight and added to the sum going into the neuron.

Hidden Layer—Arriving at a neuron in the hidden layer, the value from each input neuron is multiplied by a weight (w_{ji}), and the resulting weighted values are added together producing a combined value u_j. The weighted sum (u_j) is fed into a transfer function, σ, which outputs a value h_j. The outputs from the hidden layer are distributed to the output layer.

Output Layer-Arriving at a neuron in the output layer, the value from each hidden layer neuron is multiplied by a weight (w_{kj}), and the resulting weighted values are added together producing a combined value v_j. The weighted sum (v_j) is fed into a transfer function, σ, which outputs a value y_k. The y values are the outputs of the network.

The algorithm for the MLPNN is given below. It requires the units to have thresholding non linear functions that are continuously differentiable, i.e., smooth everywhere. A sigmoid function f (net)=1/(1+e^{-knet}), is used, since it has a simple derivative. All training and testing data were normalized.

Initialize weights and thresholds:

Set all weights and thresholds to small random variable.

Present input and desired output:

Present input: $X_P = x_1, x_2, \ldots\ldots\ldots\ldots x_p$

Target output: $Y_P = y_1, \ldots\ldots\ldots\ldots y_m$

where, p is the number of input nodes and m is the number of output nodes. Set w_0 to be -θ, the bias, and x_1 to be always 1.

For pattern association, X_P and Y_P represent the patterns to be associated. For classification, Y_P is set to zero except for one element set to 1 that corresponds to the class the X_P is in.

Calculation of actual output:

Each layer calculates $Y_{pi} = f\left(\sum_{i=0}^{n-1} w_{i,x_i}\right)$ and passes it as input to the next layer. The final layer outputs values O_{pj} and passes that as input to the next layer.

Adapt weights (start from control layer, and work backwards):

$$w_{ij}(t+1) = w_{ij}(t) + \eta\, \delta_{pj} O_{pj}$$

where, $w_{ij}(t)$ represents the weights from node i to node j at time t, η is a gain term, and δ_{pj} is an error term for pattern p on node j.

For output units: $\delta_{pj} = k\, O_{pj}\,(1 - O_{pj})\,(t_{pj} - O_{pj})$

For hidden units: $\delta_{pj} = kO_{pj}\,(1 - O_{pj}) \sum \delta_{pk} w_{jk}$

where, the sum is over the k nodes in the layer above node j. The stopping condition may be weight change, number of epochs, and so on.

The main issues involved in designing and training a MLPNN are selecting how many hidden layers to use in the network, deciding how many neurons to use in each hidden layer, finding a globally optimal solution that avoids local minima, converging to an optimal solution in a reasonable period of time and validating the neural network to test for overfitting.

2) Probabilistic Neural Network

The PNN introduced by Specht [20] is essentially based on the well-known Bayesian classifier technique commonly used in many classical pattern-recognition problems. Consider a pattern vector x with m dimensions that belongs to one of two categories K_1 and K_2. Let $F_1(x)$ and $F_2(x)$ be the probability density functions (pdf) for the classification categories K_1 and K_2, respect

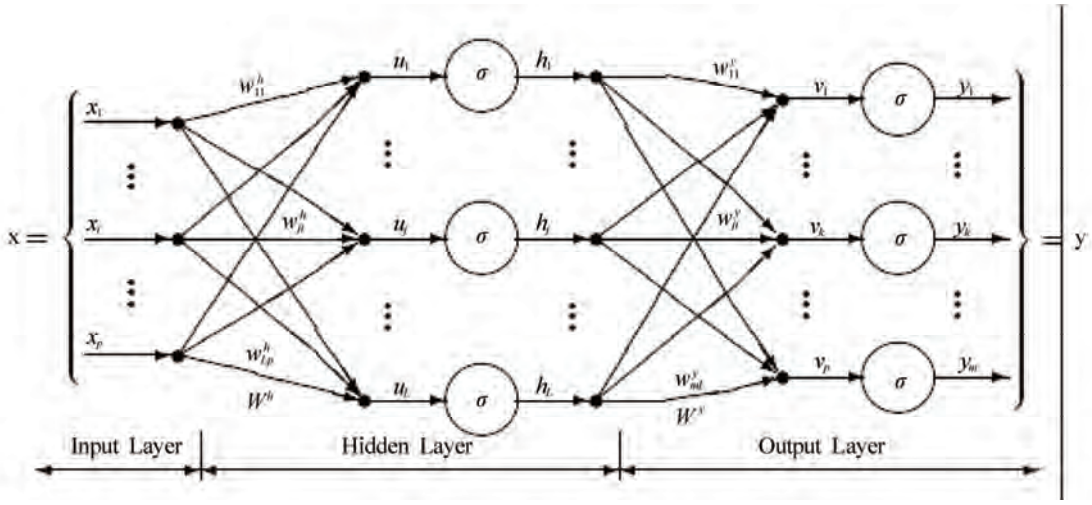

Figure 5. Architecture of MLPNN.

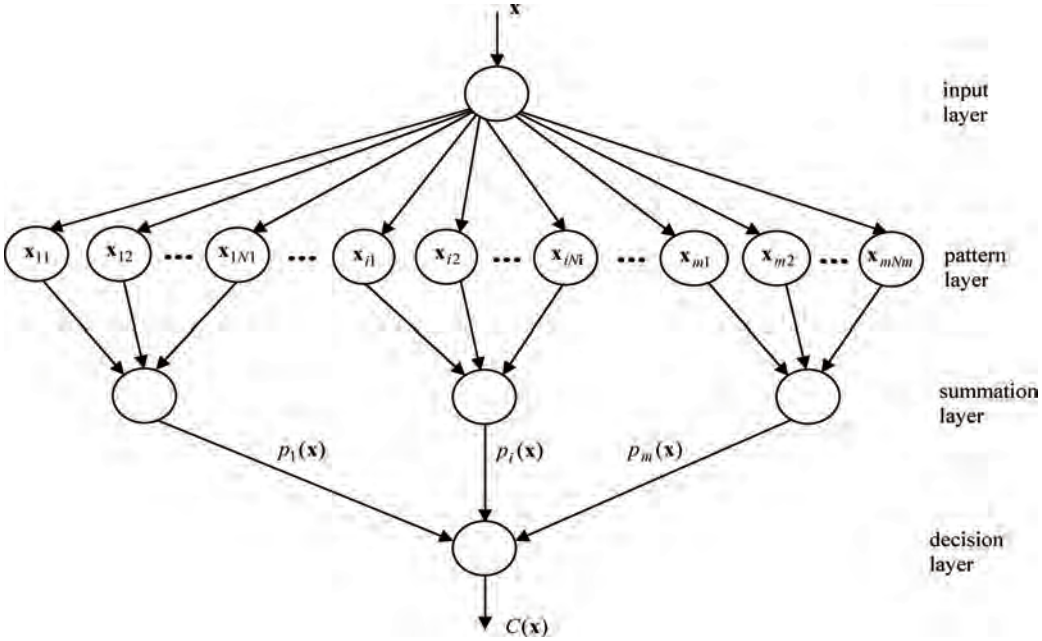

Figure 6. Architecture of PNN.

tively. From Bayes' discriminant decision rule, x belongs to K_1 if

$$\frac{F_1(x)}{F_2(x)} > \frac{L_1}{L_2}\frac{P_2}{P_1} \tag{3}$$

Conversely, x belongs to K_2 if

$$\frac{F_1(x)}{F_2(x)} < \frac{L_1}{L_2}\frac{P_2}{P_1} \tag{4}$$

where L_1 is the loss or cost function associated with misclassifying the vector as belonging to category K_1 while it belongs to category K_2, L_2 is the loss function associated with misclassifying the vector as belonging to category K_2 while it belongs to category K_1, P_1 is the prior probability of occurrence of category K1, and P_2 is the prior probability of occurrence of category K_2. In many situations, the loss functions and the prior probabilities can be considered equal. Hence the key to using the decision rules given by **Eq.3 and 4** is to estimate the probability density functions from the training patterns.

The PNN architecture (**Figure 6**) is composed of many interconnected processing units or neurons organized in successive layers. The input layer unit does not perform any computation and simply distributes the input to the neurons in the pattern layer. On receiving a pattern x from the input layer, the neuron x_{ij} of the pattern layer computes its output using

$$\varphi_{ij}(x) = \frac{1}{(2\pi)^{d/2}\sigma^d} exp\left[-\frac{(x-x_{ij})^T(x-x_{ij})}{2\sigma^2}\right] \quad (5)$$

where d denotes the dimension of the pattern vector x, σ is the smoothing parameter, and x_{ij} is the neuron vector [20,21].

For two class problem, if input units is assumed to be x_1 to x_n, Pattern units be Class A (Z_{A1} to Z_{Aj}) and Class B (Z_{B1} to Z_{Bj}), Summation units be f_A and f_B and output unit y, then the training algorithm for the probabilistic neural net is

Step 1: For each training input pattern, x(p), p=1,……P perform Steps 2-3.
Step 2: Create pattern unit Zp: Weight vector for unit Zp: w_p=x(p) (unit Zp is either a Z_A unit or Z_B unit)
Step 3: Connect the pattern unit to summation unit. If x(p) belongs to Class A, connect pattern unit Z_p to summation unit S_A. Else, connect pattern unit Z_p to summation unit S_B.

The application algorithm for classifying is given as
Step 1: Initialize weights from training algorithm.
Step 2: For input pattern to be classified, do Steps 3–5.
Step 3: Patterns units:
Calculate net input,
$Z_{inj} = x.w_j = x^T w_j$
Calculate the output
$Z=exp[[Z_{inj}-1]/\sigma^2]$
Step 4: Summation units
The weights used by the summation unit for Class B is,
$V_B = -P_B C_B m_A / P_A C_A m_B$
Step 5: Output unit:

It sums the signals from f_A and f_B. Input vector is classified as Class A if the total input to decision unit is positive.

The main advantage of PNN compared to MLPNN is

- faster to train a PNN network than a MLPNN.
- more accurate than MLPNN.
- insensitive to outliers (wild points).
- generate accurate predicted target probability scores.
- approach Bayes optimal classification.
- slower than MLPNN at classifying new cases.
- require more memory space to store the model

3) Support Vector Machine

The SVM proposed by Vapnik [22] has been studied extensively for classification, regression, and density estimation. The SVM is a binary classifier and it maps the input patterns into a higher dimensional feature space through some nonlinear mapping chosen *a priori*. A linear decision surface is then constructed in this high-dimensional-feature space. Thus, SVM is a linear classifier in the parameter space, but it becomes a nonlinear classifier as a result of the nonlinear mapping of the space of the input patterns into the high-dimensional feature space. Training the SVM is a quadratic-optimization problem. SVM has been shown to provide high- generalization ability. A proper kernel function for a certain problem is dependent on the specific data and till now there is no good method on how to choose a kernel function [22,23]. In this paper, the choice of the kernel functions was studied empirically and optimal results were achieved using radial-basis function (RBF) kernel function.

SVMs are free of optimization headaches of neural networks because they present a convex programming problem, and guarantee finding a global solution. They are much faster to evaluate than density estimators, because they make use of only relevant data points, rather than looping over each point regardless of its relevance to the decision boundary.

4) Self Organizing Maps

Self-organizing maps learn to classify input vectors according to how they are grouped in the input space. Feature maps allocate more neurons to recognize parts of the input space where many input vectors occur and allocate fewer neurons to parts of the input space where few input vectors occur. SOM also learn the topology of their input vectors. Neurons next to each other in the network learn to respond to similar vectors. The layer of neurons can be imagined to be a rubber net that is stretched over the regions in the input space where input vectors occur. SOM allow neurons that are neighbors to the winning neuron to output values. Thus the transition of output vectors is much smoother than that obtained with competitive layers, where only one neuron has an output at a time.

Initially, the weight and learning rate are set. The input vectors to be clustered are presented to the network. Once the input vectors are given, based on initial weights, the winner unit is calculated either by Euclidean distance method or sum of products method. An epoch is said to be completed once all the input vectors are presented to the network. By updating the learning rate, several epochs of training may be performed. The training algorithm for SOM is as below

Step 1: Set topological neighborhood parameters
Set learning rate, initialize weights.
Step 2: While stopping condition is false do Steps 3-9
Step 3: For each input vector x, do Steps 4-6.
Step 4: For each j, compute squared Euclidean distance.
$D(j)=\sum(W_{ij}-X_i)^2$ i =1 to n and j = 1 to m
Step 5: Find index J, when D(j) is minimum.
Step 6: For all units J with the specified neighbourhood of J, for all i, update the weights.
$W_{ij(new)} = W_{ij(old)} + \alpha[x_i - W_{ij(old)}]$
Step 7: Update the learning rate.
Step 8: Reduce the radius of topological neighborhood at specified times.
Step 9: Test the stopping condition.

The map formation occurs in two phases:

a) Initial formation of perfect (correct) order

b) Final convergence.

The second phase takes a longer duration than the first phase and requires a small value of learning rate. The learning rate is a slowly decreasing function of time and the radius of the neighborhood around a cluster unit also decreases as the clustering process goes on. The initial weights are assumed with random values. The learning rate is updated by $\alpha(t+1) = 0.5\alpha(t)$.

5) Principal Component Analysis

PCA network combine unsupervised and supervised learning in the same topology. PCA is an unsupervised linear procedure that finds a set of uncorrelated features, principal components, from the input. A MLP is supervised to perform the nonlinear classification from these components. PCA is a technique that finds an orthogonal set of directions in the input space and provides a way to find the projections into these directions in an ordered fashion. The orthogonal directions are called eigen vectors of the correlation matrix of the input vector and the projections of the corresponding eigen values.

a) Ordering of the principal components

PCA must transform the input samples into a new space (the feature space) such that the information about the samples is kept, but the dimensionality is reduced. From the input space, it finds an orthogonal set of P directions where the input data has the largest energy, and extracts P projections from these directions in an ordered fashion. The first principal component is the projection, which has the largest value (think of the projections as the shadow of the data clusters in each direction as in **Figure 7**), while the P^{th} principal component has the smallest value. If the largest projections are extracted, then the most significant information about the input data is kept. This segment of the network computes the eigenvectors of the input's correlation function without ever computing the correlation function itself. The outputs of the PCA layer are therefore related to the eigenvalues and can be used as input features to the supervised segment for classification. Since many of these eigenvalues are usually small, only the M (M<P) largest values need to be kept. This speeds up training even more.

The importance of PCA analysis is that the number of inputs for the MLP classifier can be significantly reduced. This results in a reduction of the number of required training patterns and a reduction in the training times of the classifier. Problem with linear PCA networks is evident when the input data contains outliers. Outliers are individual pieces of data that are far removed from the data clusters (i.e., noise). They tend to distort the estimation of the eigenvectors and create skewed data projections.

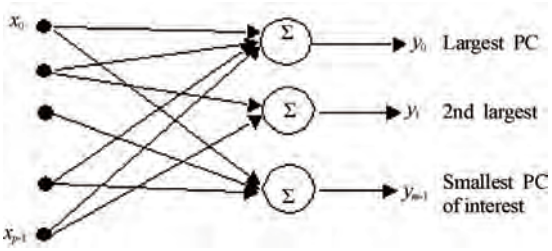

Figure 7. Ordering of the principal components.

6) Initializing Neural Networks with Stern Series

A Calkin-Wilf tree is a special type of binary tree obtained by starting with the fraction $1/1$ and iteratively adding $a/(a+b)$ and $(a+b)/b$ below each fraction a/b. The Stern-Brocot tree is closely related, putting $a/(a+b)$ and $b/(a+b)$ below each fraction a/b. Both trees generate every rational number. Writing out the terms in sequence gives 1/1, 1/2, 2/1, 1/3, 3/2, 2/3, 3/1, 1/4, 4/3, 3/5, 5/2, 2/5, 5/3, 3/4, 4/1,… as shown in **Figure 8**.

The sequence has the property that each denominator is the next numerator [26] and is known as Stern's diatomic series represented mathematically as

a(0) = 0, a(1) = 1; for n >= 0, a(2n) = a(n),
a(2n+1) = a(n) + a(n+1).

As an array the terms are:
1,2
1,3,2,3
1,4,3,5,2,5,3,4
1,5,4,7,3,8,5,7,2,7,5,8,3,7,4,5 and so on .
Finding 1/ [a(n)*a(n+1)] for each row
R=1 ½, ½
R=2 1/3,1/6,1/6,1/3
R=3 1/4,1/12,1/15,1/10,1/10,1/15,1/12,1/4 and so on.

Depending on the importance of a specific attribute chosen, we can initialize the weight of neural network with stern series for quick training. A tree showing the designed stern series for weight initialization is shown below in **Figure 9**.

The main impact of initializing the neural network weight with stern series is quick training period .The code for generating Stern series is given below.

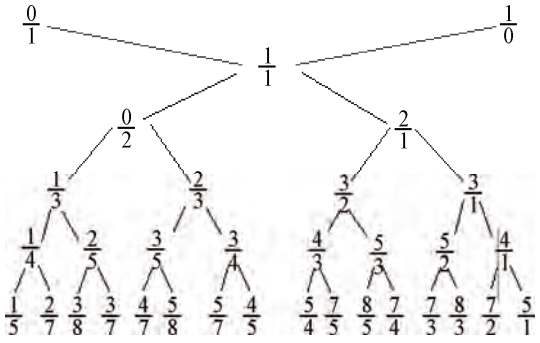

Figure 8. Stern-brocot tree.

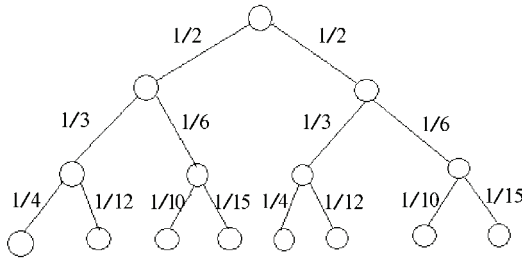

Figure 9. Weight initialization using stern sequence.

```
#include<iostream.h>
#include<conio.h>
static int ans=0;                    //STERN'S RESULT
void stern(int n)
{
    if(n==0||n==1)              //STERN'S ASSUMTION
      {   ans+=n; }
    else if(n%2==0)                  //STERN'S EVEN
       {   n=n/2;
          if(n>1)
                  { stern(n); }
          else
              { ans+=n;}
       }
    else
//STERN'S ODD
       {   n=n/2;
          stern(n);
          stern(n+1);
       }
}
void main()
{     textcolor(WHITE);
      textbackground(BLUE);
   clrscr();
   int                                                    n;
//STERN'S N
   gotoxy(33,3);
      cprintf("STERN'S SERIES\n\n");
   gotoxy(2,5);
   cprintf("VALUE N: ");
   cin>>n;
   cout<<endl;
   for(int i=1;i<=n;i++)
        {   ans=0;
          stern(i);
          gotoxy(2,wherey());
                cprintf("%d/",ans);
                ans=0;
          stern(i+1);
                 cprintf("%d\n",ans);
       }
                  getch();
                 }
```

7) Experiments for Implementation of Classifiers

The key design decisions for the neural networks used in the classification are the architecture and the training process. The adequate functioning of neural networks depends on the sizes of the training and the testing set. To comparatively evaluate the performance of the classifiers, all the classifiers presented in this paper were trained by the same training data set and tested with the evaluation data set. In order to compare the performance of the different classifiers for the same classification problem, in addition to CANFIS, we also implemented the MLPNN, PNN, PCA, SVM, and SOM. We performed different experiments during implementation of the classifiers and the number of hidden neurons was determined by taking into consideration the classification accuracies. In the hidden layers and the output layers, the activation function used was the sigmoidal function. The sigmoidal function with the range between zero and one introduces two important properties. First, the sigmoid is nonlinear, allowing the network to perform complex mappings of input to output vector spaces, and secondly, it is continuous and differentiable, which allows the gradient of the error to be used in updating the weights. The training algorithm for different classifiers is based on adjusting all the weights between the neurons to minimize the mean square error of all the training patterns. The Levenberg-Marquardt algorithm is used for training the classifiers as it combines the best features of Gauss-Newton technique and steepest-descent algorithm and does not suffer from slow convergence [19].

3. DIAGNOSTIC SYSTEM USING CANFIS

CANFIS combines Classification and Regression Trees (CART) and the Neuro-Fuzzy Inference System (NFIS) in a two step procedure. CART is a tree-based algorithm used to optimize the process of selecting relevant predictors from a large pool of potential predictors. Using the selected predictors, NFIS builds a model for continuous output of the predictand. In this sense, CANFIS migrates various degrees of neuro-fuzzy spectrum between the two extremes: a completely understandable FIS and a black-box NN, which is at the other end of interpretability spectrum. Neuro-fuzzy models can be characterized by neuro-fuzzy spectrum, in light of linguistic transparency and input-output mapping precision.

CANFIS powerful capability stems from pattern-dependent weights between consequent layer and fuzzy association layer. Membership values correspond to those dynamically changeable weights that depend on input patterns. CANFIS bears a close relationship to the computational paradigms of radial basis function (RBF) networks and modular networks.

The fundamental component for CANFIS is a fuzzy neuron that applies membership functions (MFs) to the inputs. Two membership functions commonly used are general Bell and Gaussian. The network also contains a

normalization axon to expand the output into a range of 0 to 1. The second major component in this type of CANFIS is a modular network that applies functional rules to the inputs. The number of modular networks matches the number of network outputs, and the number of processing elements in each network corresponds to the number of MFs. CANFIS also has a combiner axon that applies the MFs outputs to the modular network outputs. Finally, the combined outputs are channeled through a final output layer and the error is back-propagated to both the MFs and the modular networks.

The function of each layer is described as follows. Each node in Layer 1 is the membership grade of a fuzzy set (A, B, C, or D) and specifies the degree to which the given input belongs to one of the fuzzy sets. The fuzzy sets are defined by three membership functions. Layer 2 receives input in the form of the product of all output pairs from the first layer. The third layer has two components. The upper component applies the membership functions to each of the inputs, while the lower component is a representation of the modular network that computes, for each output, the sum of all the firing strengths. The fourth layer calculates the weight normalization of the output of the two components from the third layer and produces the final output of the network. The architecture of CANFIS network is presented in **Figure 10**.

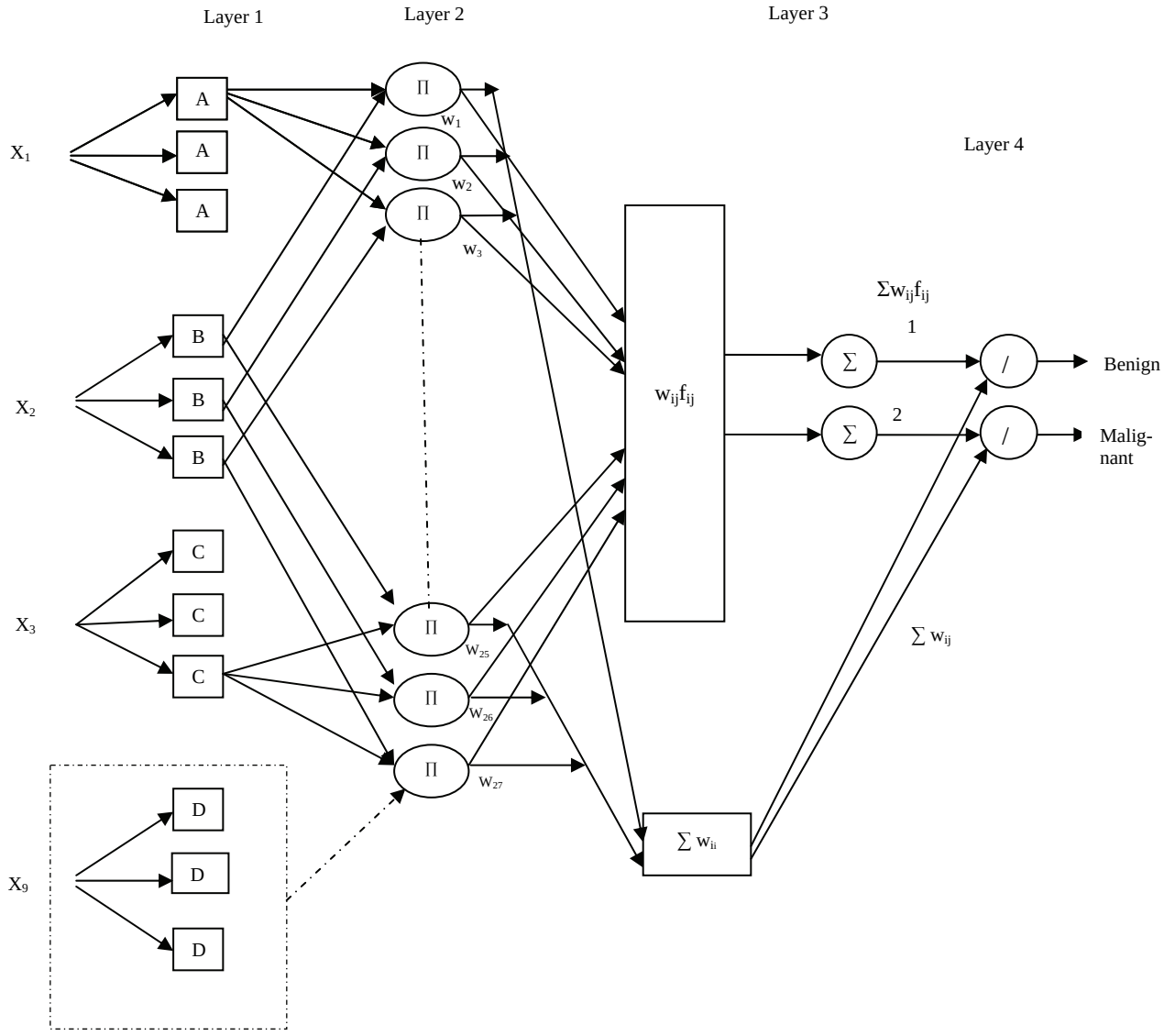

Figure 10. CANFIS network topology.

One disadvantage of CANFIS is that it should not be used to predict values outside the extreme contained in the learning database. This limitation becomes less relevant with increased database size. Another disadvantage is that sufficient data base volume is required to build the model. As such it is not capable of direct prediction for sites which have a lack of archived observations.

4. EXPERIMENTAL RESULTS

The simulations were realized by using MATLAB 6.0 Neural Network Toolbox and Neurosolution software. Six different neural network structure, Multi layer perceptron, Probabilistic neural network, Principal component analysis, Radial basis function, Support vector machine and Self organizing map neural network were applied to WBCD database to show the performance of these neural networks on breast cancer data. To evaluate the correctness of the proposed system, PPV (positive predicted value) was computed in each case.

PPV is computed as:

$$PPV = \frac{Correct\ results}{All\ results} \times 100$$

Table 3 gives the recommended inputs by each input recommenders, Decision tree and Correlation coefficients.

Table 4 gives the results citied in the literature on WBCD dataset and **Table 5** gives our results. **Figure 11** shows the CANFIS networks learning curve using Neuro Solution software on WBCD database. **Figure 12** shows the output vs. desired plot for CANFIS network on WBCD dataset and the obtained Mean Square Error is only 0.020588.

Table 3. Recommended Inputs by each input recommender.

Decision Tree input	X_6	X_3	X_7	X_8
Correlation coefficient input	X_2	X_7	X_3	X_6

Table 4. Experimental results of previous work on WBCD dataset.

Experiment	PPV (percent)	Reference
Fuzzy-Genetic	97.07	[2]
ILFN	97.23	[7]
Fuzzy	96.71	[7]
ILFN &Fuzzy	98.13	[7]
SANFIS	96.07~96.3	[4]
NNs	97.95	[24]

Table 5. Experimental results of our works on WBCD dataset.

Experiment	All Inputs PPV (%)	Decision Tree PPV (%)	Correlation Coefficient PPV (%)
CANFIS	98.82	98.53	97.94
PCA	98.53	98.24	97.65
SOM	97.94	96.77	97.94
SVM	97.65	95.30	95.89
PNN	97.06	97.65	97.65
MLP	97.65	98.24	97.36

The reduced input dataset shows almost the same performances or better performances with the same learning iteration number and shows better/similar performance against the results of previous works. Since the result derived by the reduced input dataset shows better performance and it has significantly higher advantage in computation, it would be a better method to be implemented in real situations. Therefore, the proposed methods-combined algorithm with dominant input recommenders, can be appropriate methods of inference system for the problem of breast cancer diagnosis.

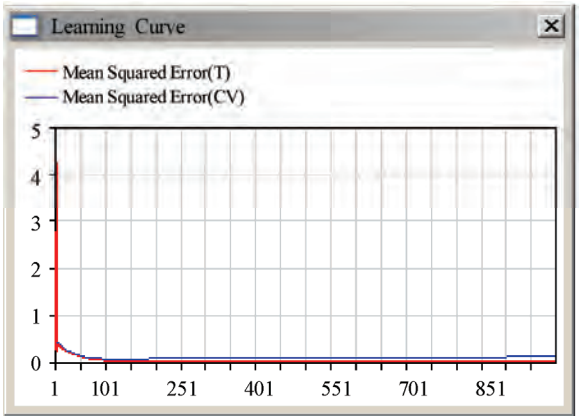

Figure 11. CANFIS network learning curve on WBCD database.

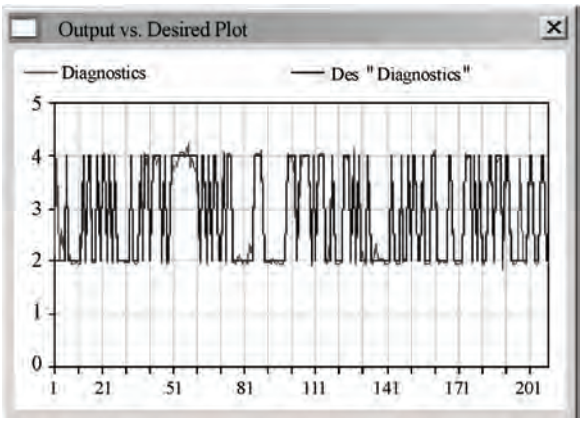

Figure 12. Output vs desired plot for CANFIS on WBCD database.

5. DISCUSSION

Based on the results of the present paper, we would like to highlight the following.

1) The high classification accuracies of CANFIS with full data give insights into the nine measures of the WBCD database. This classification accuracy slightly decreases with input recommenders.

2) The classification accuracy of PCA, SOM, PNN and MLP does not change much even after decreasing the inputs with input recommenders.

3) When we initialized the weight of neural network using stern series instead of zero as we usually do, the speed of training was noted to increase.

4) During SVM training, most of the computational effort is spent on solving the quadratic programming problem in order to find the support vectors. The SVM maps the features to higher dimensional space and then uses an optimal hyperplane in the mapped space. This implies that though the original features carry adequate information for good classification, mapping to a higher dimensional feature space could potentially provide better discriminatory clues that are not present in the original feature space. The selection of suitable kernel function appears to be a trial-and-error process. One would not know the suitability of a kernel function and performance of the SVM until one has tried and tested with representative data. For training the SVMs with RBF-kernel functions, one has to predetermine the σ values. The optimal or near optimal σ values can only be ascertained after trying out several, or even many values.

5) The pattern layer of a PNN often consists of all training samples of which many could be redundant. Including redundant samples can potentially lead to a large network structure, which, in turn, induces two problems. First, it would result in a higher computational overhead simply because the amount of computation necessary to classify an unknown pattern is proportional to the size of the network. Second, a consequence of a large network structure is that the classifier tends to be oversensitive to the training data and is likely to exhibit poor generalization capabilities to the unseen data. However, the smoothing parameter also plays a crucial role in the PNN classifier, and an appropriate smoothing parameter is often data dependent.

6. CONCLUSIONS

In this work, the performance of various neural network structures was investigated for breast cancer diagnosis problem. Initializing Neural network with Stern series was proposed to speed up training. CANFIS is the best trade off between neural networks and fuzzy logic providing smoothness and adaptability. It also gives better classification accuracy in terms of PPV [**Table 5**] than all other neural classifiers analyzed. The performance of the SVM was not as high as the SOM and PCA. This may be attributed to several factors including the training algorithms, estimation of the network parameters, and the scattered and mixed nature of the features. The results of the present paper demonstrated that the CANFIS and PCA can be used in the classification of the WBCD data by taking into consideration the misclassification rates. This work also indicates that CANFIS can be effectively used for breast cancer diagnosis to help oncologists.

REFERENCES

[1] Ioanna, C., Evalgelos, D., and George, K., (2000) Fast detection of masses in computer aided mammography, IEEE Signal Processing Magazine: January, 54–64.

[2] Pena-Reyes, C. A. and Sipper, M., (91999) A fuzzy-genetic approach to breast cancer diagnosis, Artificial Intelligence in Medicine, 131–155.

[3] Pena-Reyes, C. A. and Sipper, M., (1998) Evolving fuzzy rules for breast cancer diagnosis, In Proceedings of 1998 International Symposium on Nonlinear Theory and Applications.

[4] Wang, J.-S. and Lee, G. C. S., (2002) Self-adaptive neuron-fuzzy inference systems for classification applications, IEEE Transactions on Fuzzy Systems.

[5] Arulampalam, G. and Bouzerdoum, A., (2001) Application of shunting inhibitory artificial neural networks to medical diagnosis, Seventh Australian and New Zealand Intelligent Information Systems Conference.

[6] Land, W. H., Jr., Masters, T., and Lo, J. Y., (2000) Application of a new evolutionary programming/adaptive boosting hybrid to breast cancer diagnosis, IEEE Congress on Evolutionary Computation Proceedings.

[7] Meesad, P. and Yen, G. G., (2003) Combined numerical and linguistic knowledge representation and its application to medical diagnosis, IEEE Transactions on Systems, Man, and Cybernatics.

[8] Jang, J.-S. R., (1993) ANFIS: Adaptive-network based fuzzy inference system., IEEE Trans. on System, Man and Cybernetics, **23(3)**.

[9] Jang, J. R. and Sun, C. T. (1995) Neuro-fuzzy modeling and control, Proceedings of the IEEE.

[10] Freund, Y. and Schapire, R. E., (1996) Experiments with a new boosting algorithm, Machine Learning: Proceedings of the Thirteenth International Conference.

[11] Schapire, R. E., (1999) Theoretical views of boosting and applications, Proceedings of Algorithmic Learning Theory.

[12] Sebri, A., Malek, J., and Tourki, R., (2007) Automated breast cancer diagonosis based on GVF-snake segmentation, wavelet features extraction and neural network classification, J. Computer Science, **3(8)**, 600–607.

[13] Goldberg, D., (1989) Genetic algorithm in search, optimization, and machine learning, Addison-Wesley.

[14] John, G. H., Kohavi, R., and Pfleger, K., (1994) Irrelevant features and the subset selection problem, Machine Learning: Proceedings of the Eleventh International Conference.

[15] Mangasarian, O. L., Street, W. N., and Wolberg, W. H., (1994) Breast cancer diagnosis and prognosis via linear programming, Mathematical Programming Technical Report 9410, University of Wisconsin.
[16] Song, H.-J., Lee, S.-G., and Park, G.-T., (2005) A Methodology of computer aided diagnostic system on breast cancer, Proceedings of the IEEE Conference on Control Applications Toronto, Canada.
[17] Haykin, S., (1994) Neural networks: A comprehensive foundation, NewYork: Macmillan.
[18] Chaudhuri, B. B. and Bhattacharya, U., (2000) Efficient training and improved performance of multilayer perceptron in pattern classification, Neurocomputing, **34**, 11–27.
[19] Hagan, M. T. and Menhaj, M. B., (1994) Training feedforward networks with the Marquardt algorithm, IEEE Trans. Neural Netw., **5(6)**, 989–993.
[20] Specht, D. F., (1990) Probabilistic neural networks, Neural Netw., **3(1)**, 109–118.
[21] Burrascano, P., (1991) Learning vector quantization for the probabilistic neural network, IEEE Trans. Neural Netw., **2(4)**, 458–461.
[22] Vapnik, V., (1995) The Nature of statistical learning theory, NewYork: Springer-Verlag.
[23] Cortes and Vapnik, (1995) Support vector networks, Mach. Learn., **20(3)**, 273–297.
[24] Setiono, R., (2000) Generating concise and accurate classification rules for breast cancer diagnosis, Artificial Intelligence in Medicine.
[25] American Cancer Society Hompage, (20 July 2008) Citing Internet sources URL: http://www.cancer.org.
[26] Johnson, M. B., (2003) Sterns diatomic array applied to fibonacci representations, Fibonacci Quarterly 41, 169–180.

Appendix

AdaBoost	Adaptive Boosting
AP	Accuracy Percentage
CAD	Computer Aided Diagnosis
CANFIS	Coactive Neuro-Fuzzy Inference Systems
CART	Classification and Regression Trees
DT	Decision Tree
FIS	Fuzzy Inference Systems
GA	Genetic Algorithm
MLPNN	Multi Layer Perceptron Neural Network
NFIS	Neuro-Fuzzy Inference System
NN	Neural Network
PCA	Principal Component Analysis
PNN	Probabilistic Neural Network
PPV	Positive Predicted Value
RMS	Root Mean Square
SOM	Self Organizing Map
SVM	Support Vector Machine
WBCD	Wisconsin Breast Cancer Data

J. Biomedical Science and Engineering, 2009, 2, 336-344 **JBiSE**
doi: 10.4236/jbise.2009.25049 Published Online September 2009 (http://www.SciRP.org/journal/jbise/).

Lossless compression of digital mammography using base switching method

Ravi kumar Mulemajalu[1], Shivaprakash Koliwad[2]

[1]Corresponding author, Department of IS&E., KVGCE, Sullia, Karnataka, India; [2]Department of E&C., MCE, Hassan, Karnataka, India.
Email: [1]perajeravi@yahoo.com, [2]spksagar2006@yahoo.co.in

Received 31March 2009; revised 15 May 2009; accepted 25 May 2009.

ABSTRACT

Mammography is a specific type of imaging that uses low-dose x-ray system to examine breasts. This is an efficient means of early detection of breast cancer. Archiving and retaining these data for at least three years is expensive, difficult and requires sophisticated data compression techniques. We propose a lossless compression method that makes use of the smoothness property of the images. In the first step, de-correlation of the given image is done using two efficient predictors. The two residue images are partitioned into non overlapping sub-images of size 4x4. At every instant one of the sub-images is selected and sent for coding. The sub-images with all zero pixels are identified using one bit code. The remaining sub-images are coded by using base switching method. Special techniques are used to save the overhead information. Experimental results indicate an average compression ratio of 6.44 for the selected database.

Keywords: Lossless Compression; Mammography image; Prediction; Storage Space

1. INTRODUCTION

Breast cancer is the most frequent cancer in the women worldwide with 1.05 million new cases every year and represents over 20% of all malignancies among female. In India, 80,000 women were affected by breast cancer in 2002. In the US, alone in 2002, more than 40,000 women died of breast cancer. 98% of women survive breast cancer if the tumor is smaller than 2 cm [1]. One of the effective methods of early diagnosis of this type of cancer is non-palpable, non-invasive mammography. Through mammogram analysis radiologists have a detection rate of 76% to 94%, which is considerably higher than 57% to 70% detection rate for a clinical breast examination [2].

Mammography is a low dose x-ray technique to acquire an image of the breast. Digital image format is required in computer aided diagnosis (CAD) schemes to assist the radiologists in the detection of radiological features that could point to different pathologies. However, the usefulness of the CAD technique mainly depends on two parameters of importance: the spatial and grey level resolutions. They must provide a diagnostic accuracy in digital images equivalent to that of conventional films. Both pixel size and pixel depth are factors that critically affect the visibility of small low contrast objects or signals, which often are relevant information for diagnosis [3]. Therefore, digital image recording systems for medical imaging must provide high spatial resolution and high contrast sensitivity. Due to this, mammography images commonly have a spatial resolution of 1024x1024, 2048x2048 or 4096x4096 and use 16, 12 or 8 bits/pixel. **Figure 1** shows a mammography image of size 1024x1024 which uses 8 bits/pixel.

Nevertheless, this requirement retards the implementation of digital technologies due to the increment in processing and transmission time, storage capacity and cost that good digital image quality implies. A typical mammogram digitized at a resolution of 4000x5000 pixels with 50-µm spot size and 12 bits results in approximately 40 Mb of digital data. Processing or transmission time of such digital images could be quite long. An efficient data compression scheme to reduce the digital data is needed.

The goal of the image compression techniques is to represent an image with as few bits as possible in such a way that the original image can be reconstructed from this representation without or with minimum error or distortion. Basically image compression techniques have been classified into two categories namely lossy and lossless methods. Lossy compression methods cannot achieve exact recovery of the original image, but achieves significant compression ratio. Lossless compression techniques, as their name implies, involve no loss of information. The original data can be recovered

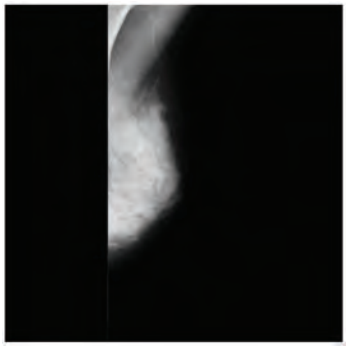

Figure 1. A Mammography image of size 1024x1024 which uses 8 bits/pixel.

exactly from the compressed data. In medical applications, lossless coding methods are required since loss of any information is usually unacceptable [4]. Performance of the lossless compression techniques can be measured in terms of their compression ratio, bits per pixels required in the compressed image and the time for encoding and decoding. On the other hand, since the lossy compression techniques discard some information, performance measure includes the mean square error and peak signal to noise ratio (PSNR) in addition to the measures used for the lossless compression.

Lossless image compression systems typically function in two stages [5]. In the first stage, two-dimensional spatial redundancies are removed by using an image model which can range from a relatively simple causal prediction used in the JPEG-LS [6,7] standard to a more complicated multi-scale segmentation based scheme. In the second stage, the two-dimensional de-correlated residual which is obtained from the first stage, along with any parameters used to generate the residual is coded with a one-dimensional entropy coder such as the Huffman or the Arithmetic coder.

Existing lossless image compression algorithms can be broadly classified into two kinds: Those based on prediction and those that are transform based. The predictive coding system consists of a prediction that at each pixel of the input image generates the anticipated value of that pixel based on some of the past pixels and the prediction error is entropy coded. Various local, global and adaptive methods can be used to generate prediction. In most cases, however the prediction is formed by a linear combination of some previous pixels. The variance of the prediction error is much smaller than the variance of the gray levels in the original image. Moreover, the first order estimate of the entropy of the error image is much smaller than the corresponding estimate for the original image. Thus higher compression ratio can be achieved by entropy coding the error image. The past pixels used in the prediction are collectively referred to as a context. The popular JPEG-LS standard uses the prediction based coding technique [8]. Transform based algorithms, on the other hand, are often used to produce a hierarchical or multi-resolution representation of an image and work in the frequency domain. The popular JPEG-2000 standard uses the transform based coding technique [9].

Several techniques have been proposed for the lossless compression of the digital Mammography. A. Neekabadi *et al.* [10] uses chronological sifting of prediction errors and coding the errors using arithmetic coding. For the 50 MIAS (Mammography Image Analysis Society) images, CSPE gives better average compression ratio than JPEG-LS and JPEG-2000. Xiaoli Li *et al.* [11] uses grammar codes in that the original image is first transformed into a context free grammar from which the original data sequence can be fully reconstructed by performing parallel and recursive substitutions and then using an arithmetic coding algorithm to compress the context free grammar. Compression ratio achieved is promising but it involves more complicated processing and large computation time. Delaunay triangulation method [12] is another approach. It uses geometric predictor based on irregular sampling and the Delaunay triangulation. The difference between the original and the predicted is calculated and coded using the JPEG-LS approach. The method offers lower bit rate than the JPEG-LS, JPEG-lossless, JPEG2000 and PNG. A limitation is the slow execution time. Lossless JPEG2000 and JPEG-LS are considered as the best methods for the mammography images. Lossless JPEG 2000 methods are preferred due to the wide variety of features, but are suffered from a slightly longer encoding and decoding time [13].

Recently, there have been a few instances of using segmentation for lossless compression. Shen and Rangayyan [14] proposed a simple region growing scheme which generates an adaptive scanning pattern. A difference image is then computed and coded using the JBIG compression scheme. Higher compression ratio is possible with such a scheme for the high resolution medical images. But the application of the same scheme to normal images did not result in significant performance improvement. Another scheme reported in literature involves using a variable block size segmentation(VBSS) to obtain a context sensitive encoding of wavelet coefficients, the residual being coded using a Huffman or Arithmetic coder [15,16]. The performance of the method is comparable to that of the lossless JPEG standard. Mar wan Y. *et al.* [17] proposed fixed block based (FBB) lossless compression methods for the digital mammography. The algorithm codes blocks of pixels within the image that contain the same intensity value, thus reducing the size of the image substantially while encoding the image at the same time. FBB method alone gives small compression ratio but when used in conjunction with LZW it provides better compression

ratio.

We propose a method based on Base switching (BS). Trees-Juen Chuang *et al.* [18] have used Base-switching method to compress the general images. [19] And [20] also have used the same concept for the compression of digital images. The algorithm segments the image into non overlapping fixed blocks of size n×n and codes the pixels of the blocks based on the amount of smoothness. In the proposed work we have optimized the original BS method for the compression of mammography images. Specific characteristics of mammography images are well suited for the proposed method. These characteristics include low number of edges and vast smooth regions.

The organization of the paper is as follows. Section 2 describes the basic Base Switching (BS) method. The proposed algorithm is given in Section 3. Experimental results and conclusion are given in Sections 4 and 5 respectively.

2. BASE-SWITCHING ALGORITHM

The BS method divides the original image (gray-level data) into non-overlapping sub-images of size $n \times n$. Given a $n \times n$ sub-image A, whose N gray values are $g_0, g_1, \ldots g_{N-1}$, define the "minimum" m, "base" b and the "modified sub-image "A^I, whose N gray values are $g_0^I, g_1^I, \ldots g_{N-1}^I$, by

$$m = \min g_i \tag{1}$$

$$b = \max g_i - \min g_i + 1 \tag{2}$$

$$A^I{}_{n\times n} = A_{n\times n} - m \times I_{n\times n} \tag{3}$$

$$\text{Also, } g_i{}^I = g_i - m \quad \text{for all i=0 to N -1} \tag{4}$$

where N= $n \times n$ and each of the elements of I is 1. The value of 'b' is related to smoothness of the sub-image where smoothness is measured as the difference between maximum and minimum pixel values in the sub-image.

The number of bits required to code the gray values g_i^I is,

$$B = \lceil \log_2 b \rceil \tag{5}$$

Then, total bits required for the whole sub-image is,

$$Z_A = N \times \lceil \log_2 b \rceil \text{ bits.} \tag{6}$$

For example, for the sub-image of **Figure 2**, n=4, N=16, m=95& b=9. Modified sub-image of **Figure 3** is obtained by subtracting 95 from every gray values of A.

For the sub-image in **Figure 3**, since B=4, Z_A =64 bits.

95	96	97	99
96	97	103	103
97	96	96	103
96	96	97	103

Figure 2. A sub-image A with n=4, N=16, m=95, b=9& B=4.

0	1	2	4
1	2	8	8
2	1	1	8
1	1	2	8

Figure 3. Modified sub-image A^I.

In order to reconstruct A, value of B and m should be known. Therefore encoded bit stream consists of m, B and A^I coded using B bits. In the computation of B, If b is not an integer power of 2, $\log_2(b)$ is rounded to the next higher integer. Thus, in such cases, higher number of bits is used than absolutely required. BS method uses the following concept to exploit this redundancy.

$$\text{It is found that, min } g_i^I = 0 \text{ and max } g_i^I = b-1 \tag{7}$$

The image $A^I = (g_0^I, g_1^I, \ldots, g_{N-1}^I)$ can be treated as an N digit number $(g_0^I g_1^I \ldots g_{N-1}^I)_b$ in the base b number system. An integer value function f can be defined such that f (A^I,b)= decimal integer equivalent to the base-b number.

$$= \sum_{i=0}^{N-1} g_i{}^I \times b^i \tag{8}$$

$$= g_0^I + g_1^I \times b + \cdots\cdots + g_{N-1}^I \times b^{N-1} \tag{9}$$

Then, number of bits required to store the integer f (A^I, b) is

$$Z_B = \left\lceil \log_2 b^N \right\rceil \tag{10}$$

Reconstruction of A^I is done by switching the binary (base 2) number to a base b number. Therefore, reconstruction of A needs the value of m and b. The format of representation of a sub-image is as shown below.

Min. value in the n× n block. (8 bits)	Value of b For the n× n block (8 bits)	f (A^I, b) coded using Z_B bits (Z_B bits)

For the example of **Figure 3**, b=9 and therefore Z_B=51 bits. It is easy to prove that always $Z_B \le Z_A$. We know that, Maximum value of f (A^I, b) = b^N-1.

Total number of bits required to represent f in binary is

$$Z_B = \left\lceil \log_2 b^N \right\rceil = \lceil N \times \log_2 b \rceil \tag{11}$$

Always,

$$\lceil N \times \log_2 b \rceil \le N \times \lceil \log_2 b \rceil \tag{12}$$

$$\text{This verifies that } Z_B \le Z_A \tag{13}$$

2.1. Formats Used for Encoding

Original BS algorithm uses a block size of 3x3 for seg-

mentation. There are three formats used by the original algorithm for encoding the sub-images.

Format1:

If b $\in$ {1,2 …,11}, then the coding format is

c	b	m	Binary equivalent of f (A^I, b)
1 bit	7 bits	8 bits	Z_B bits

This format is economical when b<2 [3,4]

Format2:

If b $\in$ (12, 13,…., 128}, then the coding format is

c	b	m(8 bits)	P(min, max) (7 bits)	Binary equivalent of $(g^I_i for 0 \le i \le 8, i \ne i_{min}, i \ne i_{max})_b$ ($\lceil \log_2 b^7 \rceil$ bits)
(1 bit)	(7 bits)			

Here P(min,max) is a pair of two 3 bit numbers indicating the position of minimum and maximum values. If b>11, writing the positions of minimum and maximum values is economical than coding them.

Format 3:

If b $\in$ (129, 130,…., 256}, then the coding format is

c	The original nine gray values: $g_0, g_1, \ldots g_8$
(1 bit)	(72 bits)

Here, c stands for the category bit. If c is 0, then the block is encoded using Formats 1 or 2; otherwise Format 3 is used.

2.2. Hierarchical Use of BS Technique

The encoded result of Subsection 2.1 can be compressed further in a hierarchical manner. We can imagine that there is a so-called "base-image", whose gray values are b0, b1, b2, …, b255; then, since it is a kind of image (except that each value is a base value of a sub-image rather than a gray value of a pixel), we can use the same BS technique to compress these base values. The details are omitted. Besides *b*, the minimal value *m* of each block can also be grouped and compressed similarly. We can repeat the same procedure to encode *b* and *m* values further.

3. PROPOSED METHOD

In the proposed method, we made following modifications to the basic BS method.

1) Prediction
2) Increasing the block size from 3x3 to 4x4
3) All-zero block removal
4) Coding the minimum value and base value

3.1. Prediction

After reviewing the BS method, it is found that number of bits required for a sub-image is decided by the value of base 'b'. If 'b' is reduced, the number of bits required for a sub-image is also reduced. In the proposed method, prediction is used to reduce the value of 'b' significantly. A predictor generates at each pixel of the input image the anticipated value of that pixel based on some of the past inputs. The output of the predictor is then rounded to the nearest integer, denoted $\hat{x}_n$ and used to form the difference or prediction error

$$e_n = x_n - \hat{x}_n \tag{14}$$

This prediction error is coded by the proposed entropy coder. The decoder reconstructs e_n from received code words and perform the reverse operation

$$x_n = e_n + \hat{x}_n \tag{15}$$

The quality of the prediction for each pixel directly affects how efficiently the prediction error can be encoded. The better this prediction is less is the information that must be carried by the prediction error signal. This, in turn, leads to fewer bits. One way to improve the prediction used for each pixel is to make a number of predictions then chose the one which comes closest to the actual value [21]. This method also called as switched prediction has the major disadvantage that the choice of prediction for each pixel must be sent as overhead information. The proposed prediction scheme uses two predictors and one of them is chosen for every block of pixels of size 4x4. Thus, the choice of prediction is to be made only once for the entire 4x4 block. This reduces the amount of overhead. The two predictions are given in **Eq.16 and 17**, in that, Pr_1 is the popular MED predictor used in JPEG-LS standard and Pr_2 is the one used by [5] for the compression of mammography images.

For the entire pixels of a block of size 4×4, one of the two predictions is chosen depending on the smoothness property of the predicted blocks. Here, smoothness is measured as the difference between maximum and minimum pixel values in the block. The predictor that gives the lowest difference value will be selected for that block. The advantage here is that the overhead required for each block is only one bit.

$$Pr_1 \begin{cases} = \min(A, B) \text{ if } C \ge \max(A, B). \\ = \max(A, B) \text{ if } C <= \min(A, B). \\ = A + B - C \quad \text{otherwise.} \end{cases} \tag{16}$$

$$Pr_2 = \lceil (A \times 0.1 + B \times 0.3 + C \times 0.1 + D \times 0.2 + E \times 0.2 + F \times 0.1) \rceil \tag{17}$$

Here, A, B, C, D, E and F are the neighbors of pixel involved in prediction as depicted in **Figure 4**.

The proposed switched prediction is described in the equation form in 18 where d1 and d2 are the differ-

	C	B	E	F
	A	X		
	D			

Figure 4. Neighbors of pixel involved in prediction.

ences between maximum and minimum values for the two blocks obtained using the two predictors Pr_1 and Pr_2 respectively.

$$Pr = Pr_1 \text{ if } d1<d2 \quad (18)$$
$$= Pr_2 \text{ otherwise}$$

Figure 5 illustrates the prediction technique. It shows two error images which are obtained by using two predictors Pr_1 and Pr_2 respectively. The BS algorithm divides them into 4x4 sub-images and computes the difference between maximum and minimum pixel values for all the four sub-images. For the first sub-image, difference 'd1' is 6 and 'd2' is 8, where d1 and d2 are the differences of the sub-images corresponding to the predictors Pr_1 and Pr_2 respectively. Now, since d1<d2, the prediction Pr considers 4x4 sub-image of predictor Pr_1 for further processing. This procedure is repeated for all the other sub-images. The resulting error image is shown in **Figure 6**. We use a separate file *predict* to store the choice of predictor made at every sub-image.

Error Image obtained using prediction p_{r_1}

-1	0	2	0	-2	3	2	1
0	3	3	0	2	2	2	1
2	3	4	0	2	0	1	4
0	-2	3	-1	0	5	-2	-3
0	0	0	0	2	3	-1	0
-1	1	1	1	1	3	-1	0
0	2	1	0	0	3	2	0
-1	1	1	2	2	2	2	1

Error Image obtained using prediction p_{r_2}

-1	0	2	0	-2	3	2	2
0	3	3	0	2	2	2	1
2	3	4	0	2	0	1	4
0	-4	3	-1	0	3	-2	-3
0	0	0	0	2	3	-1	0
-1	1	1	1	1	3	-1	0
0	4	1	0	0	6	2	0
-1	1	1	2	2	2	2	1

Figure 5. Prediction technique.

3.2. Increasing the Block Size from 3x3 to 4x4

It is obvious that smaller block size gives lower *b* value but at the cost of increased overhead for the total image. The basic BST algorithm uses a block size of 3x3 to achieve optimum balance between amount of overhead and compression efficiency. Since the prediction increases smoothness, a larger block size can be chosen without significant difference in the smoothness. Certainly, this will improve the compression ratio. We have tested the proposed algorithm using different block sizes and found that block size of 4x4 gives the best result. This is supported by **Table 1** giving the average compression ratios obtained for the 50 mammography images for various block sizes.

3.3. All-Zero Block Removal

Mammography images are highly correlated so that pixels inside most of the sub-images are same. During prediction and subtraction they have the highest chance of becoming zeros. If a sub-image of the error image has all its pixel values as zero, then that is marked as an all-zero block by storing a bit 1 in the encoding format. For each of the remaining sub-images, bit 0 is stored in the encoding format and is retained for further processing. Mammography images of MIAS data-set shows very large amount of all-zero blocks. This is supported by **Table 2** showing average number of all-zero blocks present in the 50 mammography images of the MIAS dataset.

For these images, total bits required for marking the presence or absence of all-zero blocks is 65536, since

-1	0	2	0	-2	3	2	2
0	3	3	0	2	2	2	1
2	3	4	0	2	0	1	4
0	-2	3	-1	0	3	-2	-3
0	0	0	0	2	3	-1	0
-1	1	1	1	1	3	-1	0
0	2	1	0	0	3	2	0
-1	1	1	2	2	2	2	1

Figure 6. Resulting error image.

Table 1. Average compression ratio obtained for various block sizes.

3x3	4x4	4x8	8x4	8x8
6.18	**6.44**	6.15	6.18	5.92

Table 2. Average number of all-zero blocks present in the 50 MIAS images.

Image size	No. of blocks of size 4× 4	Average no. of all-zero blocks	Remaining blocks
1024× 1024	65 536	32 282	33 254

total sub-images are 65536. The error image will have both negative and positive pixel values since the prediction has changed the range of the pixel values from [0, 255] to [-255, 255]. Therefore, 9 bits are required to record the pixel values. The approximate average compression ratio obtained by all-zero block removal for the 50 MIAS images considered in **Table 2** can be estimated by the following formula.

$$CR = \frac{1024 \times 1024 \times 8}{65536 + \text{remaining blocks} \times \text{pixels per block} \times \text{bits per pixel used for coding}}$$
$$= \frac{1024 \times 1024 \times 8}{65536 + 33254 \times 16 \times 9} = 1.73.$$

Here the value 65536 indicates the overhead bits required for marking the presence or absence of all-zero blocks. The numerator gives total bits used by the original uncompressed image. This computation clearly shows that removal of all-zero blocks alone gives an approximate compression ratio of 1.73.

3.4. Coding the Minimum Value and the Base Value

The error image will have both negative and positive pixel values. The prediction has changed the range of the minimum value from [0,255] to [-255,255]. Therefore, 9 bits are required to record the minimum value. By studying various images, it is found that minimum values are ranging from -128 to 64. More concentration is observed between -8 to 0. Similarly, base values are concentrated in the range 1 to 15. This statistics is supported by **Table 3** of average number of minimum values and base values for the 50 mammography images.

To exploit this redundancy, we use a typical categorize and coding technique. A four bit code is used to identify the minimum values. Minimum values less than 1 and greater than -15 are given with codes 0 to 14, whereas other minimum values are represented by the code 15 followed by their actual 9 bit values. A scheme similar to this can be used to code the base values also. Base values between 1 and 15 are identified by using 4 bit codes whereas values greater than 15 are identified using the code 15 followed by their actual 9 bit values. The two four bit codes for each of the sub-images are combined to get an 8 bit number. Such 8 bit numbers are stored in a file and Huffman encoded at the end.

3.5. System Overview

As shown in **Figure 7**, we first divide the error image into sub-images of size 4x4.The sub-images are then processed one by one. For each sub-image, we have to determine whether it belongs to all-zero category and if so they are removed. The remaining blocks are retained for further processing.

The two binary files *zero* and *predict* are separately run length encoded, grouped and Huffman encoded. Also, the two four bit files *min* and *base* are combined to form an eight bit file and Huffman encoded.

Table 3. Average number of minimum and base values in 50 MIAS images.

Average No. of minimum and base values	Average no. of minimum values in the range -14 to 0	Average no. of base values in the range 1 to 15
33 253	32 466	33 097

3.6. Decoding a Sub-Image

Following are the decoding steps:

1) The files *min*, *base*, *zero* and *predict* are reconstructed.

2) The decoding algorithm first checks whether the block is an all-zero block or not. If all-zero, then a 4x4 block of zero's is generated.

3) Otherwise, base value and minimum value are first obtained by using the files *min* and *base*. The modified image A^1 is reconstructed as explained in Section 2 and 4x4 error image is obtained by adding min value to it.

4) Type of prediction used is read from the *predict* file. The prediction rule is applied to the 4x4 error image and the original 4x4 sub-image is reconstructed.

4. RESULTS

We evaluated the performance of the proposed scheme using the 50 gray-scale images of the MIAS dataset that include three varieties of images: Normal, Benign and Malignant. The MIAS is a European Society that researches mammograms and supplies over 11 countries with real world clinical data. Films taken from the UK national Breast Screening Program have been digitized to 50 micron pixel edge and representing each pixel with an 8 bit word. MATLAB is the tool used for simulation. All the simulation was conducted on a 1.7GHZ processor and was supplied with the same set of 50 mammography images. Each mammogram has a resolution of 1024x1024 and uses 8 bits/pixel. Results of the proposed method are compared with that of the popular methods. Comparison of Compression results for the 50 MIAS images is shown in **Table 4**. This set includes all the three varieties of images namely normal, benign and malignant.

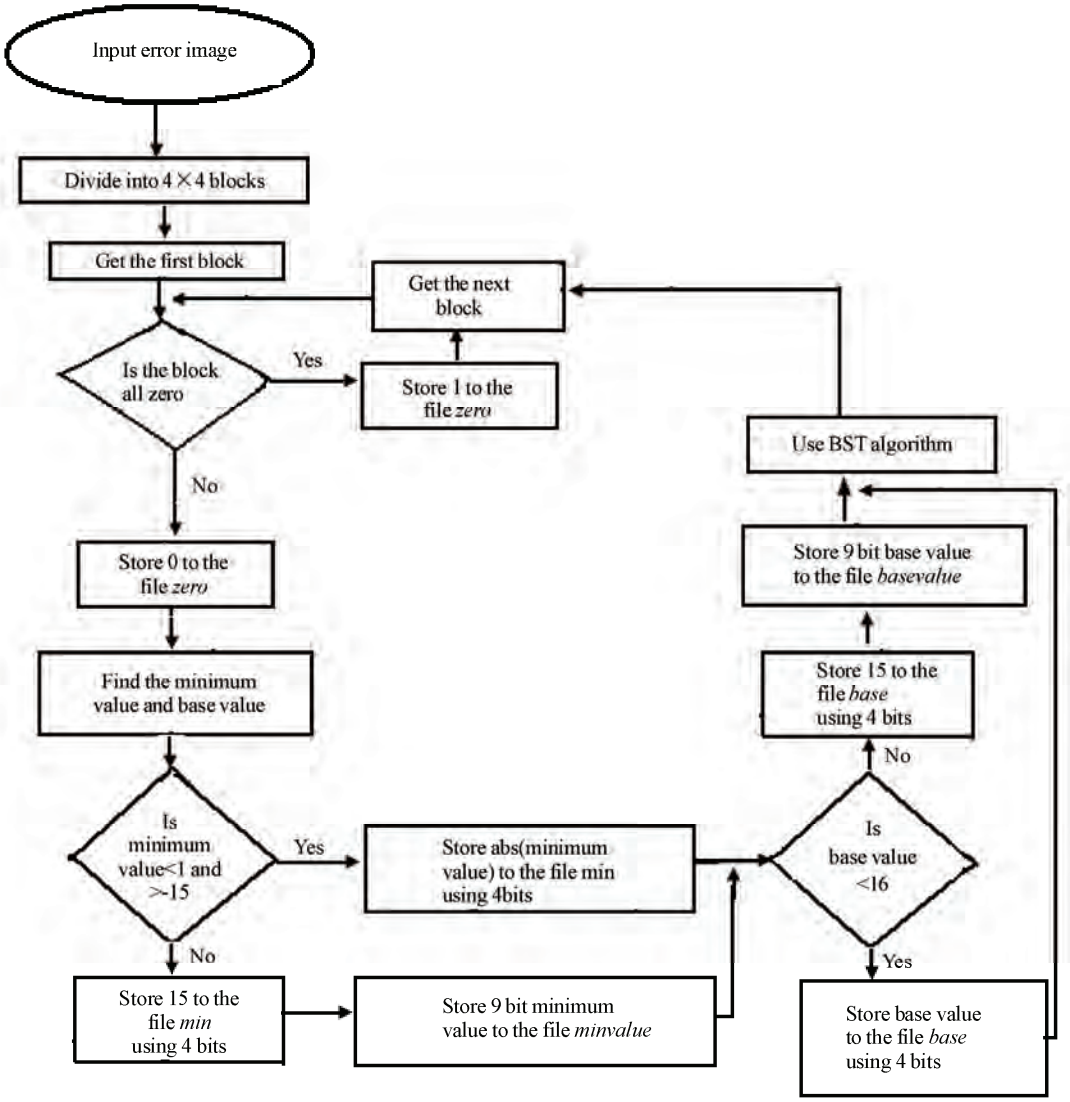

Figure 7. System overview.

Table 4. Comparison of compression results for the 50 MIAS images.

PNG	JBIG	JPEG2000	JPEGLS	PROPOSED
4.30	5.88	6.29	6.39	6.44

Figure 8 and **Figure 9** show the two images mdb040.pgm and mdb025.pgm that gives best and the worst compression ratio respectively.

5. CONCLUSIONS

Several techniques have been used for the lossless compression of mammography images; none of them have used the smoothness property of the images. Our study has shown that there is very large number of zero blocks present in mammography images. We have picked up the concept of Base switching transformation and successfully optimized and applied it in conjunction with other existing compression methods to digitized high resolution mammography images. Comparison with other approaches is given for a set of 50 high resolution digital mammograms comprising of normal, benign and malignant images. Compared with the PNG method, one of the international standards, JBIG, performs better by 36%. Transformation method based JPEG200, another international compression standard, when used in lossless mode, performs slightly better than JBIG by 7%. Whereas, the latest standard for lossless image compression JPEG-LS based on prediction based method, performs best among the four international standards of lossless coding techniques. It gives a compression ratio of 6.39 which is 1.5% better than the JPEG 2000. Finally, for these images, the proposed method performs better than PNG, JBIG, JPEG2000 and JPEG-LS by 50%, 9.5%,

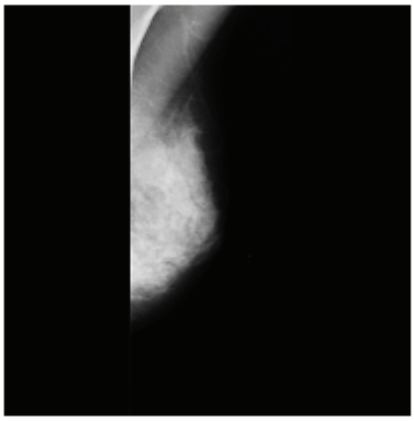

Figure 8. Image mdb040. CR=14.16.

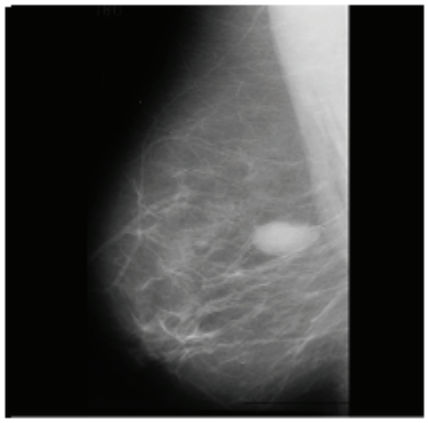

Figure 9. Image mdb025. CR=4.55.

2.4% and approximately 1% respectively. The success of our method is primarily due to its zero block removal procedure, compression of the overheads and the switched prediction used. It should be also noted that the speed of the BST method is very much comparable with the speed of other standard methods as verified by [18]. Further investigation on improvement of the performance of our method is under way, by developing more suitable prediction methods. Motivated by the results obtained here, our next study will carry out the compression of larger database of natural images and medical images obtained by other modalities.

REFERENCES

[1] Saxena, S., Rekhi, B., Bansal, A., Bagya, A., Chintamani, and Murthy, N. S., (2005) Clinico-morphological patterns of breast cancer including family history in a New Delhi Hospital, India—a cross sectional study, World Journal of Surgical Oncology, 1–8.

[2] Cahoon, T. C., Sulton, M. A, and Bezdek, J. C. (2000), Breast cancer detection using image processing techniques, The 9th IEEE International Conference on Fuzzy Systems, **2**, 973–976.

[3] Penedo, M., Pearlman, W. A., Tahoces, P. G., Souto, M., and Vidal, J. J., (2003) Region-based wavelet coding methods for digital mammography, IEEE Transactions on Medical Imaging, **22**, 1288–1296.

[4] Wu, X. L., (1997), Efficient lossless compression of Continuous-tone images via context selection and quantization, IEEE Transaction. on Image Processing, **6**, 656–664.

[5] Ratakonda, K. and Ahuja, N. (2002), Lossless image compression with multi-scale segmentation, IEEE Transactions on Image Processing, **11**, 1228–1237.

[6] Weinberger, M. J., Rissanen, J., and Asps, R., (1996) Application of universal context modeling to lossless compression of gray scale images, IEEE Transaction on Image Processing, **5**, 575–586.

[7] Grecos, C., Jiang, J., and Edirisinghe, E. A., (2001) Two Low cost algorithms for improved edge detection in JPEG-LS, IEEE Transactions on Consumer Electronics, **47**, 466–472.

[8] Weinberger, M. J., Seroussi, G., and Sapiro, G., (2000) The LOCO-I lossless image compression algorithm: Principles and standardization into JPEG-LS, IEEE Transactions on Image processing, **9**, 1309–1324.

[9] Sung, M. M., Kim, H.-J., Kim, E.-K., Kwak, J.-Y., Kyung, J., and Yoo, H.-S., (2002) Clinical evaluation of JPEG 2000 compression for digital mammography, IEEE Transactions on Nuclear Science, **49**, 827–832.

[10] Neekabadi, A., Samavi, S., and Karimi, N., (2007) Lossless compression of mammographic images by chronological sifting of prediction errors, IEEE Pacific Rim Conference on Communications, Computers & Signal Processing, 58–61.

[11] Li, X., Krishnan, S., and Marwan, N. W., (2004) A novel way of lossless compression of digital mammograms using grammar codes, Canadian Conference on Electrical and Computer Engineering, **4**, 2085–2088.

[12] da Silva, L. S. and Scharcanski, J., (2005) A lossless compression approach for mammographic digital images based on the delaunay triangulation, International Conference on Image Processing, **2**, 758–761.

[13] Khademi, A. and Krishnan, S., (2005) Comparison of JPEG2000 and other lossless vompression dchemes for figital mammograms, Proceedings of the IEEE Engineering in Medicine and Biology Conference, 3771–3774.

[14] Shen, L. and Rangayyan, R. M., (1997) A segmentation based lossless image coding method for high-resolution medical image compression, IEEE Transactions on Medical imaging, **16**, 301–307.

[15] Ranganathan, N., Romaniuk, S. G., and Namuduri, K. R., (1995) A lossless image compression algorithm using variable block segmentation, IEEE Transactions on Image Processing, **4**, 1396–1406.

[16] Namuduri, K. R., Ranganathan, N., and Rashedi, H., (1996) SVBS: A high-resolution medical image compression algorithm using slicing with variable block size segmentation, IEEE Proceedings of ICPR, 919–923.

[17] Alsaiegh, M. Y. and Krishnan, S. (2001), Fixed block-based lossless compression of digital mammograms, Canadian Conference on Electrical and Computer Engineering, **2**, 937–942.

[18] Chuang, T.-J. and Lin, J. C., (1998) A new algorithm for lossless still image compression, Pattern Recognition, **31**, 1343–1352.
[19] Chang, C.-C., Hsieh, C.-P., and Hsiao, J.-Y., (2003) A new approach to lossless image compression, Proceedings of ICCT'03, 1734–38.
[20] Ravikumar, M. S., Koliwad, S., and Dwarakish, G. S., (2008) Lossless compression of digital mammography using fixed block segmentation and pixel grouping, Proceedings of IEEE 6th Indian Conference on Computer Vision Graphics and Image Processing, 201–206.
[21] Sayood, K., (2003) Lossless compression handbook, First edition, Academic Press, USA, 207–223.

J. Biomedical Science and Engineering, 2009, 2, 345-358 **JBiSE**
doi: 10.4236/jbise.2009.25050 Published Online September 2009 (http://www.SciRP.org/journal/jbise/).

Review: structure of amyloid fibril in diseases

Arezou Ghahghaei[1*], Nasim Faridi[1]

[1]Department of Biology, Faculty of Science, University of Sistan and Baluchestan, Zahedan, Iran.
Email: Arezou@chem.usb.ac.ir

Received 8 May 2009; revised 13 July 2009; accepted 21 July 2009.

ABSTRACT

Tissue deposition of normally soluble proteins, or their fragments, as insoluble amyloid fibrils causes both acquired and hereditary systemic amyloidoses, which is usually fatal. Amyloid is associated with serious diseases such as Alzheimer's disease, type 2 diabetes, Parkinson's Disease, Huntington's Disease, cancer and the transmissible spongiform encephalopathies. Information concerning the structure and mechanism of formation of fibrils in these diseases is critical for understanding the process of pathology of the amyloidoses and to the development of more effective therapeutic agents that target the underlying disease mechanisms. Structural models have been made using information from a wide variety of techniques, including electron microscopy, X-ray diffraction, solid state NMR, and Congo red and CD spectroscopy. Although each type of amyloidosis is characterised by a specific amyloid fibril protein, the deposits share pathognomonic histochemical properties and the structural morphology of all amyloid fibrils is very similar. In fact, the structural similarity that defines amyloid fibres exists principally at the level of β-sheet folding of the polypeptides within the protofilament, while the different types vary in the supramolecular assembly of their protofilaments.

Keywords: Amyloid; Protofilaments; Aggregation; Neurodegenerative

1. INTRODUCTION

Amyloid fibril formation arises from the slow aggregation of intermediately folded peptide or protein molecules. During this process the protein goes from its native soluble form to insoluble fibril, which is highly β-sheet in character [1,2,3,4]. The aggregation of the amyloid β peptide has been examined in various solvents and conditions and this has led to a model by which a conformational switching occurs from an α-helix or random coil to a β-sheet structure early on the amyloid-forming pathway [5], prior to a nucleation-dependent process leading to the elongation of the fibril. Along this pathway, small oligomeric intermediates and short fibrillar structures (protofibrils) have been observed. In cross-section, the fibril appears to be composed of several subfibrils or protofilaments. Each of these protofilaments is rich in stacked β-sheet structures in which hydrogen bonded β-strands run perpendicular to the fibril's axis, and the backbone hydrogen bonds are parallel to it [6].

The basic process of amyloid formation is known to involve the construction of fibrils from individual polypeptide monomer units held together by noncovalent interactions generated by the formation of intermolecular β-sheets or the correct stacking of intramolecular β-sheet structures [7]. Small polypeptide fragments (as small as five or six residues long) are able to form amyloid fibrils from fully denatured conformations, larger sequences, typically between 80 and 150 residues, appear to require the population of more compact or partially folded states to form amyloids [7]. In a number of systems it has been demonstrated that amyloid fibril formation by proteins *in vitro* is preceded by the formation of metastable, nonfibrillar forms often referred to as protofibrils. These species often have the appearance of spherical beads 2–5 nm in diameter, beaded chains, where the individual beads again have a diameter of 2–5 nm, or annular structures, formed apparently by the circularisation of the beaded chains.

Figure 1 suggests that the various fates awaiting a polypeptide chain, once it has been synthesized in the cell, will depend on the kinetics and thermodynamics of the various equilibria between various possible states [5,8]. In its monomeric state, the protein is believed to fold from its highly disordered unfolded state (*3*) through a partially structured intermediate state (*2*) to a globular native state (*1*) [8,9]. The unfolded and partially folded states can form aggregated species that are frequently disordered. Highly ordered amyloid fibrils can form through a mechanism of nucleation and elongation [8,9,10] showed that the β-domain is the destabilized region of the human lysozyme. This implies that the aggregation process may be initiated by intermolecular rather than intramolecular association [8,10,11].

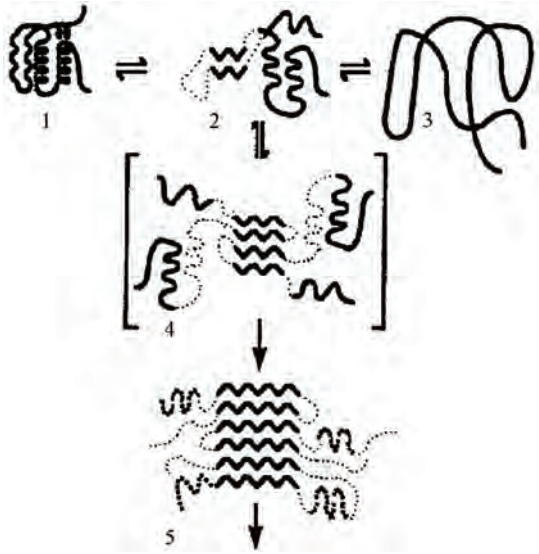

Figure 1. A proposed mechanism for lysozyme amyloid fibril formation [8]. An intermediate structural state form of the protein (2) aggregates through the β domain (4) to commence fibril formation. This intermediate (4) shows a pattern for the development of the fibril.

Negative-stain electron microscopy (EM) showed that the amyloid fibrils associated with the various diseases mostly appear straight, and unbranched, and are 30-120 Å in diameter. They consist of two or more filamentous subunits, which twist around each other with 11.5 nm, 24 β-strand periodicity resulting in a protofilament diameter of 5-6 nm. The amyloid fibril, shown in **Figure 2**, is about 25-35 Å wide and consists of two or three subunit strands helically arranged with a 35-50 Å diameter repeat [12,13,14,15,16,17].

X-ray fibre diffraction showed that all types of fibrils have a common core structure [18,19,20,21]. They consist of a helical array of β-sheets along the length of the fibre. This indicates that the polypeptide chain in fibres are hydrogen-bonded together along their entire length which increases their stability [18,19,20,21]. Cross β-sheets consist of two dominant reflections: a sharp and intense meridional reflection at 4.8 Å, which corresponds to the average distance between the hydrogen-bonded β-strands that comprise β-sheets and a strong and more diffuse reflection on the equator between 9-11 Å arising from the distance between stacked β-sheets, [18,19,20,21]. The X-ray diffraction pattern of PI3-SH3 fibril is shown in **Figure 3** [21]. The fibril contains two reflections: the main reflection, which is intense, occurs at 4.71 Å while the weaker reflections appear at 9.42.

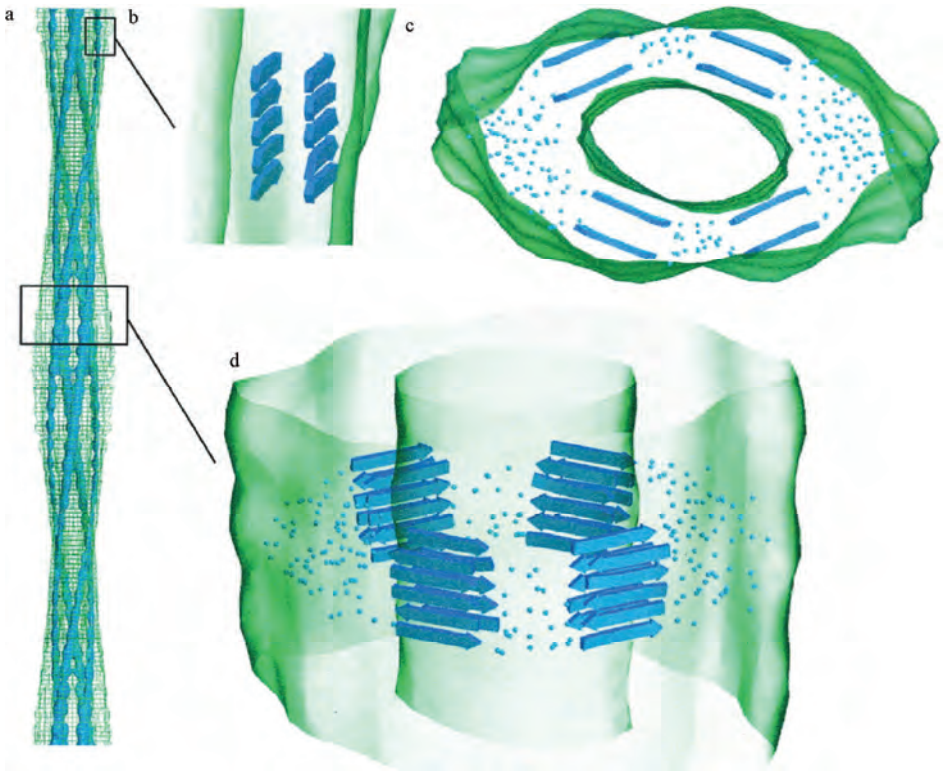

Figure 2. Modeling of an amyloid fibril structure. (a) Overview of the fibril structure showing protofilaments extended in regular helical twists along the length of the fibre (b) Side view of inter-sheet spacing between subprotofilaments of 9-11 Å perpendicular to the axis (c) Cross-section of amyloid fibril (d) Slightly tilted side view of the fibril showing inter-strand spacing of 4.7 Å along the fibre axis [16].

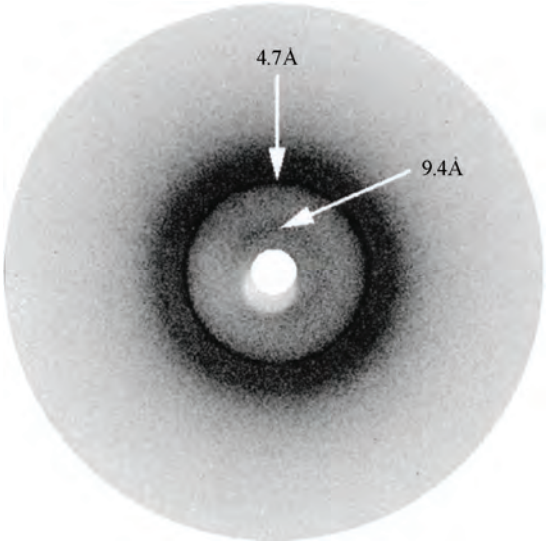

Figure 3. X-ray diffraction pattern of PI3-SH3 fibrils. The meridional (interstrand spacing) and equatorial (intersheet spacing) reflections are indicated at 4.7 Å and 9.4 Å, respectively [21].

In some systems, small amounts of preformed amyloid fibrils, added to the sample to act as seeds, induce the formation of amyloid fibrils more readily if protofibrils are present in the sample rather than non-aggregated or smaller oligomeric species. This observation suggests that, in these cases at least, fibrils can form preferentially from the assembly of protofibrils. Evidence exists, however, that some oligomeric aggregates assembling into chains and rings with "bead-on-string" morphology may be off-pathway species that are not amyloid-competent [22].

The soluble precursors of amyloid deposits do not share any sequence homology or common fold. However, amyloid aggregates have common structural features: 1) they show the same optical behavior (such as birefringence) on binding certain dye molecules like Congo red; 2) they present very similar morphologies (long, unbranched and often twisted fibrillar structures a few nanometers in diameter); and 3) they display the characteristic cross-β X-ray diffraction pattern which indicates that the "core" structure is composed of β-sheets running perpendicular to the fibril axis. [5,23].

2. AMYLOIDOSIS DISEASES

Amyloid formation is associated with a number of diseases e.g. Alzheimer's, Parkinson's, Huntington's, Creutzfeldt-Jakob, Spongiform and other neurodegenerative diseases in which the formation of β-sheet aggregates known as amyloid plaques that, among other features, are extremely resistant to protease action, an indication of close packed clusters. All these diseases are primarily associated with old age [3, 24,25]. It is a general observation that solubility and protease resistance depend on actual secondary structure. A helical and or random coil content has been shown to be coincident with high solubility and protease susceptibility whereas a β-sheet content has been shown to determine poor solubility and resistance to proteolysis [26,27]. The clinical classification of amyloidosis includes primary (de novo), secondary (a complication of a previously existing disorder), familial, and isolated types [28,29]. Each disease is characterized by a particular protein or polypeptide that aggregates in an ordered manner to form insoluble amyloid fibrils [30]. These amyloid fibrils are deposited in the tissues, where they are associated with the pathology of the disease [31].

There are relatively few examples of nonpathological functions. Given that many proteins have the ability to form amyloids. Among the few known functions are the amyloid curli, adhesive appendages of gram-negative bacteria, and yeast regulatory amyloids that may mediate epigenetic diversification. Recently, a natural amyloid has been found to accelerate melanin assembly in melanocytes. Amyloids have been proposed to have a role in the establishment of memory, as well. The discovery of new functions for amyloids would greatly increase our knowledge of their roles in the normal functioning of cells [32]. The role of amyloid β-peptide in the pathogenesis of neurodegenerative disorders is not completely elucidated, but its toxic effect is not necessarily correlated with senile plaque deposition, since it has been shown that the neurotoxic effect of amyloid β-peptide is independent of plaque formation in transgenic mouse models. It has been suggested that neurotoxic effects can be induced by diffusible amyloid β-peptide oligomers or by intraneuronal accumulation of amyloid β-peptide [33].

The function of the majority of proteins is attributable to its unique three dimensional structure [34]. Failure to fold to into its correct structure limits of abrogates the protein's ability to perform the biological roles for which it was produced [35]. Not only does the aggregation of folding intermediates strips the cell of an important resource, the presence of the aggregate themselves can have dire consequence and results in a wide range of disease such as described in the **Table 1**.

Conformational diseases such as those in **Table 1** are associated with proteins that do not attain or maintain their native structure resulting in aggregation and insolubilization [36,37]. The insoluble deposits in this disease form either plaques or fibrillar tangles within tissues and their accumulation ultimately result in cell damage or death [35,38].

Table 1. Representative human disease associated with defective protein folding [113,114,115].

Disease	Protein	Phenotype
Alzheimer's disease	β-Amyloid	Aggregation
Tay-Sachs disease	β-Hexasominidase	Improper trafficking
Cancer	PS3	Misfolding/improper trafficking
Spongiform	Prion Protein	Aggregation
Creutz feldt-jakob diseases	Prion protein	Aggregation
Maifan syndrom	Fibrillin	Misfolding
Parkinson diseases	α-Synuclein	Aggregation
Gaucher's disease	β-Glucosidase	Improper trafficking
Scurvy	Collagen	Misfolding
Huntington's diseases	Huntington	Aggregation
Familial amyloiosis	Transthyretin	Aggregation

3. THE ALZHEIMER'S DISEASE

Alzheimer's disease (AD) is one of the most common neurodegenerative disorders associated with aging, and is characterized by fibrillar deposits of amyloid β (Aβ) peptides in the brain parenchyma and cortical blood vessels [5,37,39]. Patients in Alzheimer's disease often have psychiatric manifestations of disease, such as psychosis (e.g., delusions and hallucinations) and disruptive behaviors (e.g., psychomotor agitation and physical aggression), especially in the later stages of the disease (1). One of the characteristics of brains afflicted with AD is the presence of extracellular structural elements referred to as amyloid plaques. Plaques are, in part, composed of masses of filaments, which are in turn composed of the insoluble form of the Aβ peptide [5,39,40]. These Aβ aggregates may cause neuronal injury directly by acting on synapses, or indirectly by activating microglia and astrocytes and therefore pharmacological interventions have been developed to target the sequential events originating from Aβ synthesis [40,41]. Usually neuritic plaques composed of amyloid β-protein (Aβ) are an early and invariant neuropathological feature of Alzheimer's disease (AD), [41]. Genetic and neuropatho logical studies suggest that the processing of amyloid precursor protein (APP) to yield amyloid β-protein (Aβ), and its subsequent aggregation, play important roles in the pathogenesis of Alzheimer's disease (AD) as the numbers of Aβ plaques and Aβ burden increased over time in the brain with AD and Aβ deposition precedes clinical symptom of AD. The other pathological feature of this disease is intraneural neurofibrillary tangles [42, 43,44].

The Aβ family of peptides is derived by the enzymatic breakdown of the amyloid precursor protein (APP), a 563-770 residue membrane protein expressed in neuronal and non-neuronal tissue [45]. Patients with Down syndrome develop AD because of an extra copy of the amyloid precursor protein (*APP*) gene on chromosome 21 [46]. Amyloid precursor protein (APP) is a ubiquitous membrane glycoprotein encoded by a single gene on chromosome 21 and formed as a cleavage byproduct by three proteases, β-, γ- nd α-secretase [47]. It's cleavege via the α-secretase or the β-secretase pathway, often referred to as the amyloidogenic pathway. When APP is cleaved by α-secretase, it produces a large amino-terminal fragment APPα destined for secretion and a smaller carboxyl-terminal fragment. Further processing of the carboxyl-terminal fragment by γ-secretase produces a 22- to 24-residue fragment termed P3, which may or may not be amyloidogenic. Alternatively, when APP is cleaved by β-secretase it produces a soluble amino-terminal fragment, APPβ, and a carboxyl-terminal fragment containing the Aβ peptide. Cleavage of the carboxyl-terminal fragment by γ-secretase results in the formation of multiple Aβ variants of 40-43 amino acids, which are prone to aggregate. The most abundant forms are 40 and 42 amino acids in length, Aβ 40 and Aβ 42. Both forms are capable of assembling into 60-100 Å diameter β-sheet fibrils that exhibit the characteristic cross-β X-ray fiber diffraction pattern, and yield a red-green birefringence when stained with Congo red [45]. The ratio of Aβ 42 to Aβ 40 is about 1:10. Aβ 42 plays a critical role in the pathogenesis of AD since its aggregative ability and neurotoxicity are much greater than those of Aβ 40. Aβ 42 oligomers initially formed as a seed accelerate the aggregation of Aβ 40 to form the amyloid plaques that eventually lead to the neurodegeneration (amyloid cascade hypothesis) [47].

4. THE STRUCTURE OF AMYLOID IN ALZHEIMER DISEASE

The formation of insoluble Aβ deposits in the brain is a pathological hallmark of AD. If the hypothesis that the neurotoxicity of Aβ is mediated by amyloid fibril formation is correct, inhibition of Aβ fibril formation might

slow progression or prevent the disease. However, more recent studies have shown that fibrils are not the only neurotoxic structures and that Aβ also assembles into soluble forms like small oligomers and protofibrils, which could be responsible for neurotoxicity [48]. Aβ (1-40) and Aβ (1-42) differ structurally by the absence or presence of two C-terminal amino acids [49]. The amino acid sequence of the Aβ 1–42 peptide is D_1AEFRHDSG_9 YEVHHQKLVFFAED_{23}VGSNK_{28}GAIIGLMVGGVV4 $0I_{42}$, where subscripts indicate residue numbers.

The solid state NMR data are consistent with an Aβ1–40 monomer secondary structure composed of a structurally disordered N-terminal region followed by two β-strand segments connected by a "loop" or "bend" segment. Structural model resulted by NMR data support a parallel β-sheet structure in fibrils formed by both the 40 and 42-residue β amyloid peptides (Aβ 1–40,42). Parallel β-sheets have been found by solid state NMR originally in fibrils formed by residues 10–35 of β-amyloid (Aβ 10–35) [23,31,50]. However, antiparallel β-sheets have also been found by solid state NMR in fibrils formed by shorter β-amyloid fragment. In agreement with the NMR experiment MD analysis of various structural models of short β-amyloid fragments, including parallel and antiparallel β-sheet structures suggested a strand-loop-strand structure with parallel β-sheets for Aβ10–35 fibrils [51]. Recent solid state NMR and electron microscopy experiments have shown that Aβ 1–40 can form at least two distinct amyloid fibril structures, with distinct and self-propagating morphologies and molecular-level structural features, dependent on subtle variations in fibril growth conditions. Although all Aβ1–40 fibril structures studied to date contain parallel β-sheets, distinct structures differ in the specific details of side-chain-side-chain contacts and in mass-per length (MPL) values [52].

Thin sections of amyloid fibrils formed from fragments of amyloid β (Aβ), the amyloid fibril protein of Alzheimer's disease, show cross-sections containing five or six protofilaments [23,53,54,55,56]. The protofilaments were over 40Å in diameter and appeared as "beaded" structures with a 200 Å periodicity [53,54,57,58,59].

Electron microscopy studies have shown that amyloid fibrils consist of three to six protofilaments. It is possible that the exposed hydrophobic residues could be involved in helical packing among the protofilaments. It is known, for instance, that side-chain packing plays an important role in stabilizing helical coiled-coil bundles. While the center of pleated β-sheet structure is hydrophobic, the ends of the sheets are somewhat hydrophilic. Ionic interactions and/or hydrogen bond interactions as additional forces stabilizing the cross-β structure have been proposed [60].

Oligomerization of Aβ42 induced by the intermolecular β-sheet at positions 15–21 and 24–32 would confine this radical species in the oligomer, making it possible to damage the cells continuously. However, this oligomer would not lead to the fibrils since the C-terminal β-sheet is intramolecular (**Figure 4(b)**). As shown in **Figure 4(a) and (b)**, the C-terminal residues in Aβ42 play a critical role in its aggregative and neurotoxicity [61] and the intermolecular β-sheet in the C-terminal region of Aβ42 seems to be preferable to long fibrils [47,62]. Aβ (1-42) did not adopt a unique fold, but rather a mixture of rapidly interconverting conformations that were classified into three distinct families. The secondary structure analysis revealed that these conformations were dominated by loops and turns but that some helical structure formed in the C-terminal hydrophobic tail. Experimental studies of full-length Aβ monomers in water (organic solvent mixtures) showed that the monomer structure consists of two α-helical regions connected through an exible turn- or bend-like kink. The model of one helical turn of the twisted pleated β-sheet is composed of 48 monomers of Aβ. Each monomer contains an antiparallel β-sheet. Overall, there are 96 β-strands. Four strands form a unit and 24 units stack together along the fibril axis. If each unit were twisted by 15° relative to its immediate neighbors (above and below) in the same way, 24 units would make a complete helical turn, with the

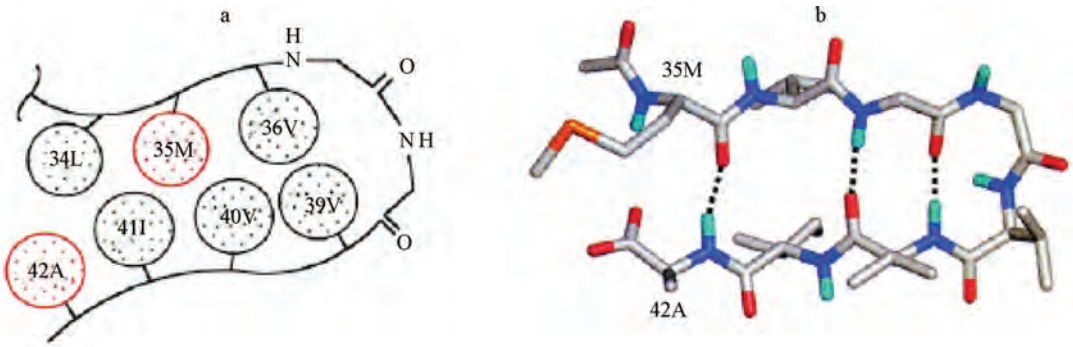

Figure 4. (a) A representation of the hydrophobic residue at the C-terminus of Aβ42 [61]. (b) The intramolecular anti-parallel β-sheet at the C-terminus of Aβ42 [112].

helical axis parallel to the fibril axis. Given that the angle between the two immediate strands from two different monomers was set at 15°, the helical twist formed by the 24 units in the model was actually nearly a complete turn (~350°). Four strands in each unit layer are in an identical orientation, and those between two adjacent (above, below) unit layers are in an antiparallel arrangement (**Figure 5(a) and (b)**). In other words, the unit layers stack in an antiparallel fashion. The distances between the two adjacent strands in different unit layers and that between two strands within a unit layer are ~4.7 and ~9.7 Å, respectively (**Figure 5(c) and (d)**). These distances are consistent with results from x-ray fibril diffraction studies on amyloid fibrils. NMR experiments on Aβ (10-35) monomer structure in an aqueous solution show a collapsed structure with loops, strands, and turns without any significant amount of α-helical or β-strand content. These studies suggest that Aβ monomer structure is very sensitive to external conditions, such as temperature, pH, and solvent. An Aβ (1-40) monomer structure considered with little α-helix or β-strand at low temperatures. As the temperature was increased to physiological, substantial β-sheet content developed. A folded Aβ (1-42) monomer, but not an Aβ (1-40) monomer, possesses a turn at G37-G38 stabilized by a hydrophobic interaction between V36 and V39 [63]. Preliminary cryo-electron microscopy of the amyloid fibrils formed from Aβ (11-25) and from Aβ (1-42) revealed that although they resembled one another closely in diameter and morphology, Aβ (11-25) appeared to form more consistently homogeneous, straight, uniform fibrils with clearly definededges (**Figure 6(a)**. The Aβ (1-42) fibril showed less contrast, poorly defined edges and did not appear as straight or rigid (**Figure 6(b)**. Close inspection of Aβ (1-42) fibril images did not reveal any additional features (**Figure 6(b)**. The Aβ (1-42) fibrils showed the spacing between the bands measured 4.7-4.8 Å, which corresponds to the hydrogen bonding distance between β-strands. These results appear to directly reveal the β-sheet structure a single amyloid fibril [5,56]. A model has been suggested for Aβ amyloid protofilaments in which, Aβ (12-42) folds into a β-hairpin and associates into four β-sheets, which twist around a central axis. In these models the β-strands are in register between the sheets. Aβ (11-25) fibrils were more ordered, uniform structures. Aβ (1-42) fibrils appeared to have less defined edges and this meant that selecting fibril images was more difficult. It is possible that this is because Aβ (1-42) fibril structure is complicated by loops and disordered protein around the periphery of the fibrils whereas Aβ (11-25) fibrils constitute the core β-sheet structure. The β-strands clearly run perpendicular to the fibre axis. The strong, obvious striations visible across the fibre in these projections indicate that the β-sheets within the

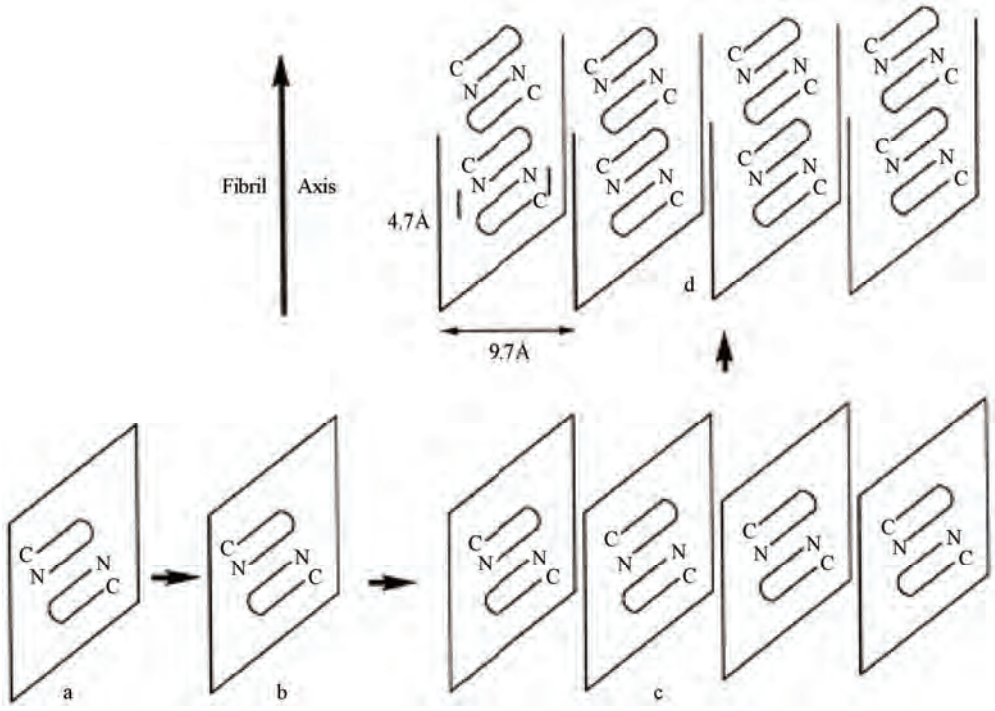

Figure 5. (a) A four-strand antiparallel β-sheet unit from the dimer interface. (b) A dimer of Aβ 12-42 in an antiparallel β-sheet conformation. The distance between any two adjacent strands is ~4.7 Å. (c) The dimer is translated three times in a direction perpendicular to the plane defined by the Cα atoms of the dimer, each by ~9.7 Å. An 8-mer results. (d) A perfectly stacked 16-mer. It was constructed by stacking (parallel) two 8-mers together in the direction of the fibril axis [61].

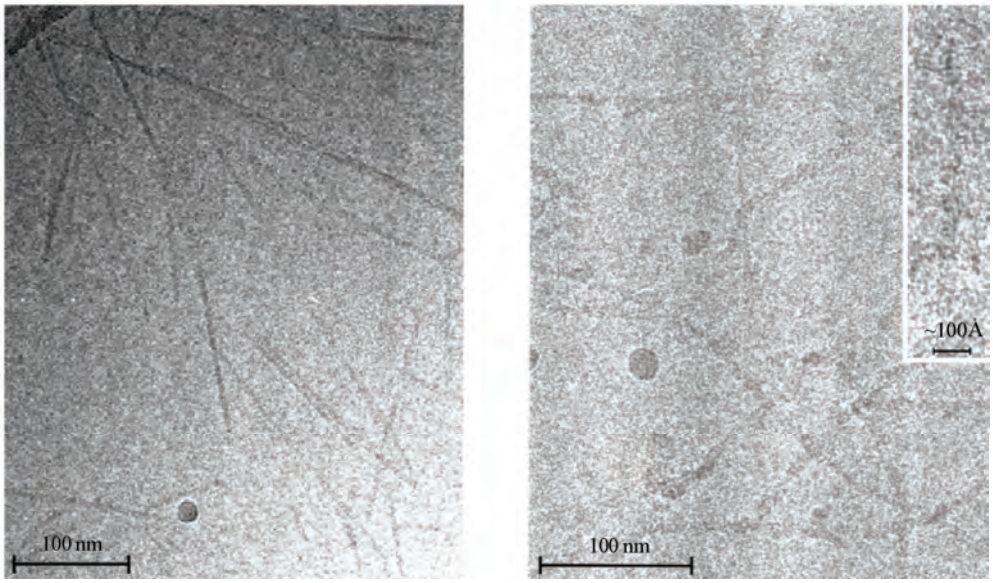

Figure 6. Low dose cryo electron micrograph of (a) Aβ(11 to 25) amyloid fibrils and (b) Aβ(1 to 42) amyloid fibrils. The fibrils formed from both peptides are clearly long, straight and predominantly single. (b) A magnified view of Aβ(1-42) fibril. It is clear from these images that the Aβ(11 to 25) fibrils are straighter and more clearly defined than those of Aβ(1 to 42) [5].

fibril are likely to be in exact register with one another, where a β-strand of one sheet is in register with the β-strand of the adjacent sheet, so that the strands reinforce one another in the image. Amyloid fibrils composed of Aβ peptide are composed of continuous β-sheet structure where the β-strands run perpendicular to the fibre axis.

Electron microscopy has been used as a tool to examine the structure and morphology of these aggregates from ex *vivo* materials, but predominantly from synthetic amyloid fibrils assembled from proteins or peptides *in vitro*. Electron microscopy has shown that the fibrils are straight, unbranching, and are of a similar diameter (60-100 A) irrespective of the precursor protein. Image processing has enhanced electron micrographs to show that amyloid fibrils appear to be composed of protofilaments wound around one another. In combination with other techniques, including X-ray fiber diffraction and solid state NMR, electron microscopy has revealed that the internal structure of the amyloid fibril is a ladder of β-sheet structure arranged in a cross-β conformation [64]. The nonfibrillar oligomeric species are pathogenic, although reports differ as to whether soluble dimers or higher molecular weight protofibrils are toxic. The highly amyloidogenic Aβ 42 forms soluble oligomers extremely rapidly and Aβ 42 could form the pathogenic oligomeric species and/or amyloid fibrils and deposit in senile plaques faster than Aβ 40 [23,31,50,65].

Numerous evidence suggests that β-amyloid found abundantly in the brains of Alzheimer disease patients, is toxic in neuronal cell cultures through a mechanism involving free radicals. Therefore, anti-amyloid strategies are currently being investigated to lower the production of Aβ. Vitamin E prevents the oxidative damage induced by β-amyloid in cell culture and delays memory deficits [66], Another approach is using inhibitor investigation of anti-amyloid strategies to lower the production of Aβ. Using of chemical agents such as Congo red, rifampicin and benzofurans can prevent Aβ oligomerization and the formation of neurotoxic protofibrils but are not appropriate *in vivo* due to their toxicity [67,68].

5. HUNTINGTON

Huntington's disease (HD) is an autosomal-dominant neurodegenerative disorder caused by a CAG triplet repeat expansion coding for a poly-glutamine (polyQ) sequence in the N-terminal region of the Huntington (htt) protein [69]. The first symptoms of Huntington's disease usually occur in the third to fifth decade [70]. As the disease progresses, a variety of motor, emotional/ behavioral, and cognitive symptoms are experienced, including unsteadiness, trouble holding onto things, trouble walking, changes in sleeping patterns, delusions and hallucinations, intellectual decline, and memory loss Which Psychiatric symptoms are among the most common features [71,72].

CAG repeats resulting in long polyglutamine tracts have been implicated in the pathogenesis of at least eight neurodegenerative diseases including Huntington and several spinocerebellar ataxias [73]. Normally, Huntington is a cytoplasmic protein expressed at high levels in the striatal neurons vulnerable to degeneration in HD

and at low or undetectable levels in the neurons resistant to degeneration. In HD brain, N-terminal fragments of mutant huntington were reported to accumulate and form inclusions in the nucleus and identified as a characteristic neuronal intracellular inclusion (NII) [74]. This inclusions contained β-pleated sheet stabilized by hydrogen bonds. In several cases, NI is spherical aggregates, sometimes assembled by insoluble amyloid-like fibrils. Aggregates outside the nucleus have also been observed, but it has been shown recently that nuclear localization is required for toxicity [75]. The poly-Q disorders are also associated with the formation of neuronal nuclear inclusions (NI) whose average size is about 5–7 μm, and formed by aggregates of the protein with the expanded polyglutamine sequence [75,76,77].

The hypothesis that amyloid structures are formed in Huntington's disease (HD) is supported by evidence that polyglutamine forms amyloid like protein aggregates *in vitro*, which stain with Congo Red (a histological stain for amyloid) and exhibit green birefringence under polarized light, [78,79]. Ultrastructural studies of brains of HD transgenic mice revealed neuronal intranuclear inclusion that contained aggregated huntingtin protein with granular or fibrillar morphology. Neuronal intranuclear inclusion with similar structural features also were detected in postmortem brains of HD and spinocerebellar ataxia type 3 patients as well as in stable and transiently transfected cell lines. Furthermore, recombinant proteins with an expanded poly(Q) stretch (51–122 glutamines) were found to form insoluble high molecular weight protein aggregates *in vitro* [80].

Increasing PG length correlates with the number of inclusions, which contributes to earlier onset of illness. *In vivo* inclusions occur primarily in subpopulations of neurons that are affected in the illnesses. *In vitro* expression of PG tracts has been shown to lead to aggregation of proteins by either cross linking or by polar-zipper hydrogen bonding [81,82]. Consistent with this, it was found that the rate of aggregate formation *in vitro* directly correlates with repeat length: the longer the poly(Q) tract, the faster the aggregation rate. Similarly, the protein concentration required for aggregate formation decreased with an increase of the poly(Q) repeat length. *In vitro* aggregation of N-terminal, poly(Q)-containing huntingtin peptides is self initiated and, like a crystallization or Aβ formation, follows a nucleation-dependent pathway. [83].

Thus the formation of amyloidlike huntingtin aggregates *in vitro* not only depends on poly(Q) repeat length but also critically depends on protein concentration and time [79]. Among these, formation of ordered huntingtin aggregates is highly poly(Q) repeat length-dependent, which correlated the age of onset and the severity of HD. The majority of adult-onset cases have expansions ranging from 41 to 55 units, whereas expansions of 70 and above invariably cause the juvenile form of the disease. Interestingly, pathological effects occur in patients only when the length of poly-Q exceeds a rather sharp threshold of 35±40 glutamines. Thus length of the poly-Q tract correlates directly with the age of onset and with the severity of the symptoms in the diseases [79,83].

Discovery of the gene underlying HD can be used as a genetic therapy for a logical step towards finding a cure. Animal models that closely mimic the neurobiological and clinical symptoms of the disease can be used to test experimental treatments for HD across different stages of the disease [71,84].

6. PARKINSON

Parkinson's disease (PD) is an age-related neurodegenerative disorder. In 80% cases PD is most common Parkinsonism which clinically is a syndrome characterized by tremor at rest, rigidity, slowness or absence of voluntary movement, postural, instability, and freezing. PD is a progressive disease, which affects both women and men. It has an effect on ~1% of people beyond 65 years of age, with a higher prevalence in men [85-88]. The postmortem PD *substantia nigra* is characterized by sporadic intraneuronal cytoplasmic inclusions known as Lewy bodies (LB). The presence of Lewy bodies are associated with neurodegenerative disorders such as sporadic and familial Parkinson's disease (PD), dementia with LBs and the LB variant of Alzheimer's disease. The principal component of LBs is the protein α-synuclein, but they also contain various amounts of other proteins, including the molecular chaperones, αB-crystallin, clusterin, torsin A, Hsp27 and Hsp70 [89,90,91,92,93].

α-Synuclein protein and a fragment of it, called NAC. α-Synuclein is a presynaptic protein, which was originally identified as the precursor protein for the non-β-amyloid component (NAC) of Alzheimer's disease (AD) senile plaques. NAC is a 35 amino acid peptide comprising amino acids 61-95 of the α-syn sequence and has been identified as the second major constituent in the plaques of AD brains [94,95,96]. The formation of NAC peptides in a crossed β-pleated sheet conformation was assessed by thioflavine-S staining. Only the aged samples of NAC(1-35) and NAC(1-18) were thioflavine-S positive, indicative of the presence of amyloid-like filaments [97,98].

The involvement of α-synuclein in neurodegenerative diseases was first suspected after the isolation of a α-synuclein fragment (NAC) from amyloid plaques in Alzheimer's disease (AD). Later, two different α-synuclein mutations were shown to be associated with autosomal-dominant Parkinson's disease (PD), but only in a small number of families. However, the discovery that α-synuclein is a major component of Lewy bodies and Lewy neurites, the pathological hallmarks of PD, confirmed its role in PD pathogenesis [99].

Two autosomal dominant mutations in the α-synuclein gene were linked to familial early onset PD: A53T and A30P. The mutations, A30P and A53T, do not affect the conformational behavior of the monomeric protein; wild-type α-synuclein (WT), A53T, and A30P are all ''natively unfolded'' at low concentration. At higher concentrations, WT, A53T, and A30P all form amyloid fibrils of similar morphology by what appears to be a nucleation-dependent mechanism [97]. All three proteins also produce nonfibrillar oligomers that may be assembly intermediates, analogous to the Aβ protofibril. Fibrillization of α-synuclein is clearly accelerated by the A53T mutation but the effect of the A30P mutation on fibril formation has not been determined, although A30P accelerates the formation of nonfibrillar oligomers and the disappearance of unsedimentable protein from solution [100,101]. Circular dichroism spectroscopy indicated that α-synuclein undergoes a conformational change from random coil to β-sheet structure during assembly. X-ray diffraction and electron diffraction of the α-synuclein assemblies showed a cross-β conformation characteristicof amyloid [90].

In vitro multiple factors have been shown to accelerate α-synuclein aggregation. In aqueous solution, α-synuclein is natively unfolded within extended structure composed of random coil without a hydrophobic core. *In vivo*, it binds to rat brain vesicles via the first four 11-mer N-terminal repeats. *In vitro*, it binds to monolayer phospholipid membranes, acquiring an α-helical secondary structure probably formed by the seven N-terminal 11-residue repeats containing the conserved core sequence Lys-Thr-Lys-Glu-Gly-Val [102]. Therapeutic strategies aimed to prevent this aggregation are therefore envisaged. Although little has been learned about its normal function, α-synuclein appears to interact with a variety of proteins and membrane phospholipids, and may therefore participate in a number of signaling pathways. In particular, it may play a role in regulating cell differentiation, synaptic plasticity, cell survival, and dopaminergic neurotransmission. Thus, pathological mechanisms based on disrupted normal function are also possible [102,103].

7. SPONGIFORM AND FAMILIAL AMYLOIDOSIS DISEASES

The transmissible spongiform encephalopathies (TSEs) or prion diseases form a group of fatal neurodegenerative diseases including bovine spongiform encephalopathy, Creutzfeldt-Jakob Disease (CJD) and Gerstmann-Stra¨ussler-Scheinker syndrome (GSS). TSEs, or prion diseases, are mammalian neurodegenerative disorders characterized by a posttranslational conversion and brain accumulation of an insoluble, protease-resistant isoform (PrP^{Sc}) of the host-encoded cellular prion protein (PrP^{C}) [104]. The diseases are rare, but outbreaks of acquired forms of CJD, such as variant CJD and iatrogenic CJD with cadaveric growth hormone or dura grafts, have prompted the development of therapeutic interventions and new diagnostic methods [105]. In humans, prion diseases result from infectious modes of transmission, Gerstmann-Sträussler-Scheinker Syndrome, Fatal Familial Insomnia; and modes of transmission. The clinical symptoms associated with each of the human prion disease forms vary dramatically [106,107].

Cellular prion protein, PrPC, is a predominantly α-helical glycoprotein that remains attached to the outer membrane of the cells through a glycophosphatidyl inositol linkage. A β-sheet-rich conformational isoform of PrP^{C}, termed PrP^{SC}, has been considered to be the infectious agent of the fatal neurodegenerative diseases transmissible spongiform encephalopathies (TSE) and its hereditary forms of spongiform encephalopathies (SE). [104]. $PrPS^{C}$ exists as oligomers and amyloid polymers (fibres) and, unlike PrP^{C}, is resistant to digestion by proteinase K (PK), which is considered as an indicator of formation of PrP^{SC}. However, PrPC may undergo disease-associated structural modifications that do not lead to a protease-resistant molecule, indicating that prion disease can occur in the absence of PrP^{SC}; further protease-resistant prion protein forms without any infectivity can be generated. [108].

Familial amyloidosis may occur in patients with familial Mediterranean fever or it may arise from transthyretin mutations. Approximately 30 such mutations have been described [28]. Transthyretin, previously called prealbumin because it migrates ahead of albumin in standard electrophoretic separations, is a serum carrier of thyroid hormones and vitamin A. The mutant transthyretin is deposited as extracellular twisted β-pleated sheet fibrils in peripheral somatic and autonomic nerves and visceral organs; it causes autonomic and peripheral somatic disorders, and the disease is ultimately fatal [28]. Clinically, patients are susceptible to neuropathic, cardiopathic, or nephropathic complications. Type I familial hereditary generalized amyloidosis is inherited as an autosomal dominant gene mutation with a single amino acid substitution of methionine for valine at position 30 in transthyretin [28].

8. CONCLUSIONS

The topics discussed in this review provide a great deal of evidence for the proteins that have an intrinsic capacity of aggregating and forming structures such as amyloidfibrils. Aggregates are most commonly formed from the interaction of partially folded intermediates containing significant native-like structure. These interactions involve extended chain or β-sheet-like conformations. Thus, both ordered and disordered aggregates show increased βstructure relative to the native conformation (in the case of all-βproteins, the increased βstructure is dis-

tinct from that of the native protein).

Misfolded and aggregated species are likely to owe their toxicity to the exposure on their surfaces of regions of proteins that are buried in the interior of the structures of the correctly folded native states. The exposure of large patches of hydrophobic groups is likely to be particularly significant as such patches favour the interaction of the misfolded species with cell membranes [109,110,111]. Interactions of this type are likely to lead to the impairment of the function and integrity of the membranes involved, giving rise to a loss of regulation of the intracellular ion balance and redox status and eventually to cell death. The data reported so far strongly suggest that the conversion of normally soluble proteins into amyloid fibrils and the toxicity of small aggregates appearing during the early stages of the formation of the latter are common or generic features of polypeptide chains. Moreover, the molecular basis of this toxicity also appears to display common features between the different systems that have so far been studied.

Amyloidosis comprises a group of diseases in which protein tissue deposits have common morphologic structural, and staining properties but variable protein composition [28,37]. In this review we highlighted the relevance of amyloid fibril formation of different protein to diseases. The fibrillar morphology, diagnostic staining characteristics and underlying β-sheet structure of the proteins deposits led to them being classified as amyloid fibrils, and the diseases are now regarded as a protein misfolding disease. There are still many outstanding and critical questions regarding protein aggregation. Among these are questions about the detailed mechanism of the aggregation process, factors determining the kinetics of aggregation, the structural nature of the intermolecular interactions, and how aggregation may be effectively and efficiently prevented, especially *in vivo.*

REFERENCES

[1] Come, J. H., Fraser, P. E. and Lansbury, J., P. T., (1993) A kinetic model for amyloid formation in the prion diseases: Importance of seeding. P. Natl. Acad. Sci. USA. **90**, 5959–5963.

[2] Chiti, F., Webster, P., Taddei, N., Clark, A., Stefani, M., Ramponi, G. and Dobson, C. M. (1999) Designing conditions for in vitro formation of amyloid protofilaments and fibrils. Biochemistry. **96**, 3590–3594.

[3] Arrigo, P. A. and Muller, G. E. W. (2001) ((W. E. G. Muller (Managing Editor), P. J., I.Kostovic, Y. Kuchino, A. Macieira-coelho, R. E. Rhoads, Ed.). Ed.).

[4] van Montfort, L. R., Slingsby, C. and Vierling, E. (2002) Structure and function of the small heat shock protein/ α-crystallin family of molecular chaperones. Protein. Chem. **59**, 105–155.

[5] Serpell, C. L. a. (2000) Alzheimer's amyloid fibrils: Structure and assembly. Biochim. Biophys. Acta. **1502**, 16–30.

[6] Pellarin, R. and Caflisch, A. (2006) Interpreting the aggregation kinetics of amyloid peptides. J. Mol. Biol **360**, 882–892.

[7] Hall, D., Hirota, N. and Dobson, M. C. (2005) A toy model for predicting the rate of amyloid formation from unfolded protein. J. Mol. Biol. **195**, 195–205.

[8] Dobson, M. C. (2001) The structure basis of protein folding and its links with human disease. Phil. Trans. R. Soc. Lond. B.. **356**, 133–145.

[9] Dobson, M. C. (1999) Protein misfolding, evolution and disease. TIBS. **24**, 329–332.

[10] Canet, D., Sunde, M., Last, A. M., Miranker, A., Spencer, A., Robinson, C. V. and Dobson, C. M. (1999) Mechanistic studies of the folding of human lysozyme and the origin of amyloidogenic behavior in its disease-related variants. Biochemistry. **38**, 6419–27.

[11] MacPhee, E. C. and Dobson, C. M. (2000) Chemical dissection and reassembly of amyloid fibril formed by a peptide fragment of transthyretin. J. Mol. Biol. **297**, 1203–1215.

[12] Shirahama, T. and Cohens, A. S. (1967) High-resolution electron microscopic. Analysis of the amyloid fibril. J. Cell. Biol.. **33**, 679–708.

[13] Chamberlain, K. A., MacPhee, E. C., Zurdo, J., Morozova-Roche, A. L., Hill, A. H., Dobson, M. C. and Davis, J. J. (2000) Ultra structural organization of amyloid fibrils by atomic force microscopy. Biophys. J.. **79**, 3282–3293.

[14] Conway, K. A. and Harper, J. D. (2000) Fibrils formed in vitro from α-synuclein and two mutant forms linked to Parkinson's disease are typical amyloid. Biochemistry. **39**, 2552–63.

[15] Cohen, A. S., Shirahama, T. and Skinner, M. (1982) Electron microscopy of amyloid. In electron microscopy of protein. Academic Press Inc, London UK. **3**, 165–205.

[16] Jiménez, J. L., Guijarro, J. I., Orlova, E., Zurdo, J., Dobson, C. M., Sunde, M. and Saibil, H. R. (1999) Cryo-electron microscopy structure of an SH3 amyloid fibril and model of the molecular packing. EMBO. **18**, 815–821.

[17] Serpell, L. C., Sunde, M., E., F. P., Luther, P. K., Morris, E. P., Sangren, O., Lundgren, E. and Blake, C. C. (1995) Examination of the structure of the transthyretin amyloid fibril by image reconstruction from electron micrographs. J. Mol. Biol.. **254**, 113–8.

[18] Kirschner, A. D., Abraham, C. and Selkoe, J. D. (1986) X-ray diffraction from intraneuronal paired helical filaments and extraneuronal amyloid fibers in alzheimer disease indicates cross-β conformation. P. Natl. Acad. Sci. USA. **83**, 503–508.

[19] Blake, C. and Serpell, L. (1996) Synchrotron X-ray studies suggest that the core of the transthyretin amyloid fibril is a continuous β-sheet helix. Structure. **4**, 989–98.

[20] Sunde, M., Serpell, L. C., Bartlam, M., Fraser, P. E., Pepys, M. B. and Blake, C. F. (1997) Common core structure of amyloid fibrils by synchrotron X-ray diffraction. J. Mol. Biol. **273**, 729–739.

[21] Guijarro, I. L., Sunde, M., Jones, A. J., Campbell, D. I. and Dobson, M. C. (1998) Amyloid fibril formation by an SH3 domain. Biochemistry. **95**, 4224–4228.

[22] Plakoutsi, G., Bemporad, F., Calamai, M., Taddei, N., Dobson, M. C. and Chiti, F. (2005) Evidence for a mechanism of amyloid formation involving molecular

reorganisation within native-like precursor aggregates. J. Mol. Biol. **351**, 910–922.

[23] Cecchini, M., Curcio, R., Pappalardo, M., Melki, R. and Caflisch, A. (2006) A Molecular Dynamics Approach to the Structural Characterization of Amyloid Aggregation. J. Mol. Biol. **357**, 1306–1321.

[24] Hatters, D. M., Wilson, M. R., Easterbrook-Smith, S. B. and Howlett, G.J. (2002) Suppression of apolipoprotein C-II amyloid formation by the extracellular chaperone, clusterin Eur. J. Biochem. **269**, 2789–2794.

[25] Haley, D. A., Horwitz, J. and Stewart, P. L. (1998) The small Heat-Shock protein,aB-crystallin, has a variable quaternary structure. J. Mol. Biol. **277**, 27–35.

[26] Jacchieri, G. S. (1998) Study of a-helix to b-strand to b-sheet transitions in amyloid: the role of segregated hydrophobic b-strands. Biophysical Chemistry. **74**, 23–34.

[27] Milner-White, J. E., Watson, D. J., Qi, G. and Hayward, S. (2006) Amyloid formation may involve a- to b-sheet interconversion via peptide plane flipping. Structure. **14**, 1369–1376.

[28] Horwitz, S., Thomas, C., Gruener, G., Nand, S. and Shea, F. J. (1998) MR of Leptomeningeal Spinal and Posterior Fossa Amyloid. AJNR Am J Neuroradiol. **19**, 900–902.

[29] Horowitz, S., Thomas, C., Gruener, G., Nand, S. and Shea, F. J. (1998) MR of Leptomeningeal Spinal and Posterior Fossa Amyloid. AJNR Am J Neuroradiol. **19**, 900–902.

[30] Tycko, R. (2000) Solid-state NMR as a probe of amyloid fibril structure. Curr. Opin. Chem. Biol. **4**, 500–506.

[31] Makin, S. O., Atkins, E., Sikorski, P., Johansson, J. and Serpell, C. L. (2005) Molecular basis for amyloid fibril formation and stability. PNAS. **102**, 315–320.

[32] Otoo, N. H., Lee, G.K., Qiu, W. and Lipke, N. P. (2008) Candida albicans Als adhesins have conserved amyloid-forming sequences. Eukaryotic Cell. **7**, 776–782.

[33] Religa, D., Laudon, H., Styczynska, M., Winblad, B., Näslund, J. and Haroutunian, V. (2003) Amyloid β Pathology in Alzheimer's Disease and Schizophrenia. Am J Psychiatry. **160**, 867–872.

[34] Barrel, J. M., Broadley, S. A., Schaffar, G. and Hart, F. U. (2004) Role of molecular chaperones in protein misfolding diseases. Semin. Cell. Dev. Biol. **15**, 17–29.

[35] Ellidson and Bottomley (2004) The role of Misfolding in the pathogenesis of human diseases. IUBMB life. **56(3)**, 119–123.

[36] Carrell, R. W. and Lomas, D. A. (1997) Conformational diseas. Lancet. **350**, 134–138.

[37] Small, W. G., Kepe, V., Ercoli, M. L., Siddarth, P., Bookheimer, Y. S., Miller, J. K., Lavretsky, H., Burggren, C. A., Cole, M. G., Vinters, V. H., Thompson, M. P., Huang, C. S., Satyamurthy, N., Phelps, E. M. and Barrio, R. J. (2006) PET of brain amyloid and Tau in mild cognitive impairment. N. Engl. J. Med. **355**, 2652–2663.

[38] Selkoe (2003) Folding proteins in fatal ways. Nature. **426(6968)**, 900–904.

[39] Han, H., Weinreb, H. P. and Lansbury, T. P. (1995) The core Alzheimer's peptide NAC forms amyloid fibrils which seed and are seeded by p-amyloid: is NAC a common trigger or target in neurodegenerative disease? Chemistry & Biology. **2**, 163–l69.

[40] Shoghi-Jadid, K., Barrio, R. J., Kepe, V., Wu, M. H., Small, W. G., Phelps, E. M. and Huang, C. S. (2005) Imaging b-amyloid fibrils in Alzheimer's disease: a critical analysis through simulation of amyloid fibril polymerization. Nuclear Medicine and Biology. **32**, 337–351.

[41] Miura, Y., You, C. and Ohnishi, R. (2008) Inhibition of Alzheimer amyloid aggregation by polyvalent trehalose. SCIENCE AND TECHNOLOGY OF ADVANCEDMATERIALS (Sci. Technol. Adv. Mater). **9**, 1–6.

[42] Sefton, F. C. and Yu, G. (2008) Ab Predictor of Alzheimer disease symptoms Arch Neurol. **65**, 875–876.

[43] Malm, T., Ort, M., Tä htivaara, L., Jukarainen, N., Goldsteins, G., Puolivä li, J., Nurmi, A., Pussinen, R., Ahtoniemi, T., Miettinen, K. T., Kanninen, K., Leskinen, S., Vartiainen, N., Yrjä nheikki, J., Laatikainen, R., Harris-White, E. M., Koistinaho, M., Frautschy, A. S., Bures, J. and Koistinaho, J. (2006) b-Amyloid infusion results in delayed and age-dependent learning deficits without role of inflammation or b-amyloid deposits. PNAS **103**, 8852–8857.

[44] Grundman, M., Petersen, R. C., Ferris, H. S., Thomas, R. G., Aisen, S. P., Bennett, A. D., Foster, L. N., Jack, R. C., Galasko, R. D., Doody, R., Kaye, J., Sano, M., Mohs, R., Gauthier, S., Kim, T. H., Jin, S., Schultz, N. A., Schafer, K., Mulnard, R., Dyck, V. H. C., Mintzer, J., Zamrini, Y. E., Cahn-Weiner, D. and Thal, J. L. (2004) Mild cognitiveimpairment can be distinguished from Alzheimer Disease and normal aging for clinical trials. Arch Neurol. **61**, 59–66.

[45] Huang, J. H. T., Yang, S. D., Plaskos, N. P., Go, S., Yip, M. C., Fraser, E. P. and Chakrabartty, A. (2000) Structural Studies of Soluble Oligomers of the Alzheimer b-Amyloid Peptide. J. Mol. Biol. **297**, 73–87.

[46] Rosenberg, N. R. (2000) Explaining the cause of the amyloid burden in Alzheimer disease. Arch Neurol. **59**, 1367–1368.

[47] Irie, K., Murakami, K., Masuda, Y., Morimoto, A., Ohigashi, H., Ohashi, R., Takegoshi, K., Nagao, M., Shimizu, T. and Shirasawa, T. (2005) Structure of B-amyloid fibrils and its relevance to their neurotoxicity: implications for the pathogenesis of Alzheimer's disease. Journal of Bioscience and Bioengineering. **99**, 437–447.

[48] Rivière, C., Richard, T., Quentin, L., Krisa, S., Mérillon, M. J. and Monti, P. J. (2007) Inhibitory activity of stilbenes on Alzheimer's b-amyloid fibrils in vitro. Bioorganic & Medicinal Chemistry. **15**, 1160–1167.

[49] Hardy, J. and Selkoe, D. J. (2002) The amyloid hypothesis of Alzheimer's disease: Progress and problems on the road to therapeutics. Science. **297**, 353–356.

[50] Sachse, C., Xu, C., Wieligmann, K., Diekmann, S., Grigorieff, N. and Fändrich, M. (2006). Quaternary structure of a mature amyloid fibril from Alzheimer's Aβ(1-40) peptide. J. Mol. Biol. **362**, 347–354.

[51] Ma, B. Y. and Nussinov, R. (2002) Stabilities and conformations of Alzheimer's b-amyloid peptide oligomers (Ab (16–22), Ab (16–35) and Ab (10–35)): Sequence effects. Proc. Natl Acad. Sci. USA. **99**, 14126–14131.

[52] Buchete, V. N., Tycko, R. and Hummer, G. (2005) Molecular dynamics simulations of Alzheimer's b-Amyloid protofilaments. J. Mol. Biol. **353**, 804–821.

[53] JimeÂnez, L. J., Tennent, G., Pepys, M. and Saibil, R. H. (2001) Structural Diversity of ex vivo Amyloid Fibrils Studied by Cryo-electron Microscopy. J. Mol. Biol. **311**, 241–247.

[54] Gilead, S. and Gazit, E. (2005) Self-organization of short peptide fragments: From amyloid fibrils to nanoscale supramolecular assemblies. Supramolecular Chemistry. **17**, 87–92.

[55] Pellarin, R., Guarnera, E. and Caflisch, A. (2007) Pathways and intermediates of amyloid fibril formation. J. Mol. Biol. **374**, 917–924.

[56] Serpell, L. C. and Smith, J. M. (2000) Direct visualisation of the b-sheet structure of synthetic Alzheimer's amyloid. J. Mol. Biol. **299**, 225–231.

[57] Klement, K., Wieligmann, K., Meinhardt, J., Hortschansky, P., Richter, W. and Fändrich, M. (2007) Effect of different salt ions on the propensity of aggregation and on the structure of Alzheimer's Aβ(1-40) amyloid fibrils. J. Mol. Biol. **373**, 1321–1333.

[58] Ban, T., Hoshino, M., Takahashi, T., Hamada, D., Hasegawa, K., Naiki, H. and Goto, Y. (2004) Direct observation of Ab amyloid fibril growth and inhibition. J. Mol. Biol. **344**, 757–767.

[59] Idicula-Thomas, S. and Balaji, V. P. (2007) Protein aggregation: A perspective from amyloid and inclusion-body formation. CURRENT SCIENCE. **92**, 758–767.

[60] Li, L., Darden, A. T., Bartolotti, L., Kominos, D. and Pedersen, G. L. (1999) An atomic model for the pleated b-sheet structure of Ab- amyloid protofilaments. Biophys J. **76**, 2871–2878.

[61] Weinreb, P. H., Jarrett, J. T. and Lansbury, P. T. (1994) Peptide models of a hydrophobic cluster at the C-terminus of the amyloid protein. J. Am. Chem. Soc. **116**, 10835–10836.

[62] Williams, A. D., Portelius, E., Kheterpal, I., Guo, J., Cook, K. D., Xu, Y. and Wetzel, R. (2004) Mapping A-amyloid fibril secondary structure using scanning proline mutagenesis. J. Mol. Biol. **335**, 833–842.

[63] Lazo, N. D. and Downing, D. T. (1999). Fibril formation by amyloid b-proteins may involve b-helical protofibrils. J. Pept. Res., **53**, 633–640.

[64] Thusnelda, S. and Louise C, S. (2005) Structure and morphology of the Alzheimer's amyloid fibril, Microscopy Research and Technique, **67**, 210–217.

[65] El-Agnaf, A. M. O., Mahil, S. D., Patel, P. B. and Austen, M. B. (2000) Oligomerization and Toxicity of b-Amyloid-42 Implicated in Alzheimer's Disease. Biochemical and Biophysical Research Communications. **273**, 1003–1007.

[66] Grundman, M. (2000) Vitamin E and Alzheimer disease: the basis for additional clinical trials. Am Clin Nutr. **71**, 630S–636S.

[67] Tuszynski, H. M., Thal, L., Pay, M., Salmon, P. D., Sang U, H., Bakay, R., Patel, P., Blesch, A., Vahlsing, L. H., Ho, G., Tong, G., Potkin, G. S., Fallon, J., Hansen, L., Mufson, J. L., Kordower, H. J., Gall, C. and Conner, J. (2005) A phase 1 clinical trial of nerve growth factor gene therapy for Alzheimer disease. Nat. Med. **11**, 551–555.

[68] Martin, K. B., Meinert, L. C. and Breitner, S. C. J. (2002) Double placebo design in a prevention trial for Alzheimer's disease. Cont. Clin. Trials. **23**, 93–99.

[69] Dı´az-Hernández, M., Torres-Peraza, J., Salvatori-Abarca, A., Morán, M.A., Gómez-Ramos, P., Alberch, J. and Lucas, J. J. (2005) Full motor recovery despite striatal neuron loss and formation of irreversible amyloid-like inclusions in a conditional mouse model of Huntington's Disease. The Journal of Neuroscience. **25(42)**, 9773–9781.

[70] Gusella, J. F., Wexler, N. S., Conneally, P. M., Naylor, S. L., Anderson, M. A., Tanzi, R. E., Watkins, P. C., Ottina, K., Wallace, M. R., Sakaguchi, A. Y., Young, A. B., Shoulson, I., Bonilla, E. and Martin, J. B. (1983) A polymorphic DNA marker genetically linked to Huntington; s disease. Nature. **306**, 234–238.

[71] Anderson, K. E., Louis, E. D., Stern, Y. and Marder, K. S. (2001) Cognitive Correlates of Obsessive and Compulsive Symptoms in Huntington's Disease. Am J Psychiatry. **158**, 799–801.

[72] Mitchell, I. J., Heims, H., Neville, E.A. and Rickards, H. (2005) Huntington's disease patients show impaired perception of disgust in the gustatory and olfactory modalities. J. Neuropsychiatry Clin Neurosci. **17**, 119–121.

[73] Hirakura, Y., Azimov, R., Azimova, R. and Kagan, L. B. (2000) Polyglutamine-Induced Ion Channels: A Possible Mechanism for the Neurotoxicity of Huntington and Other CAG Repeat Diseases. Journal of Neuroscience Research. **60**, 490–494.

[74] Davies, W. S., Beardsall, K., Turmaine, M., DiFiglia, M., Aronin, N. and Bates, P. G. (1998) Are neuronal intranuclear inclusions the common neuropathology of triplet-repeat disorders with polyglutamine-repeat expansions? THE LANCET. **351**, 131–33.

[75] Temussi, A. P., Masino, L. and Pastore, A. (2003) From Alzheimer to Huntington: why is a structural understanding so difficult? The EMBO Journal. **22**, 355–361.

[76] Karpug, V. M., Becher, W. M., Springer, E. J., Chabas, D., Youssef, S., Pedotti, R., Mitchell, D. and Steinman, L. (2002). Prolonged survival and decreased abnormal movements in transgenic model of Huntington disease, with administration of the transglutaminase inhibitor cystamine. Nat. Med. **8**, 143–149.

[77] Karpuj, V. M., Becher, W. M., Springer, E. J., Chabas, D., Youssef, S., Pedotti, R., Mitchell, D. and Steinman, L. (2002) Prolonged survival and decreased abnormal movements in transgenic model of Huntington disease, with administration of the transglutaminase inhibitor cystamine. Nature Medicine. **8**, 143–149.

[78] Hoffner, G. and Djian, P. (2000) Protein aggregation in Huntington's disease. Biochimie. **84**, 273–278.

[79] Mcgowan, P. D., Vanroon-Mom, W., Holloway, H., Bates, P. G., Mangiarini, L., Cooper, S. J. G., R., F. L. and Snell, G. R. (2000) Amyloid-lioke inclusions in huntington, s disease. Neuroscience. **100**, 677–680.

[80] Gutekunst, A. C., Li, H. S., Yi, H., Mulroy, S. J., Kuemmerle, S., Jones, R., Rye, D., Ferrante, J. R., Hersch, M.S. and Li, J.X. (1999) Nuclear and Neuropil Aggregates in Huntington's Disease: Relationship to Neuropathology. The Journal of Neuroscience. **19(7)**, 2522–2534.

[81] Ross, A. C. (2002) Polyglutamine pathogenesis: emergence of unifying mechanisms for Huntington's disease and related disorders. Neuron. **35**, 819–822.

[82] Dahlgren, R. P., Karymov, A. M., Bankston, J., Holden, T., Thumfort, P., Ingram, V. M. and Lyubchenko, L. Y. (2005) Atomic force microscopy analysis of the Hunting-

ton protein nanofibril formation. Nanomedicine: Nanotechnology, Biology and Medicine. **1**, 52–57.

[83] Scherzinger, E., Sittler, A., Schweiger, K., Heiser, V., Lurz, R., Hasenbank, R., Bates, P.G., Lehrach, H. and Wanker, E. E. (1999) Self-assembly of polyglutamine-containing huntingtin fragment into amyloid-like fibrils: Implications for Huntington's disease pathology. Proc. Natl. Acad. Sci. USA. **96**, 4604–4609.

[84] Borlongan, C. V., Koutouzis, T. K., Freeman, T. B., Cahill, D. W. and Sanberg, P. R. (1995) Behavioral pathology induced by repeated systemic injections of 3-nitropropionic acid mimics the motoric symptoms of Huntington's disease. Brain Res. **697**, 254–257.

[85] Spillantini, G. M., Crowther, A. R., Jakes, R., Hasegawa, M. and Goedertm, M. (1998) A-synuclein in filamentous inclusions of Lewy bodies from Parkinson's disease and dementia with Lewy bodies. Proc. Natl. Acad. Sci. USA. **95**, 6469–6473.

[86] Recchia, A., Debetto, P., Negro, A., Guidolin, D., Skaper, D. S. and Giusti, P. (2004) A-Synuclein and Parkinson's disease. The FASEB J. **18**, 617–626.

[87] Dauer, W. and Przedborski, S. (2003) Parkinson's disease: mechanisms and models. Neuron. **39**, 889–909.

[88] Hariz, G. and Hriz, I. M. (2000) Gender distribution in surgery for Parkinson's disease. Parkinsonism Relate Disord. **6**, 155–157.

[89] Iwaki, T., Wisniewski, T., Iwaki, A., Corbin, E., Tomokane, N., Tateishi, J. and Goldman, J. E. (1992) Accumulation of aB-crystallin in central nervous system glia and neurons in pathologic conditions. Am. J. Path. **140**, 345–356.

[90] Serpell, C. L., Berriman, J., Jakes, R., Goedert, M. and Crowther, A. R. (2000) Fiber diffraction of synthetic a-synuclein filaments shows amyloid-like cross-b conformation. PNAS. **97**, 4897–4902.

[91] Mizutani, T., Inose, T., Nakajima, S., Kakimi, S., Uchigata, M. and Ikeda, K. (1998) Familial parkinsonism and dementia with ballooned neurons, argyrophilic neuronal inclusions, atypical neurofibrillary tangles, tau-negative strocytic fibrillary tangles, and Lewy bodies.. Acta Neuropathol. (Berl). **95**, 15–27.

[92] Sasaki, K., Doh-ura, K., Wakisaka, Y. and Iwaki, T. (2002) Clusterin/apolipoprotein J is associated with cortical Lewy bodies: immunohistochemical study in cases with alpha-synucleinopathies. Acta Neuropathol. (Berl). **104**, 225–230.

[93] McLean, P. J., Kawamata, H., Shariff, S., Hewett, J., Sharma, N. and Ueda, K. (2002) Torsin A and heat shock proteins act as molecular chaperones: suppression of alpha-synuclein aggregation. J. Neuro. **83**, 846–854.

[94] Splllantini, G. M. a., Crowther, A. R., JAKES, R., Cairns, J. N., Lantos, L. P. and Goedert, M. (1998) Filamentous a-synuclein inclusions link multiple system atrophy with Parkinson's disease and dementia with Lewy bodies. Neuroscience. **251**, 205–208.

[95] El-Agnaf, A. M. O., Jakes, R., Curran, D. M. and Wallace, A. (1998) E¡ects of the mutations Ala30 to Pro and Ala53 to Thr on the physical and morphological properties of K-synuclein protein implicated in Parkinson's disease. FEBS. **440**, 67–70.

[96] Spillantini, G. M. a., Crowther, A. R., JAKES, R., Cairns, J. N., Lantos, L. P. and Goedert, M. (1998) Filamentous a-synuclein inclusions link multiple system atrophy with Parkinson's disease and dementia with Lewy bodies. Neuroscience. **251**, 205–208.

[97] El-Agnaf, A. M. O., JAKES, R., Curran, D. M., Middleton, D., Ingenito, R., Bianchi, E., Pessi, A., Neill, D. and Wallace, A. (1998) Aggregates from mutant and wild-type a-synuclein proteins and NAC peptide induce apoptotic cell death in human neuroblastoma cells by formation of L-sheet and amyloid-like ¢laments. FEBS. **440**, 71–75.

[98] Arima, K., Hirai, S., Sunohara, N., Aoto, K., Izumiyama, Y., Ue´da, K., Ikeda, K. and Kawai, M. (1999) Cellular co-localization of phosphorylated tau- and NACPr a-synuclein-epitopes in Lewy bodies in sporadic Parkinson's disease and in dementia with Lewy bodies. Brain Research. **843**, 53–61.

[99] Arima, K., Ue´da, K., Sunohara, N., Hirai, S., Izumiyama, Y., Tonozuka-Uehara, H. and Kawai, M. (1998) Immunoelectron-microscopic demonstration of NACPra-synuclein-epitopes on the filamentous component of Lewy bodies in Parkinson's disease and in dementia with Lewy bodies. Brain Research. **808**, 93–100.

[100] Conway, A. K., Lee, J. S., Rochet, C. J., Ding, T. T., Williamson, E. R. and Lansbury, T. P. (2000) Acceleration of oligomerization, not fibrillization, is a shared property of both a-synuclein mutations linked to early-onset Parkinson's disease: Implications for pathogenesis and therapy. PNAS. **97**, 571–576.

[101] Conway, A. K., Harper, J. D. and Lansbury, P. T. (2000) Fibrils Formed in Vitro from R-Synuclein and Two Mutant Forms Linked to Parkinson's Disease are Typical Amyloid. Biochem. **39**, 2552–2563.

[102] Lu¨cking, B. C. and Brice, A. (2000) a-synuclein and Parkinson's disease. CMLS, Cell. Mol. Life Sci. **57**, 1894–1908.

[103] Williams, A. D., Portelius, E., Kheterpal, I., Guo, J., Cook, K. D., Xu, Y. and Wetzel, R. (2004) Mapping A amyloid fibril secondary structure using scanning proline mutagenesis. J. Mol. Biol. **335**, 833–842.

[104] Casalone, C., Zanusso, G., Acutis, P., Ferrari, S., Capucci, L., Tagliavini, F., Monaco, S. and Caramelli, M. (2004) Identification of a second bovine amyloidotic spongiform encephalopathy: Molecular similarities with sporadic Creutzfeldt-Jakob disease. PNAS **101**, 3065–3070.

[105] Ishikawa, K., Doh-ura, K., Kudo, Y., Nishida, N., Murakami-Kubo, I., Ando, Y., Sawada, T. and Iwaki, T. (2004) Amyloid imaging probes are useful for detection of prion plaques and treatment of transmissible spongiform encephalopathies. Journal of General. **85**, 1785–1790.

[106] Aguzzi, A., Heikenwalder, M. and Miele, G. (2004) Progress and problems in the biology, diagnostics, and therapeutics of prion diseases. J. Clin. Invest. **114**, 153–160.

[107] Weissmann, C. and Aguzzi, A. (2005) Approaches to therapy of prion diseases. Ann. Rev. of Med. **56**, 321–344.

[108] Nandi, P. K. and Nicole, J.-C. (2004) Nucleic acid and prion protein interaction produces spherical amyloids which can function in vivo as coats of spongiform en-

cephalopathy agent. J. Mol. Biol. **344**, 827–837.
[109] Kourie, J I and A, S. A. (2000) Properties of cytotoxic peptide-induced ion channels. Am J Physiol Cell Physiol. **278**, C1063–C1087.
[110] Kourie, J. I. and L, H. C. (2002) Ion channel formation and membrane-linked pathologies of misfolded hydrophobic proteins:the role of dangerous unchaperoned molecules. Clin Exp Pharmacol Physiol, **29**, 741–753.
[111] Volles, M. J. and T, L. P. (2001) Vesicle permeabilization by protofibrillar α-synuclein: comparison of wild-type with Parkinson's disease linked mutants and insights in the mechanisms. Biochem. **40**, 7812.7819.
[112] Williams, A. D., Portelius, E., Kheterpal, I., Guo, J., Cook, K. D., Xu, Y. and Wetzel, R. (2004) Mapping A amyloid fibril secondary structure using scanning proline mutagenesis. J. Mol. Biol. **335**, 833–842.
[113] Dobson. (2004) Principle of protein folding, Misfolding and aggregation. Semin. Cell. Dev. Biol. **15**, 3–16.
[114] Thomas, Q. and Pederson. (1995) Defective protein folding as a basis of human diseases. TIBS. **20 (11)**, 456–459.
[115] Welch and Brown (1996) Influence of molecular and chemical chaperones on protein folding. Cell Stress Chaperone. **1(2)**, 109–115.

Appendix

APP	Abbreviation: Amyloid precursor protein
AD	Alzheimer's disease
HD	Huntington's disease
PD	Parkinson's disease
LBs	Lewy bodies
TSEs	Transmissible spongiform encephalopathies

J. Biomedical Science and Engineering, 2009, 2, 359-362 **JBiSE**
doi: 10.4236/jbise.2009.25051 Published Online September 2009 (http://www.SciRP.org/journal/jbise/).

Applications of fuzzy similarity index method in processing of hypnosis

Soroor Behbahani[1], Ali Motie Nasrabadi[2]

[1]Biomedical Engineering Department, Islamic Azad University, Science and Research Branch, Tehran, Iran; [2]Biomedical Engineering Department, Faculty of Engineering, Shahed University, Tehran, Iran.
Email: [1]Soroor_Behbahani@yahoo.com; [2]nasrabadi@shahed.ac.ir

Received 1 June 2009; revised 10 July 2009; accepted 12 July 2009.

ABSTRACT

The brain is a highly complex system. Understanding the behavior and dynamics of billions of interconnected neurons from the brain signal requires knowledge of several signal- processing techniques, from the linear and non-linear domains. The analysis of EEG signals plays an important role in a wide range of applications, such as psychotropic drug research, sleep studies, seizure detection and hypnosis processing. In this paper we accomplish to analyze and explore the nature of hypnosis in Right, Left, Back and Frontal hemisphere in 3 groups of hypnotizable subjects by means of Fuzzy Similarity Index method.

Keywords: Fuzzy Similarity Index; Hypnosis; Left-Right; Frontal-Back Hemisphere; Higuchi; Entropy; Energy; Frequency Band

1. INTRODUCTION

The analysis of EEG signals plays an important role in a wide range of applications, such as psychotropic drug research, sleep studies, seizure detection and hypnosis processing. Still it is unclear that what happens in the brain during hypnosis. Changes in different EEG frequencies have already been reported in association with hypnosis; however, it is difficult to compare different studies with each other because of methodological differences as well as different criteria when selecting subjects for experiments. EEG during pure hypnosis would differ from the normal non hypnotic EEG [1].

Various EEG analysis methods have been proposed in the literature, and some of these methods achieved good results in specific applications [2].

Today's Fuzzy theory is one of principal method of researches. A number of basic concepts and methods already introduced in the early stages of the theory have become standard in the application of fuzzy-theoretic tools to medical artificial intelligence subjects [3].

The notion of similarity involves an elaborate cognitive whenever the assessment of similarity should reproduce the judgment of a human observer based on qualitative features, it is appropriate to model it as a cognitive process that simulates human similarity perception.

Among the various knowledge representation formalisms that have been proposed as ways of reasoning in the presence of uncertainty and imperfect knowledge, a situation typical to the human cognitive processes, fuzzy logic has very important features because:

• Fuzzy set theory has been proved a plausible tool for modeling and mimicking cognitive processes, especially those concerning recognition aspects, and

• Fuzzy set theory is able to handle qualitative no numerical descriptions, approximate class memberships and possibility reasoning [4,5].

In this study we propose to explore the nature of hypnosis in Right, Left, Back and Frontal hemisphere in 3 groups of hypnotizable subjects by means of Fuzzy Similarity Index method.

2. FUZZY SIMILARITY INDEX (FSI)

To identify the change state of a system, one of the simplest methods is to compare the feature sets of the present state and ones of the previous states. If the both states are very similar, then it means that the feature sets does not show a large change. After the feature extraction process, a fuzzy membership function can be used to transfer the present and previous features as two fuzzy sets. The parameters of the fuzzy membership function can be determined by the features. Fuzzy sets can be obtained from the feature sets of the signals under study by repeating the fuzziness process. Suppose two fuzzy sets A and B and each set includes N features $x_1, x_2, ..., x_N$, a reliable and simple method can be used to compute the similarity between the two fuzzy sets, A and B as follows:

$$S(A,B)=\frac{\sum_{i=1}^{N}\left(1-\left|\mu_A(x_i)-\mu_B(x_i)\right|\right)}{N} \quad (1)$$

where $1-\left|\mu_A(x_i)-\mu_B(x_i)\right|$ can be regarded as the similarity degree of fuzzy sets A and B on the features xi. S (A, B) is the average of the similarity degree of fuzzy sets A and B, called fuzzy similarity index. The range of $S(A,B)$ is from 0 to 1, which corresponds to the different similarity degree. $S(A,B)=1$, means the two signals are identical; otherwise there exist a difference between the two signals [5].

Decision making is performing in two stages: feature extraction by computing the entropy and energy of each signal and computing fuzzy similarity index of feature sets between the reference EEG signals and the other classes of EEG signals.

2.1. Experimental Data

EEG data used in this study was collected by Ali Moti Nasrabadi [6]. The data collected from 32 Right hand subjects, 4 low (below 20 at Stanford scale), 16 medium (between 20-40) and 12 subjects were high (more than 40) hypnotizable. EEG signals are obtained from subjects using 19 electrodes placed at fp2,fp1,f8,f4, fz,f3,f7, t4,c4,cz,c3,t3,t6,p4,pz,p3,t5,o2,o1 locations. The electrodes are positioned as per the international 10 -20 system illustrated in **Figure 1** [7].

The sampling frequency was **256** Hz. To explore the relation of hypnotizability and similarity of Right–Left and Frontal-Back hemispheres during the hypnosis process between the 3 groups of hypnotizable subjects, 16 and 14 channels of electrodes placed at the fp2,fp1,f8, f4,f3,f7,t4,c4,c3,t3,t6,p4,p3,t5,o2,o1(Right-Left) and fp1, fp2, f3, f4, fz, pz, p3, p4, f8, f7, t6, t5, o1, o2 (Frontal-Back) locations was chosen respectively.

3. FEATURE EXTRACTION

In this experiment a simple algorithm is used to extract the features from the EEG signals. Although Similarity Index method is usually perform with two features (energy, entropy) we decided to find the best features which could discriminate **3** groups of hypnotizability in Left-Right and Frontal-Back hemispheres during hypnosis.

We performed the similarity index method wit **3** kinds of features, at first exam we use the usual features, energy and entropy, at second we use the entropy, Higuchi fractal dimension and at third, entropy, Higuchi and frequency band features were used.

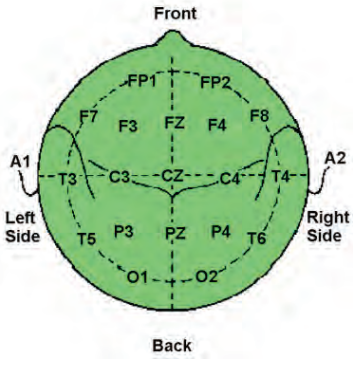

Figure 1. Electrode positions for data collection (10-20 standard).

3.1. Entropy

An entropy measure (Shannon's entropy) can be calculated directly from the EEG data samples by examining the probability distribution of the amplitudes of the data values:

$$SE=-\sum_{i=1}^{M}p_i\log(p_i) \quad (2)$$

where, M is the number of bin that the amplitudes of the EEG are partitioned into and p_i is the probability associated with the i_{th} bin.

3.2. Fractal Dimension

Fractal dimension can be used as a feature to show the complexity and self similarity of the signal. It has a relation with entropy, and entropy has a direct relationship with the amount of information inside a signal. Fractal dimension can be interpreted simply as the degree meandering (or roughness or irregularity) of a signal.

Consider $x(1),x(2),...,x(N)$ be the time sequence to be analyzed. Construct $x(1),x(2),...,x(N)$ new time series x_m^k as $x_m^k=\{x(m),x(m+k),...,x(m+\lfloor(N-m)/k\rfloor k\}$ For $m=1,2,..,k$ where m indicates the initial time value, $x(1),x(2),...,x(N)$ indicates the discrete time interval between points(delay) and $\lfloor a\rfloor$ means integer part of a. for each of curves or time series x_m^k constructed, the average length $L_m(k)$ is computed as

$$L(m,k)=\frac{(N-1)\sum_{}^{\lfloor(N-m)/K\rfloor}\left|x(m+ik)-x(m+(i-1)\right|}{\lfloor(N-m)/k\rfloor k} \quad (3)$$

where N is the length of time sequence and $(N-1)/\{\text{int}[(N-m)/k]\times k\}$ is a normalize factor. Total average length $L(k)$ is computed for all time series having the same delay k but different m as:

$$L(k)=\sum_{m=1}^{k}L_m(k) \quad (4)$$

This procedure is repeated for each k ranging from

1 to k_{max}. The total average length for delay k, $L(k)$ is proportional to k^{-D} where D is fractal dimension by Higuchi's method [8].

3.3. Frequency Band

EEG contains different specific frequency components, which carry the discriminative information. Normally, most waves in the EEG can be classified as alpha, beta, theta and delta waves. The definition of the boundaries between the bands is somewhat arbitrary, however, in most of applications these are defined as; delta (less than 4 Hz), theta (4-8 Hz), alpha (8-13 Hz) and beta (13-30 Hz). When the awake person's attention is directed to some specific type of mental activity, the alpha waves are replaced by asynchronous, higher frequency beta waves. Beta waves occur at frequencies greater than 13 Hz. Theta waves have frequencies between 4 and 8 Hz. They occur normally in parietal and temporal regions in children, but they also occur during emotional stress in some adults. Theta waves also occur in many brain disorders, often in degenerative brain states. Delta waves include all the waves of the EEG with frequencies less than 4 Hz, and they occur in very deep sleep, in infancy and in serious organic brain disease. Therefore, EEG contains different specific frequency components, which carry the discriminative information [5].

4. STATISTICS

In order to reveal any statistically significant differences between any two conditions, the ANOVA method was used separately for each type. Statistical significance was assumed where $p < 0.05$ (only statistically significant values are displayed).

5. RESULTS

In this research we compare the similarity between hypnosis in Left-Right and Frontal-Back hemisphere separately like previous steps and gathered the obtained results.

Furthermore, we evaluated the ability of FSI to discriminate 3 groups of hypnotizability by means of receiver operating characteristic (ROC) curves. ROC curve is a graphical representation of the trade-offs between sensitivity and specificity. Accuracy quantifies the total number of subjects precisely classified. The area under the ROC curve is a single number summarizing the performance. ROC indicates the probability to predict the hypnosis scale of a randomly selected hypnotizable subject. Although the set of entropy, Higuchi and frequency band (low and high) could discriminate C3 & C4 channels in Left-Right hemisphere, ROC curve value has the acceptable value for discrimination (0.753), and similar to this result in Frontal-Back hemispheres only F8 & T6 (0.721) with energy and entropy features has the acceptable ROC curve value, so there should be a trade off between features set, ANOVA and ROC curve results.

Figure 2 represents the ROC curves obtained at Left-Right and Frontal-Back hemispheres with highest discrimination. The highest ROC (0.753 for Left-Right and 0.721 for Frontal-Back hemispheres) values were achieved in C3 & C4 and F8 & T6 channels respectively. **Table 1** and **Table 2** shows the features, discriminated channels, p and ROC value for Left-Right and Frontal-Back hemisphere respectively.

6. DISCUSSION

The differences between three groups were statistically significant in 19 channels ($p < 0.05$; ANOVA). Our results agree with previous studies that have analyzed electromagnetic brain recordings with different features. Significant differences were found between the Frontal-Back and Left-Right hemispheres in medium hypno

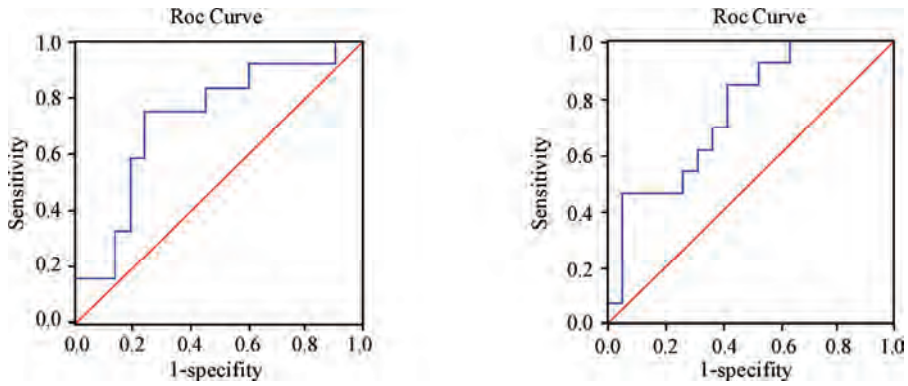

Figure 2. Roc curves showing the discrimination between Left-Right and Frontal-Back hemispheres and hypnotizability scale: (a) Left-Right hemisphere (Medium hypnotizability), (b) Frontal-Back hemispheres (medium hypnotizability).

Table 1. The features, discriminated channels, p and ROC values for Left-Right Hemispheres.

Features	Discriminate channels	sig.<0.05	ROC
Energy, Entropy	non	non	non
Entropy, Higuchi	non	non	non
Energy, Entropy, Frequency Band(low)	C3&C4	0.011	0.753
Energy, Entropy, Frequency Band(high)	C3&C4	0.043	0.518
Energy, Entropy, Frequency Band(low & high)	non	non	non

Table 2. The features, discriminated channels, p and ROC values for Frontal-Back Hemispheres.

Features	Discriminate channels	sig.<0.05	ROC
Energy, Entropy	F8&T6	0.042	0.721
Entropy, Higuchi	PZ&FZ	0.036	0.389
Energy, Entropy, Frequency Band(low)	non	non	non
Energy, Entropy, Frequency Band(high)	P4&F4-T5&F7	0.016-0.006	0.198-0.389
Energy, Entropy, Frequency Band(low & high)	PZ&FZ	0.031	0.555

tizable subjects. The discriminated channels were analyzed by means of a ROC curve. The highest ROC (0.753 for Left-Right and 0.721 for Frontal-Back hemispheres) values were achieved in C3 & C4 and F8 & T6 channels respectively.

REFERENCES

[1] Fingelkurts, A. A., Kallio, S., and Revonsuo, A. (2007) Hypnosis induces a changed composition of brain oscillations in EEG. Contemp. Hypnosis, **24(1)**, 3–18.

[2] Xu, W., Guan, C., Siong, C. E., Ranganatha, S., Thulasidas, M. and Wu, J., (2004) High accuracy classification of EEG signal, Intl. Conference on Pattern Recognition, 391–394.

[3] Andrzejak, R. G., Lehnertz, K., Mormann, F., Rieke, C., David, P., and Elger, C. E., (2001) Indications of nonlinear deterministic and finite-dimensional structures in time series of brain electrical activity: Dependence on recording region and brain state. Phys Rev E, **64**, 061907.

[4] Binaghi, E., Ventura, A. D., Rampini, A., and Schettini, R. (1993) Fuzzy reasoning approach to similarity evaluation in image analysis. International Journal of Intelligent Systems, **8**, 749−769.

[5] Tolias, Y. A., Panas, S. M., and Tsoukalas, L. H., (2001) Generalized fuzzy indices for similarity matching, Fuzzy Sets and Systems, **120(2)**, 255−270.

[6] Ali Moti Nasrabadi.

[7] Domenick, D. G. (1998) International 10-20 electrode placement system for sleep. http://members.aol.com/aduial/1020sys.html.

[8] Sabeti, a M., Boostani, a R., Katebi, a S. D., and Price, G. W. (2007) Selection of relevant features for EEG signals classification of schizophrenic patients. 10.1016/j.bspc.03.003.

[9] Übeyli, E. D. Fuzzy similarity index for discrimination of EEG signals. EMBS Annual.

[10] Gómez, C., *et al*. (2008) Use of the Higuchi's fractal dimension for the analysis of MEG recordings from Alzheimer's disease patients. Med Eng Phys, doi:10.1016/j.medengphy.06.010.

[11] Stam, C. J. (2005) Nonlinear dynamical analysis of EEG and MEG: Review of an emerging field. Clin Neurophysiol, **116**, 2266–301.

[12] Accardo, A., Affinito, M., Carrozzi, M., and Bouquet, F. (1997) Use of fractal dimension for the analysis of electroencephalographic time series. Biol Cybern, **77**, 339–50.

[13] Kwang, H. L., Song, Y.-S., and Lee, K.-M. (1994) Similarity measure between fuzzy sets and between elements, Fuzzy Sets and Systems, **62(3)**, 291–293.

J. Biomedical Science and Engineering, 2009, 2, 363-365 **JBiSE**
doi: 10.4236/jbise.2009.25052 Published Online September 2009 (http://www.SciRP.org/journal/jbise/).

Layered-resolved autofluorescence imaging of photoreceptors using two-photon excitation

Ling-Ling Zhao, Jun-Le Qu*, Dan-Ni Chen, Han-Ben Niu

Key Laboratory of Optoelectronic Devices and Systems of Ministry of Education, Institute of Optoelectronics, Shenzhen University, Shenzhen, China.
Email: jlqu@szu.edu.cn

Received 21 April 2009; revised 15 May 2009; accepted 19 May 2009.

ABSTRACT

In this paper, we present our investigation on the morphological and autofluorescence characteristics of the cones and rods using two-photon excitation with a femtosecond Ti: sapphire laser. The results show that the microstructures of the photoreceptor layers can be visualized at submicron level without any staining or slicing. The morphology and spatial distribution of the cones and rods can be resolved by autofluorescence imaging. The autofluorescence in the photoreceptor outer segments is much stronger than other layers, but susceptible to light-induced damage.

Keywords: Two-Photon Excitation; Photoreceptor; Retina; Autofluorescence

1. INTRODUCTION

There are two basic types of photoreceptors, rods and cones, which are of different shapes and involved in different visual functions. Rods are highly sensitive to the weak and faint light, which are used for vision under dark-dim conditions at night. Cones are the basis of our color perceptions since they have different wavelength sensitivity and the consequent pathways of connectivity to the brain. The dysfunction of photoreceptors is one of most important factors of ocular fundus diseases, such as retinitis pigmentosa (RP), age-related macular degeneration (AMD), glaucoma, and so forth. [1,2] Retinitis pigmentosa is the leading cause of inherited blindness, which is characterized by progressive loss of visual function related to death of rods then cones, and leads to the breakdown of the photoreceptor outer segment disc membranes. Patients with retinitis pigmentosa (RP) show various symptoms. The onset is often gradual and insidious, and many patients fail to recognize the manifestations of this condition until it has progressed significantly. When patients do report symptoms, they commonly include difficulty with night vision (nyctalopia) as well as loss of peripheral vision. In addition, age-related macular degeneration (AMD) is a slowly progressive disease that is related to the abnormal accumulation of lipofuscin, which is located in the retinal pigment epithelium (RPE) cells and is a byproduct of incomplete digestion of photoreceptor outer segment disc membranes. Generally, the people who suffer from AMD have an early abnormal condition and experience minor visual loss. For many of these people, macular degeneration will not progress to a more serious condition. But for the others, macular degeneration may lead to severe loss of visual acuity (or centralvision). [3]

Fortunately, with the advent of near infrared femtosecond laser, multiphoton excitation fluorescence microscopy, which is based on simultaneous absorption of two or more photons, has become a novel and powerful tool in biomedical imaging. [4] It enables the possibilities to investigate the autofluoresecence and spatial distribution of photoreceptors at early stage of ocular diseases, since it can increase the penetrability through the thick biological tissue and provide high-resolution imaging of endogenous fluorophores in biological tissue. [5,6] And also, Multiphoton microscopy can facilitate the simultaneous excitation of different endogenous fluorophores in biological specimens at submicron level, which benefits to the identification and evaluation of the morphological and autofluorescence characteristics of the photoreceptors. Several endogenous fluorophores exist in the photoreceptors, e.g., all-trans-retinol, NAD (P) H, A2-PE, FAD etc, which are all related to the metabolism and visual cycle. [7,8,9,10] Therefore, multiphoton microscopy can be used to investigate the autofluorescence characteristics of photoreceptors.

In this study, layered-resolved autofluorescence imaging using two-photon excitation has been performed, which can provide not only structural, but also functional information about the different layers of photoreceptors, particularly photoreceptor inner and outer segments which are vital functional layers in the photoreceptors and significant for the early diagnosis of the retinal diseases.

2. MATERIALS AND METHODS

2.1. Materials

Fresh porcine eyes are supplied by the local slaughterhouse and extracted immediately after slaughtering within one hour. The eyeballs are transported to the lab in PBS (PH 7.16)/normal saline solution and kept in a freezing box (0-4℃). The eyes are kept in the PBS (PH 7.16)/normal saline solution for less than 30 minutes before experiment. A 6mm-diameter retina-RPE-choroid-sclera complex near the macula (both the rods and cones are in existence) is trephined and the neurosensory retina is peeled off gingerly. The side that connects with the RPE cells is kept down to contact the slip of a specially designed chamber. All the specimens are freshly prepared without fixing, slicing and labeling.

2.2. Methods

The experiment is performed on an inverted confocal laser scanning microscope (Leica TCS SP2). A mode-locked femtosecond Ti: sapphire laser (Coherent Mira 900F) is coupled to the microscope for two-photon excitation of the specimen. The Ti: Sapphire laser produces ultrashort laser pulses with tunable wavelength from 700nm to 980nm, a pulse width of about 120 fs and a repetition rate of 76 MHz. The excitation wavelength in this experiment is 800nm. A 63×/NA1.32 oil-immersion objective is used to focus the excitation light onto the specimen and collect the autofluorescence from the photoreceptors.

3. RESULTS AND DISCUSSIONS

Both the rod and cone photoreceptors are consisted of four parts, i.e., the outer segment, the inner segment, the nuclear region and the synaptic terminal. The outer segment is filled with stacks of membranes containing the visual pigment molecules such as rhodopsins. The inner segment contains mitochondria, ribosomes and membranes where opsin molecules are assembled and passed to the outer segment discs. The nuclear region contains the nucleus of the photoreceptor cell and the synaptic terminal is responsible for the neurotransmission to second order neurons.

Usually rod photoreceptors are slim rod-shaped structures with their inner and outer segments filling the area between the larger cones in the subretinal space and stretching to the pigment epithelium cells. Rod cell bodies make up the remainder of the outer nuclear layer below the cone cell bodies. Cone photoreceptors, on the other hand, are robust conical-shaped structures that have their cell bodies situated in a single row right below the outer limiting membrane and their inner and outer segments protruding into the subretinal space towards the pigment epithelium. Apical processes from the pigment epithelium envelope the outer segments of both rods and cones.

In our study, we obtain the image of rod and cone photoreceptors nicely aligned along vertical and horizontal directions using two-photon excitation fluorescence microscopy and we also identify the fluorophores in photoreceptor outer segments by analyzing the spectrum, intensity, distribution and components of autofluorescence [11]. **Figure 1** shows the cross-sectional autofluorescence image of photoreceptors, in which individual cones and rods are clearly resolved. The XZ image of the different photoreceptor layer structures are distinguished accurately with submicron resolution. The autofluorescence in the photoreceptor outer segments is much stronger than other layers, since the outer segment is abundant in many fluorophores, such as all-trans-retinol, A2-PE, FAD, etc.

The XY image of the photoreceptor outer segment is shown in **Figure 2**. Because the photoreceptor outer segment is connected with the RPE cells, when the photoreceptor outer segments is separated from the

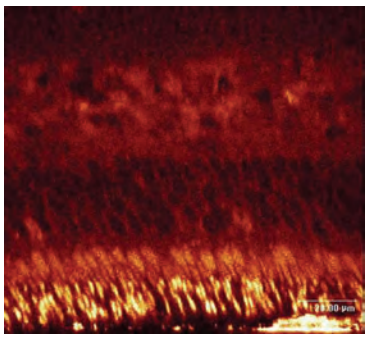

Figure 1. Cross-sectional autofluorescence image of photoreceptors excited by two-photon excitation. ($\lambda_{Ti:\ Sapphire}$=800nm).

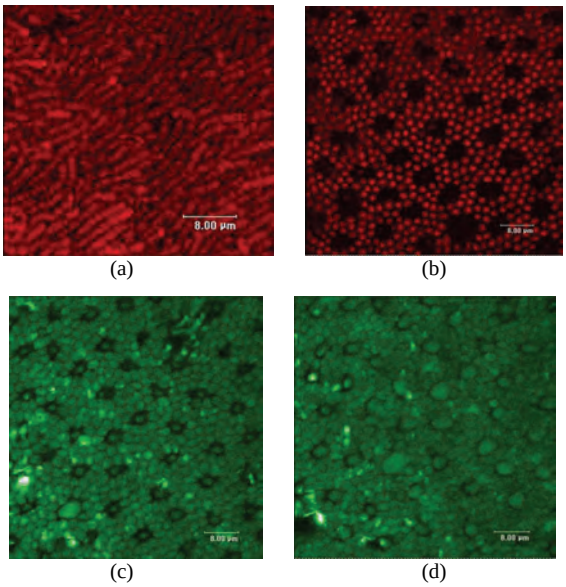

Figure 2. Autofluorescence image of photoreceptor out segment excited by two-photon excitation. ($\lambda_{Ti:\ Sapphire}$ =800nm).

RPE cells, the outer segment at top may be disarranged, but the pillar-like shape can be observed (**Figure 2(a)**). When focusing the imaging plane slightly into the specimen, we can see the rod is aligned annularly, round in shape and 2 μm in diameter (**Figure 2(b)**) and the center is dark. With focusing the objective further into the specimen, the autofluorescence of cone outer segment, which locates in the center, can be detected, and the size of the cones is becoming larger and larger (**Figure 2(c)** and **Figure 2(d)**), whereas the autofluorescence of rod outer segment weakens.

Figure 3 shows the autofluorescence image of photoreceptor inner segment. The bigger cell is corresponding to the cone inner segment whose diameter is around 6 μm. Rod inner segment is around the cone and the diameter is about 2μm. **Figure 4** is the autofluorescence image of photoreceptor nuclear region, which contains the nucleus of the photoreceptor cell.

4. CONCLUSIONS

Our results demonstrate, for the first time, that morphological and autofluorescence characteristics of different layers of photoreceptors can be identified by autofluorescence imaging using two-photon excitation. Since the cross section of two photon excitation is much smaller than that of single photon excitation, and two photon excitation is quadratically dependent on the intensity, it is susceptible to photondamage at the focal point. In our work, the structure and properties of procine eyes are very similar to human eyes, so the laser power on the sample is limited to the order of mW (3-4mW), which accords with ANSI about laser safety criteria for human eye. Moreover, this in vitro autofluorescence imaging of photoreceptors can give much detailed structural and functional information at high spatial resolution, which can help to more clearly understand the in vivo ocular fundus autofluorescence images obtained by confocal scanning laser ophthalmoscopy. And also, two photon excitation is IR illumination, which can penetrate the anterior segment of eyes, such as cornea and lens, and get the whole autofluorescence characteristics of the living retina, and eliminate the autofluorescence interference of the anterior segment of eyes by tightly focus without confocal pinhole. Thus, in vitro autofluorescence imaging of photoreceptors using two photon excitation can provide a clue and develop a two-photon laser scanning ophthalmoscope for in vivo living retina imaging. Although much research remains to be done, it appears that this technique has great potential to bridge the gap between clinical examination and invasive biopsy and thus facilitate the early detection and diagnosis of ocular diseases. The distribution and intensity of autofluorescence may provide an insight into the sequence of events that leads to retinal damage and may help elucidate pathological mechanisms.

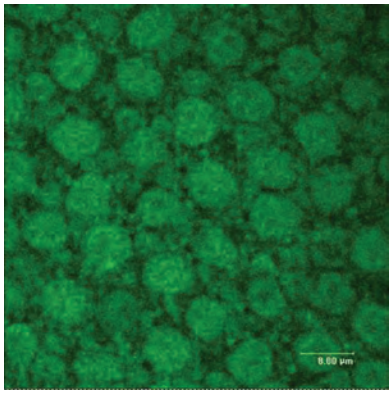

Figure 3. Autofluorescence image of photoreceptor inner segment.

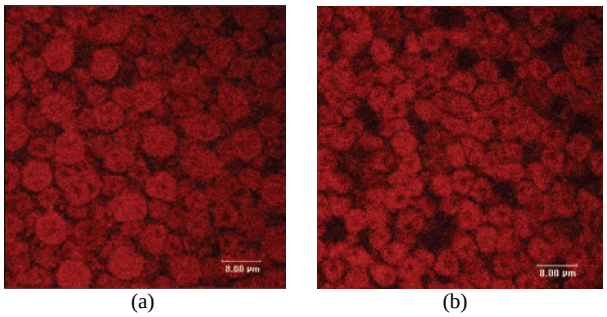

(a) (b)

Figure 4. Autofluorescence image of cone nuclear region (a) and rod nuclear region (b), excited by wo-photon excitation ($\lambda_{\text{Ti: Sapphire}}$=800nm).

5. ACKNOWLEDGMENTS

This work is supported by the National Natural Science Foundation of China (NSFC) under contract No. 60627003 and No. 60408011, and is also supported in part by Guangdong Natural Science Foundation grant No. 5010500.

REFERENCES

[1] Jiangang, G. and Kyeongmi, C., (2002) PNAS, **99(8)**, 5698.
[2] Kayatz, P., Thumann, G., Luther, T. T., *et al*., (2001) Invest. Ophthalmol. Vis. Sci., **42**, 241.
[3] Hopkins, J., Walsh, A. and Chakravarthy, U., (2006) Invest. Ophthalmol. Vis. Sci., **47**, 2269.
[4] Brakenhoff, G. J., Squier, J., Norris, T. and Blito, A. C., (1996) J. Microsc., **181**, 253.
[5] Denk, W., Strickler, J. H., (1990) Science, **248**, 73.
[6] Han, M. and Giese, G., (2007) Journal of Biomedical Optics, **12(2)**, 024012.
[7] Chunhe, C., (2005) Biophysical Journal, **88**, 2278.
[8] Kim, S. R. and Nakanishi, K., (2006) Experimental Eye Research, **82**, 828.
[9] Laura, L. E. and John, S. D., (2004) Photochemistry and Photobiology, **79(2)**, 127.
[10] Schweitzer, D., Schenke, S., and Hammer, M., (2007) Microscopy Research and Technique, **70**, 410.
[11] Zhao, L., Qu J., and Niu, H., (2007) Proc. SPIE, **6826**, 682614.

Call for Papers

The 4th International Conference on Bioinformatics and Biomedical Engineering (iCBBE 2010)

June 18-20, 2010 Chengdu, China

The 4th International Conference on Bioinformatics and Biomedical Engineering (iCBBE 2010) will be held from June 18th to 20th, 2010 in Chengdu, China. You are welcome to share your recent advances and achievements in all aspects of bioinformatics and biomedical engineering on the conference. **And all accepted papers in iCBBE 2010 will be published by IEEE and indexed by Ei Compendex and ISTP.**

Topics

Bioinformatics and Computational Biology

- Protein structure, function and sequence analysis
- Protein interactions, docking and function
- Computational proteomics
- DNA and RNA structure, function and sequence analysis
- Gene regulation, expression, identification and network
- Structural, functional and comparative genomics
- Computer aided drug design
- Data acquisition, analysis and visualization
- Algorithms, software, and tools in Bioinformatics
- Any novel approaches to bioinformatics problems

Biomedical Engineering

- Biomedical imaging, image processing & visualization
- Bioelectrical and neural engineering
- Biomechanics and bio-transport
- Methods and biology effects of NMR/CT/ECG technology
- Biomedical devices, sensors and artificial organs
- Biochemical, cellular, molecular and tissue engineering
- Biomedical robotics and mechanics
- Rehabilitation engineering and clinical engineering
- Health monitoring systems and wearable system
- Bio-signal processing and analysis
- Biometric and bio-measurement
- Biomaterial and biomedical optics
- Other topics related to biomedical engineering

Special Sessions

Biomedical imaging
Biostatistics and biometry
The information technology in bioinformatics
Environmental pollution & public health

Sponsors

IEEE Eng. in Medicine and Biology Society, USA
Gordon Life Science Institute, USA
University of Lowa, USA
Wuhan University, China
Sichuan University, China
Journal of Biomedical Science and Engineering, USA

Important Dates

Paper Due: Oct.30, 2009
Acceptance Notification: Dec.31, 2009
Conference: June 18-20, 2010

Contact Information

Website:http://www.icbbe.org/2010/
E-mail: submit@icbbe.org

Call for Papers

Journal of Biomedical Science and Engineering (JBiSE)

www. scirp. org/journal/jbise

JBiSE, an international journal, publishes research and review articles in all important aspects of biology, medicine, engineering, and their intersection. Both experimental and theoretical papers are acceptable provided they report important findings, novel insights, or useful techniques in these areas. All manuscripts must be prepared in English, and are subject to a rigorous and fair peer-review process. Accepted papers will immediately appear online followed by printed in hard copy.

Subject Coverage

Bioelectrical and neural engineering

Bioinformatics

Medical applications of computer modeling

Biomedical modeling

Biomedical image processing & visualization

Real-time health monitoring systems

Biomechanics and bio-transport

Patten recognition and medical diagnosis

Biomedical effects of electromagnetic radiation

Safety of wireless communication devices

Biomedical devices, sensors, and nano technologies

NMR/CT/ECG technologies and EM field simulation

Physiological signal processing

Medical data mining

Other related topics

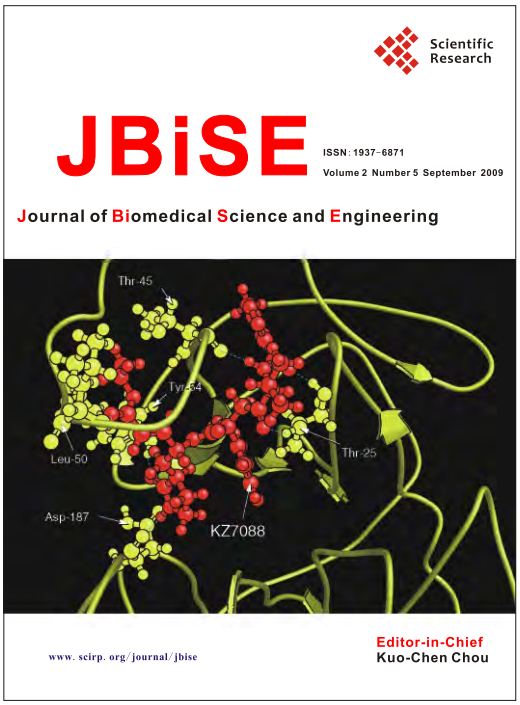

Editor–in–Chief

Editorial Board

Notes for Intending Authors

Submitted papers should not have been previously published nor be currently under consideration for publication elsewhere. Paper submission will be handled electronically through the website. All papers are refereed through a peer review process. For more details about the submissions, please access the website.

Website and E-Mail

www. scirp. org/journal/jbise

Email: jbise@scirp.org

ISSN 1937-6871 (Print), 1937-688X (Online)

Journal of Biomedical Science and Engineering, 2009, 2.
Published Online September 2009 in SciRes (http://www.scirp.org/journal/jbise).

TABLE OF CONTENTS

Volume 2, Number 5, September 2009

977193768700108